

# Femtosecond laser writing of embedded waveguides in polymers

Von der Fakultät für Mathematik und Physik  
der Gottfried Wilhelm Leibniz Universität Hannover  
zur Erlangung des Grades

**Doktor der Naturwissenschaften**

- Dr. rer. nat. -

genehmigte Dissertation

von

**Welm Maximilian Pätzold, Master of Science**

geboren am 29.11.1985 in Braunschweig

2017

Referent: Professor Dr. Uwe Morgner

Korreferent: Professor Dr. Carsten Reinhardt

Korreferent: Priv.-Doz. Dr. Ulrike Willer

Tag der Promotion: 02.06.2017

*Für Konrad Pätzold*

1928 – 2017





*“Once you eliminate the impossible, whatever remains,  
no matter how improbable, must be the truth.”*

— Sherlock Holmes



# Kurzfassung

Welm M. Pätzold

## Femtosekundenlaser-Schreiben von eingebetteten Wellenleitern in Polymeren

Femtosekundenlaser-Schreiben ist eine leistungsfähige Methode um nahezu beliebig geformte dreidimensionale Wellenleiter herzustellen, indem ein transparentes Material relativ zum Laserstrahl abgerastert wird. Nichtlineare Photoionisation ist der zugrundeliegende physikalische Prozess und wird durch die hohen Spitzenintensitäten von ultrakurzen Laserpulsen ausgelöst. Werden diese Pulse in ein Material fokussiert können lokale Modifikationen des Brechungsindex erzeugt werden. Vollständige 3D-Tauglichkeit und Schreibgenauigkeiten auf der Nanometerskala machen diese Technik zu einer idealen Methode für die Herstellung kompakter Wellenleiternetzwerke in *Lab-on-a-Chip* Anwendungen. Sie wird in verschiedenen Materialien eingesetzt, wie zum Beispiel Glas, Kristalle oder Polymere.

In dieser Dissertation wird das Femtosekundenlaser-Schreiben von Wellenleitern in Polymeren untersucht. Polymere sind ein häufig verwendetes Material für optische Anwendungen und stellen eine günstige und leichte Alternative zu Glas dar. Um das Schreiben von Wellenleitern zu ermöglichen, werden zunächst die Brechungsindexmodifikationen in Abhängigkeit der Laserparameter untersucht. Dabei zeigt sich, dass diese Modifikation durch Materialspannungen und -verdichtungen in der Nähe des Fokusvolumens entstehen. Ein Refokussierungseffekt, der während des Schreibens auftreten kann, stellt sich als sehr vorteilhaft heraus, um einen nahezu symmetrischen Wellenleiter mit nur einer Modifikationsspur zu erzeugen. Die Propagationsverluste eines solchen Wellenleiters liegen in einer Größenordnung von  $0.5 \text{ dB/cm}$ .

Darüber hinaus werden komplexere Wellenleitergeometrien, welche aus mehreren Modifikationsspuren zusammengesetzt sind, untersucht. Ein Ansatz, bei dem eine Reihe von Spuren mit lateralem Versatz geschrieben werden, erzeugt qualitativ hochwertige Wellenleiter. Die Propagationsverluste sinken in diesem Fall auf bis zu  $0.3 \text{ dB/cm}$ . Weiter führt die Einwirkung mehrerer Modifikationsspuren auf das Material zu einem Brechungsindexkontrast von bis zu  $\Delta n = 2 \cdot 10^{-3}$ . Ein Indexkontrast dieser Größenordnung ermöglicht das Leiten von Licht durch Kurven mit vernachlässigbaren Krümmungsverlusten für Kurvenradien mit  $R \geq 20 \text{ mm}$ .

**Schlagwörter:** Laserdirektschreiben, Polymerwellenleiter, nichtlineare Phänomene



# Abstract

Welm M. Pätzold

## Femtosecond laser writing of embedded waveguides in polymers

Femtosecond laser writing is a powerful technique to create virtually arbitrary three-dimensional waveguides in a transparent medium. The underlying physical mechanism is nonlinear photoionization triggered by the high peak intensities of ultrashort laser pulses. Tightly focusing these pulses inside the volume of a medium can induce local modifications of the refractive index. Scanning a sample relative to the beam generates waveguides. Full 3D capabilities and writing accuracies on the nanometer scale make this technique an ideal tool for the fabrication of compact waveguide networks for lab-on-a-chip applications. It is applied on various materials such as glasses, crystals and polymers.

In this thesis, femtosecond laser waveguide writing in polymers is investigated. Polymers are a cheap and lightweight alternative to glasses in many optical applications. To enable waveguide writing, first of all, refractive index modifications in dependence of the irradiation parameters are studied. It is found that the index modification is a result of stress and material densification in the vicinity of the focal volume. In this context, a refocusing effect, which can occur during the writing process, proves very advantageous to achieve nearly symmetric fundamental-mode waveguiding with a single modification track. The propagation losses of such a waveguide are determined to be in the order of  $0.5 \text{ dB/cm}$ .

More complex waveguide geometries are composed of multiple modification tracks. A writing approach with a series of horizontal modification tracks leaving a gap in the middle as the waveguide core is found to result in high quality waveguides. The propagation losses in this case decrease to  $0.3 \text{ dB/cm}$ , the lowest losses observed so far in this class of material. In addition, the influence of multiple modification tracks on the material results in a refractive index contrast up to  $\Delta n = 2 \cdot 10^{-3}$ . With an index contrast of this magnitude, light guiding through curved waveguides is demonstrated with negligible bend losses for radii of curvature  $R \geq 20 \text{ mm}$ .

**Key words:** laser direct writing, polymer waveguides, nonlinear phenomena



# Contents

<b>Introduction</b>	<b>1</b>
<b>1 Background</b>	<b>5</b>
1.1 Optical waveguiding . . . . .	5
1.1.1 Fundamentals . . . . .	6
1.1.2 Linearly polarized modes . . . . .	8
1.1.3 Bent waveguides . . . . .	10
1.1.4 Evanescent coupling . . . . .	12
1.2 Femtosecond laser-material interaction . . . . .	14
1.2.1 Nonlinear photoionization . . . . .	14
1.2.2 Energy distribution processes . . . . .	16
1.2.3 Origins of refractive index change . . . . .	17
1.3 Femtosecond laser waveguide writing . . . . .	21
1.3.1 Irradiation parameters . . . . .	21
1.3.2 Writing configuration . . . . .	26
1.3.3 Beam shaping . . . . .	27
1.3.4 Track morphology . . . . .	28
1.3.5 Waveguide geometries . . . . .	30
1.3.6 Functional waveguides in polymers . . . . .	33
1.4 Photonic devices . . . . .	35
<b>2 Experimental methods</b>	<b>37</b>
2.1 Writing setup . . . . .	37
2.1.1 Femtosecond laser source . . . . .	38
2.1.2 3D translation stages . . . . .	39
2.1.3 Alignment procedure . . . . .	39
2.2 Waveguide fabrication . . . . .	40
2.2.1 Sample preparation . . . . .	40
2.2.2 Writing Process . . . . .	41
2.2.3 Sample post-processing . . . . .	42

---

2.3	Waveguide characterization . . . . .	43
2.3.1	Optical evaluation . . . . .	43
2.3.2	Characterization Setup . . . . .	43
2.3.3	Numerical aperture measurement . . . . .	46
2.3.4	Waveguide losses . . . . .	46
<b>3</b>	<b>Results</b>	<b>51</b>
3.1	Structure of a modification track . . . . .	51
3.1.1	Single-pulse modification . . . . .	52
3.1.2	Heat accumulation . . . . .	54
3.1.3	Evolution of the track morphology . . . . .	58
3.2	Single-track waveguides . . . . .	62
3.2.1	Refractive index change mechanism . . . . .	62
3.2.2	Refocusing effect . . . . .	64
3.2.3	Cascaded-focus waveguide writing . . . . .	67
3.2.4	Phase gratings . . . . .	72
3.3	Multi-track waveguides . . . . .	73
3.3.1	Dual-track waveguides . . . . .	73
3.3.2	Cascaded-focus multi-track waveguides . . . . .	76
3.3.3	Photonic-crystal geometry . . . . .	83
3.4	Applications . . . . .	84
3.5	Critical remarks . . . . .	87
<b>4</b>	<b>Conclusion and Outlook</b>	<b>91</b>
	<b>Bibliography</b>	<b>95</b>
	<b>List of Figures</b>	<b>107</b>
	<b>A Heat Accumulation Simulation</b>	<b>115</b>
	<b>Publications</b>	<b>117</b>
	<b>Curriculum Vitae</b>	<b>119</b>



# Introduction

While in the 20<sup>th</sup> century electronics was a dominant technology, photonics are expected to take their place in the 21<sup>st</sup> century [Thy14]. Photonics is the science of generating, controlling and detecting photons. In this context, the guiding of light is a key mechanism for transmitting optical signals. In the field of telecommunications, fiber-optic networks have already replaced traditional copper cables for long-haul data transfer. Higher data rates thanks to an increased bandwidth and longer propagation due to lower attenuation are huge advantages of optical data transmission over electronic data transmission. On smaller scales, photonics for intra- and inter-system data transfer will take over in the long run as well [Dan15]. For example, waveguides are nowadays commonly used in lab-on-a-chip applications [Was10]. A lab-on-a-chip is a device that aims to miniaturize analysis systems to the centimeter or millimeter scale. The waveguides in these chips are usually based on surface structuring of glass, silicone or polymer wafers. However, further integration demands for complex and compact waveguide networks which call for innovative waveguide fabrication technologies.

Since its development in 1960, the laser has become one of the most powerful and flexible tools in fundamental research and applications alike. One of its prominent features is the possibility to concentrate energy in space and time. Ultrafast lasers emit pulses with durations in the femtosecond range which can trigger nonlinear effects due to their high peak intensities [Tho13b]. When tightly focused into a transparent material, nonlinear absorption of such laser pulses results in an energy deposition limited to the focal volume [Gat08]. This effect enables three-dimensional micromachining of materials such as glasses, crystals and polymers and since it does not depend on specific masks, this technique is highly flexible and ideal for rapid prototyping.

In 1996 it was demonstrated that permanent modifications to the refractive index can be induced below the surface of glass by applying a femtosecond laser micromachining technique [Dav96]. By simply translating the substrate relative to the laser focus, embedded waveguide structures can be fabricated. A femtosecond laser in this case may be thought of as an “optical pen” that three-dimensionally inscribes

refractive index modifications into the volume of a medium. Therefore, the process is typically called *waveguide writing*. Due to this property, femtosecond laser writing makes the fabrication of virtually any arbitrary waveguide structure feasible [Ose12]. It enables devices such as  $3 \times 3$  directional couplers [Suz06], 3D power splitters [Pos10] and three-dimensional waveguide arrays for all-optical routing and switching in photonic circuits [Kei11]. Femtosecond laser written waveguides have also been successfully combined with microfluidic channels of a commercial fused silica lab-on-a-chip [MV09].

Polymers, chemical compounds consisting of chains of repeating macromolecules, are good candidates as host material for future photonic devices. They have a number of advantages compared to glasses which makes the material of great interest for optical applications, including waveguiding. Among other things, polymers are cheap, lightweight, easy to process and it is easy to tailor their optical properties [Han15]. Incorporating flexibilizers into the material can make a polymer flexible which allows for the fabrication of large scale sensoric foils which may be applied on plane or curved surfaces alike. In combination with the femtosecond laser waveguide writing technique, three-dimensional polymer waveguide networks may be the foundation for next generation optoelectronic applications.

## **Goals and structure of the thesis**

While femtosecond laser waveguide writing is already widely applied in glasses and crystals [Che14], relatively little work has been done in polymers so far. A low damage threshold and high propagation losses are two of the main obstacles in achieving the formation of efficient waveguides [Eat12]. Therefore, the goal of this work is to develop novel femtosecond laser writing schemes for the fabrication of low-loss waveguides in polymers. In addition, a large refractive index increase is desirable since it enables the guiding of light through curves at low bend losses. The main polymer used for this purpose is Poly(methyl methacrylate) (PMMA) which exhibits high transmission in the visible and near-infrared range and is therefore a popular material for polymer optical fiber cores [Kai16].

First, the influence of various irradiation parameters on refractive index modifications in PMMA is thoroughly studied. Next, new writing approaches are developed and the resulting waveguides are characterized regarding the quality of the guided mode, occurring losses and magnitude of the refractive index modification.

The thesis is structured as follows: Chapter 1 gives theoretical background information on optical waveguiding as well as an overview of the current state of femtosecond laser waveguide writing. Chapter 2 introduces the experimental setups and methods for the fabrication and the characterization of waveguides. Chapter 3 reports on the experimental studies which have been conducted on waveguide writing in PMMA. It focuses especially on the formation of a continuous modification track and the evaluation of various waveguide geometries. Chapter 4 summarizes the findings of this work and gives a brief outlook on possible future experiments.



# Chapter 1

## Background

This chapter presents theoretical aspects of optical waveguiding, fundamentals of femtosecond laser-material interaction in dielectrics – especially focusing on the origins of refractive index changes in polymers – and finally the process of femtosecond laser waveguide writing.

### 1.1 Optical waveguiding

Without spatial restrictions, the amplitude of a wave will typically gradually diffract over a large area or volume. A spherical wave for example decays according to the “inverse-square-law” as it radiates into three-dimensional space. In general, a waveguide is a structure that allows a wave to propagate without the dispersion of energy by physically constraining it in one or two dimensions.

Waveguiding may occur for all types of waves. The focus of this work lies on waveguides for electromagnetic waves with wavelengths in the visible and near infrared regime, typically called “optical waveguides”. A common type of optical waveguide is based on total internal reflection which may occur at the interface of two transparent media. When light transits from an optically denser medium with refractive index  $n_1$  into an optically thinner medium with  $n_2 < n_1$  it gets refracted according to Snells’ law

$$n_1 \sin \theta_1 = n_2 \sin \theta_2 . \quad (1.1)$$

In this case the angle of refraction  $\theta_2$  will be larger than the angle of incidence  $\theta_1$ . At a critical angle of incidence  $\theta_1 = \theta_c$ , the angle of refraction becomes  $\theta_2 = 90^\circ$ . Consequently, for all  $\theta_1 > \theta_c$  a real solution for  $\theta_2$  does not exist anymore to satisfy the above equation. As a result, the beam is totally reflected at the interface. By creating a core of a medium with refractive index  $n_1$  surrounded by a cladding of refractive index  $n_2$ , light may be trapped inside the core as long as it satisfies the condition for total internal reflection.

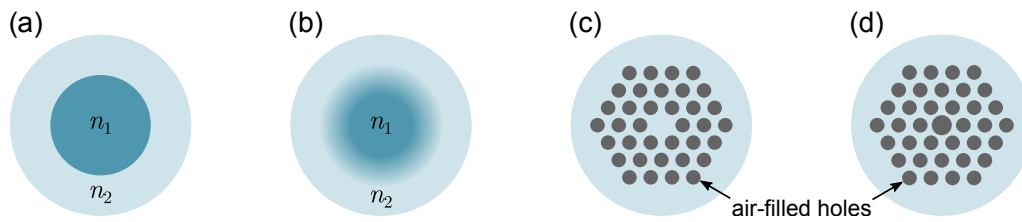


**Figure 1.1:** Cross-sectional schematics of: (a) step-index waveguide, (b) graded-index waveguide, (c) photonic-crystal waveguide with solid core surrounded by air-filled holes, and (d) photonic band gap waveguide with a hollow core.

One of the most common waveguide geometries consists of a core with circular cross section and a sharp transition to the cladding. This “step-index waveguide” is displayed in Figure 1.1(a). Another configuration is the “graded-index waveguide” where the refractive index gradually decreases with growing radial distance from the core, as shown in Figure 1.1(b). Graded-index waveguides have the advantage of decreased modal dispersion: a signal spreading over time because different modes experience different propagation velocities. Of course, different cross-sectional geometries are possible for these two types of waveguides.

An entirely different concept is displayed in Figure 1.1(c). A cladding of air-filled holes is distributed in a photonic-crystal structure around the core. If the core is solid, the guiding principle is based on an effective index-contrast as previously described. But it is also possible to create photonic band structures that forbid the electromagnetic wave to travel through certain areas. Such an area is called photonic band gap which makes it possible to confine light in a lower index core or even in air. A schematic of a photonic band gap waveguide is shown in Figure 1.1(d). In the following, some basic characteristics and properties of a step-index waveguide with circular cross section will be discussed.

### 1.1.1 Fundamentals

The most fundamental characteristics of a step-index waveguide may be described in terms of ray-optics. Figure 1.2 shows a schematic of the profile of such a waveguide. As mentioned before, for light to be guided inside the waveguide core, it has to satisfy the condition for total internal reflection. If a beam falls within the acceptance cone when it passes from an external medium into the waveguide core, the angle of incidence at the core-cladding interface will be larger than the critical angle.

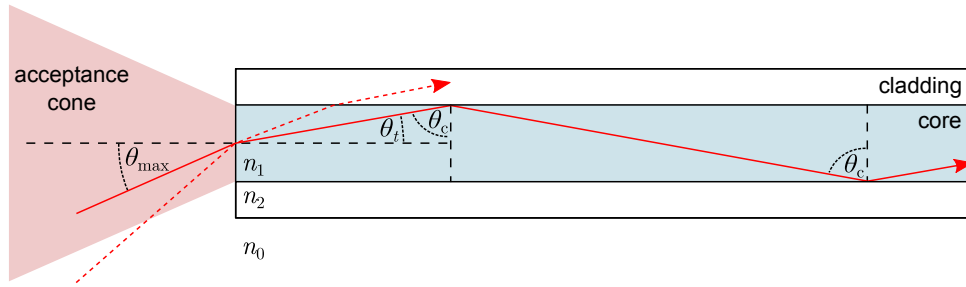


**Figure 1.2:** Optical waveguide with core index  $n_1$  exceeding the cladding index  $n_2$ . The maximum acceptance angle  $\theta_{\max}$  is determined by the critical angle  $\theta_c$  and the refractive index  $n_0$  of the external medium. The acceptance cone is given by  $2\theta_{\max}$ .

The angle of refraction  $\theta_t$ , for light transiting from an external medium with refractive index  $n_0$  into the core, is linked to the critical angle  $\theta_c$  by

$$\sin \theta_c \stackrel{(1.1)}{=} \frac{n_2}{n_1} = \cos \theta_t = \sqrt{1 - \sin^2 \theta_t} . \quad (1.2)$$

The maximum acceptance angle  $\theta_{\max}$  of a waveguide is then determined by applying Snells' law for the interface between an external medium of refractive index  $n_0$  and the waveguide core of  $n_1$ , and inserting it into Equation (1.2). The relation for the maximum acceptance angle becomes

$$\sin \theta_{\max} = \frac{1}{n_0} \sqrt{n_1^2 - n_2^2} . \quad (1.3)$$

The full acceptance cone is then given by  $2\theta_{\max}$ . The numerical aperture (NA) of a waveguide is then defined as

$$\text{NA} = n_0 \sin \theta_{\max} \stackrel{(1.3)}{=} \sqrt{n_1^2 - n_2^2} \approx \sqrt{2n_1 \Delta n} . \quad (1.4)$$

The core-cladding index difference  $\Delta n = n_1 - n_2$ , also called index contrast, is typically very small which allows for the approximation  $n_1 + n_2 \approx 2n_1$  in the above equation.

A standing wave forms at the boundary and penetrates the optically thinner medium with an exponential decay of the amplitude. This electric field, which extends to the cladding of a waveguide, is the evanescent field. From the evanescent field results the Goos-Hänchen effect: a small lateral shift of a reflected linearly polarized beam of finite size [Goo47]. That means the actual reflection plane lies inside the optically thinner medium.

### 1.1.2 Linearly polarized modes

The electric field distribution of light propagating in a waveguide is calculated by applying a wave optics approach. For the following considerations, a step-index waveguide with a cylindrical core of radius  $a$  and sufficiently large cladding is assumed. The refractive index of the core is  $n_1$  and that of the cladding is  $n_2$ . Detailed derivations can be found in [Sal07]. In the absence of free electrons the wave equation of the electric field in a medium of refractive index  $n$  is given by

$$\Delta \vec{E} = \frac{n^2}{c^2} \frac{\partial^2 \vec{E}}{\partial t^2} . \quad (1.5)$$

For symmetry reasons, cylindrical coordinates  $(r, \Phi, z)$  are used with  $z$  being the direction of propagation,  $r$  the radial distance and  $\Phi$  the azimuth. For the scalar electric field with angular frequency  $\omega$ , the following approach is applied:

$$E(r, \Phi, z, t) = \Psi_l(r) e^{-il\Phi} e^{-i\beta z} e^{i\omega t} . \quad (1.6)$$

The phase factor  $l$  must be an integer for continuity reasons after each turn in  $\Phi$ . The propagation constant  $\beta$  is the  $z$ -component of the wavenumber and is constrained by continuity at the core-cladding interface. With vacuum wavenumber  $k_0 = \omega/c$ , the differential equation for the radial component becomes

$$\frac{\partial^2 \Psi_l(r)}{\partial r^2} + \frac{1}{r} \frac{\partial \Psi_l(r)}{\partial r} = \left( \beta^2 + \frac{l^2}{r^2} - n^2 k_0^2 \right) \Psi_l(r) . \quad (1.7)$$

Using the wavenumbers  $k_1 = k_0 n_1$  and  $k_2 = k_0 n_2$ , two new variables are defined:

$$\begin{aligned} u &:= a \sqrt{k_1^2 - \beta^2} \quad , \\ w &:= a \sqrt{\beta^2 - k_2^2} \quad . \end{aligned} \quad (1.8)$$

In this context, the propagation constant has to satisfy  $k_1 > \beta > k_2$ . Substitution into Equation (1.7) gives the following set of differential equations for the core and cladding, respectively:

$$\frac{\partial^2 \Psi_l(r)}{\partial r^2} + \frac{1}{r} \frac{\partial \Psi_l(r)}{\partial r} = \left( \frac{l^2}{r^2} - \frac{u^2}{a^2} \right) \Psi_l(r), \quad r < a \quad (\text{core}), \quad (1.9)$$

$$\frac{\partial^2 \Psi_l(r)}{\partial r^2} + \frac{1}{r} \frac{\partial \Psi_l(r)}{\partial r} = \left( \frac{l^2}{r^2} + \frac{w^2}{a^2} \right) \Psi_l(r), \quad r > a \quad (\text{cladding}). \quad (1.10)$$



These are the Bessel differential equations which define the Bessel functions. The core equation is solved by  $J_l(x)$ , the Bessel function of the first kind, which oscillates like a sine or cosine function but with the amplitude decaying proportionally to  $1/\sqrt{x}$ . It is displayed for  $l = 0, 1, 2$  in Figure 1.3(a). The evanescent field in the cladding is described by  $K_l(x)$ , the modified Bessel function of the second kind, which decays exponentially with  $x$ . Taking into account that both branches have to be continuous and differentiable at  $r = a$  leads to the following solution:

$$\Psi_l(r) = \begin{cases} \frac{J_l(u \frac{r}{a})}{J_l(u)} & r < a \quad (\text{core}) \\ \frac{K_l(w \frac{r}{a})}{K_l(w)} & r > a \quad (\text{cladding}) \end{cases}, \quad (1.11)$$

with the side condition

$$\frac{u J_{l-1}(u)}{J_l(u)} = -\frac{w K_{l-1}(w)}{K_l(w)}. \quad (1.12)$$

For a given phase factor  $l$ , the propagation constant  $\beta$  can only assume a finite number of discrete values which can be determined by evaluating Equation (1.12). These solutions lead to the linearly polarized modes or  $LP_{lm}$  modes (numbered:  $m = 1, 2, 3, \dots$ ). An example of the radial distribution of the  $LP_{01}$  mode is shown in Figure 1.3(b). The effective refractive index is given by  $n_{\text{eff}} = \beta/k_0$  and is just as important for guided propagation as the refractive index is in free propagation. At this point it is clear that  $n_{\text{eff}}$  may vary significantly for different guided modes and should therefore not be confused with a weighted average of the core and cladding refractive index.

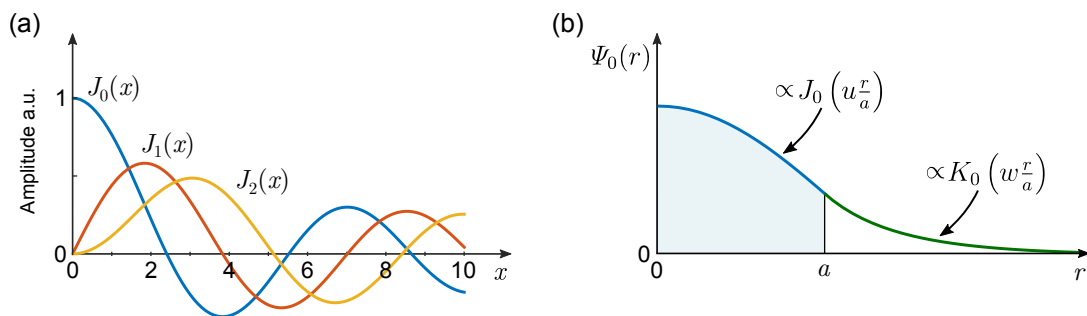


**Figure 1.3:** (a) Bessel functions of first kind  $J_l(x)$  for  $l = 0, 1, 2$ . (b) Radial distribution  $\Psi_0(r)$  of the  $LP_{01}$  mode in a waveguide with core radius  $a$ , calculated according to Equation (1.11).

Assuming an azimuthal dependence of  $\cos l\Phi$ , the electric field  $E(r, \Phi)$  yields the mode profiles displayed in Figure 1.4. In practice, calculating with Bessel functions can be troublesome. In these cases, a Gaussian distribution is a good approximation for the  $LP_{01}$  mode.

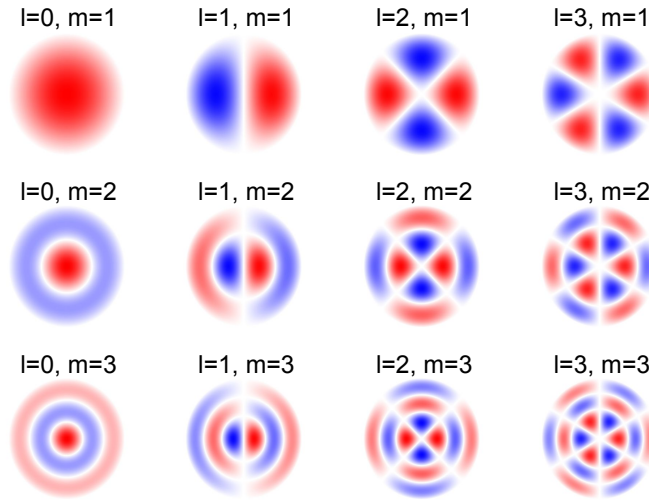


**Figure 1.4:** Linearly polarized modes for  $l = 0, 1, 2, 3$  and  $m = 1, 2, 3$ .

Another important parameter of step-index waveguides is the normalized frequency, also called  $V$  number:

$$V = \frac{2\pi a}{\lambda} \sqrt{n_1^2 - n_2^2} \stackrel{1.4}{=} \frac{2\pi a}{\lambda} \text{NA}. \quad (1.13)$$

With  $k_0 = 2\pi/\lambda$  and Equation (1.8), it can easily be seen, that it also holds

$$V^2 = u^2 + w^2. \quad (1.14)$$

When  $w \rightarrow 0$ , the propagation constant  $\beta$  of a waveguide mode approaches  $k_2$  and at the limit the wave is no longer confined. Therefore,  $w = 0 \Leftrightarrow u = V$  defines the cutoff condition and Equation (1.12) becomes  $uJ_{l-1}(u)/J_l(u) = 0$ . Since only the Bessel function  $J_0(u)$  is non-zero for  $u = 0$ , the cutoff frequency for the fundamental  $\text{LP}_{01}$  mode is  $u = 0$ . That means it can propagate even in small waveguide cores. All higher  $\text{LP}_{lm}$ -modes have a cutoff frequency at  $J_{l-1}(u) = 0$  (for  $l = 0$  the identity  $J_{-1}(u) = -J_1(u)$  is applied). Therefore, the total number of possible modes is the number of roots of  $J_{l-1}(u)$  that are smaller than  $V$ . The smallest nonzero value is the first root of  $J_0$  (see Figure 1.3(a)). Hence, a waveguide is single-mode for  $V < 2.4048$ .

### 1.1.3 Bent waveguides

All considerations of the previous sections were solely assuming light propagation in a straight waveguide. To construct compact footprint waveguide networks for real-

life applications, it is essential to direct light through bent structures at preferably arbitrary geometries. However, curves may cause additional losses in the waveguide depending on the radius of curvature [Hun09].

From a ray optics perspective, it is easy to see that the angle of incidence gets smaller if the beam hits a concave surface. If it falls below the critical angle for total internal reflection, part of the light is lost, as schematically depicted in Figure 1.5(a). For single-mode waveguides the wave picture is applied and it needs to be taken into account that the electric wave extends to the cladding. At the outside of the curve, the path length grows with increasing distance from the waveguide core. However, the propagation speed in the cladding is limited by the local speed of light. As a result, the phase front of the guided mode starts to trail behind and the wavefront is not planar anymore. The deformation of the phase front may be expressed as a radial component of the Poynting vector  $\vec{S}$  which results in the radiation of energy, shown in Figure 1.5(b). Typically, the bend losses grow rapidly as soon as a certain critical bend radius is reached.

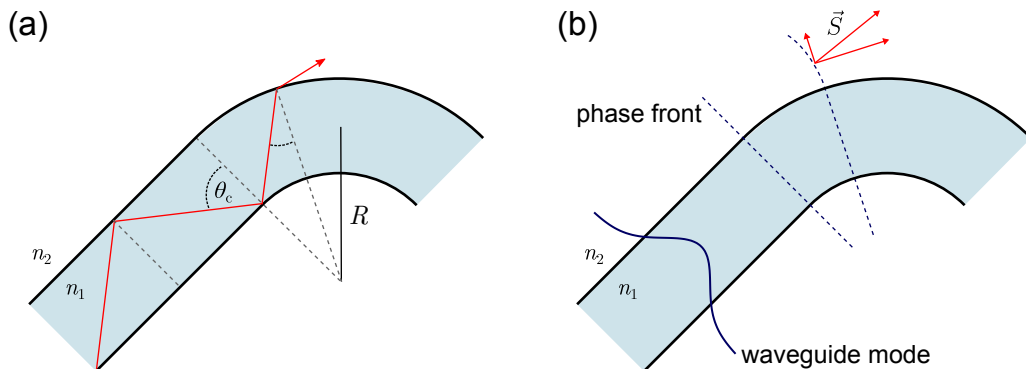


**Figure 1.5:** Origin of energy loss in a bent waveguide. (a) Ray optics: The condition for total internal reflection is not satisfied anymore when a beam hits a concave surface. (b) Wave optics: The phase-front is trailing behind in the cladding due to an increased path length and a finite speed of light. Dissipation of energy is caused by an emerging radial component of the Poynting vector  $\vec{S}$ .

The pure bend losses of a step-index waveguide were derived by [Gam78b] to be

$$\text{BL}(R) = \frac{1}{2} \left( \frac{\pi}{aw^3} \right)^{1/2} \left( \frac{u}{VK_1(w)} \right)^2 \frac{1}{\sqrt{R}} \exp \left( -\frac{4}{3} \frac{\Delta n}{n_1 a V^2} w^3 R \right), \quad (1.15)$$

with the bend radius  $R$  and all other variables as previously defined (see Section 1.1.2). Figure 1.6 shows some exemplary bend loss curves which were calculated for a waveguide with a core radius of  $3 \mu\text{m}$  at a wavelength of  $638 \text{ nm}$ . It becomes clear how the tolerable radii of curvature depend on the magnitude of the index

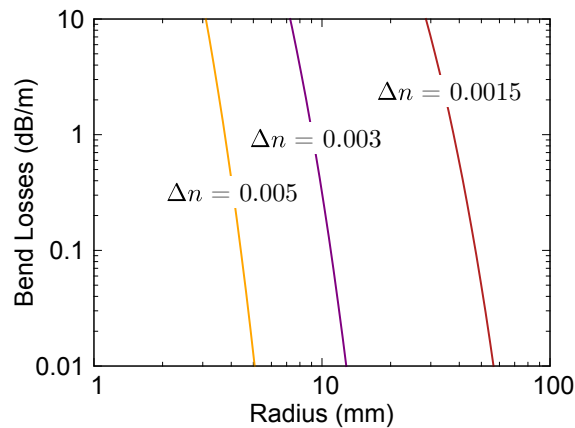


**Figure 1.6:** Bend losses at 638 nm for a waveguide with a core radius of  $3\ \mu\text{m}$  and index contrasts of  $\Delta n = 0.0015, 0.003,$  and  $0.005$  compared to a cladding with  $n = 1.5$ . The curves were calculated based on Equation (1.15).

contrast  $\Delta n$ . It has to be kept in mind that the bend losses are given per unit length. If the purpose of a bend is to change the direction of propagation, higher bend losses might be tolerable since the length of a curved segment also gets shorter when the radius of curvature decreases.

Aside from the energy loss during propagation in a bend, it has been shown that considerable transition losses may occur at the transition point of a straight and a curved segment [Gam78a]. The field distribution is shifted in a curve and leads to a mode mismatch which causes scattering of light. The magnitude of the mode mismatch is also strongly related to the radius of curvature. Investigating sinusoidal curves, it was experimentally demonstrated that if the radius of curvature is increased continuously, the transition losses decrease and the occurring dissipation of energy can be considered as pure bend losses [Gam78b].

#### 1.1.4 Evanescent coupling

When two waveguides are close to each other so that their evanescent fields overlap, light can be coupled from one waveguide to the other. This process is schematically depicted in Figure 1.7. The formal approach to calculate the propagation of light in both waveguides would be to evaluate Maxwell’s equations for the entire system with appropriate boundary conditions. The modes of the overall system would be different from the modes of an isolated waveguide and an exact solution is very complicated. For weak coupling, a simplified approach known as “coupled mode theory” is often sufficient [Sal07]. It assumes that the overall electric field may be

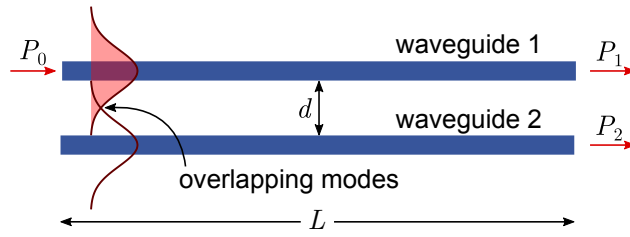


**Figure 1.7:** Schematic of evanescent coupling between waveguides. The power  $P_0$  is coupled from waveguide 1 into waveguide 2 due to overlapping waveguide modes. The output powers  $P_1$  and  $P_2$  depend on the distance  $d$  and the coupling length  $L$ .

expressed as a linear combination of the individual waveguide modes with changing amplitudes  $A_{1,2}$ ,

$$E(x, y, z) = A_1(z)E_1(x, y)e^{i\beta_1 z} + A_2(z)E_2(x, y)e^{i\beta_2 z}. \quad (1.16)$$

Assuming that the electric field of waveguide 1 induces small perturbations to the electric field of waveguide 2 and vice versa, solving the wave equation with a source leads to the following set of coupled differential equations:

$$\begin{aligned} \frac{dA_1(z)}{dz} &= -i\mathcal{C}A_2(z)e^{i\Delta\beta z}, \\ \frac{dA_2(z)}{dz} &= -i\mathcal{C}A_1(z)e^{i\Delta\beta z}, \end{aligned} \quad (1.17)$$

with  $\Delta\beta = \beta_1 - \beta_2$  and a coupling coefficient  $\mathcal{C}$  which is proportional to the overlap integral

$$\mathcal{C} \propto \int E_1(x, y)E_2(x, y)dx dy. \quad (1.18)$$

Solving these equations for identical waveguides ( $\Delta\beta = 0$ ) and applying the relation for transmitted power  $P \propto |A|^2$  yields the simple solution:

$$\begin{aligned} P_1(z) &= P_0 \cos^2(\mathcal{C}z), \\ P_2(z) &= P_0 \sin^2(\mathcal{C}z). \end{aligned} \quad (1.19)$$

At a length  $L_0 = \pi/2\mathcal{C}$ , the energy is completely transferred from one waveguide to the other, as shown in Figure 1.8(a). For instance, this mechanism may be used to assemble directional x-couplers. An example for a 50:50 beam splitter with length  $L_0/2$  is schematically depicted in Figure 1.8(b).

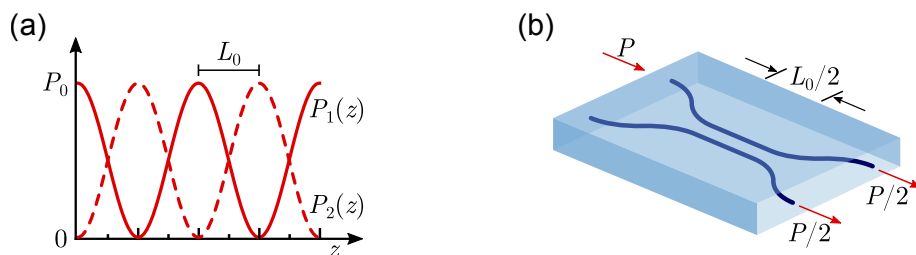


**Figure 1.8:** (a) Output powers  $P_1(z)$  and  $P_2(z)$  of coupled identical waveguides according to Equation (1.19). (b) A directional x-coupler, with 50:50 split ratio.

## 1.2 Femtosecond laser-material interaction

The fundamental properties of laser light make it an ideal tool for material processing. Spatial coherence leads to a diffraction-limited narrow beam which can be focused to a very small spot which exhibits a high local irradiance. If the photons have enough energy ( $E_{\text{ph}} = h\nu$ ) to overcome the band gap  $E_g$  of a material, it can be ionized by linear absorption. This mechanism may be used, e.g., for surface structuring or cutting. In order to create local modifications inside the bulk material, photons with energies below the band gap ( $E_{\text{ph}} < E_g$ ) and higher laser intensities are necessary. Present-day pulsed laser systems offer extremely high peak-intensities and can easily reach  $10^{\text{TW}}/\text{cm}^2$  when tightly focused [Ose12]. At these intensities, strong nonlinear photoionization occurs and energy is deposited very locally in a bulk of a material which is otherwise transparent for the present light. Moving a substrate relative to the focused laser beam now enables three-dimensional microstructuring. This technique opens up a huge field of research in processing of glasses, crystals or polymers with visible or near-infrared light, e.g., waveguide writing, two-photon polymerization, Bragg grating inscription, microfluidic channel fabrication and welding [Ose12].

This section will describe the physical mechanisms underlying femtosecond laser micromachining. It will especially focus on the interaction of femtosecond laser pulses with matter and on the origins of refractive index changes in a substrate – particularly in polymers – which is the foundation for waveguide writing.

### 1.2.1 Nonlinear photoionization

Two competing processes may cause nonlinear photoionization: Tunnel ionization and multiphoton absorption. Tunnel ionization results from the presence of strong laser fields which distort the band structure of the medium. An electron may then tunnel through the reduced potential barrier from the valence band into the con-

duction band. This effect is schematically depicted in Figure 1.9(a). At low laser intensities and high photon energies – but below the frequency for linear absorption – multiphoton absorption may occur. A number of photons  $n_{\text{ph}}$  has to satisfy

$$n_{\text{ph}} E_{\text{ph}} > E_g \quad (1.20)$$

to ionize an electron. Multiphoton absorption may be thought of as a process with intermediate virtual states. Heisenberg's uncertainty principle yields  $\Delta E \Delta t \geq \hbar/2$ , thus, if  $\Delta t$  is very small, the energy uncertainty  $\Delta E$  is very large. In multiphoton absorption, one electron is promoted to the broadened conduction band for a very short period of time. Within this time frame, the additionally needed photons have to be absorbed to ionize the electron. The process is schematically depicted in Figure 1.9(b).

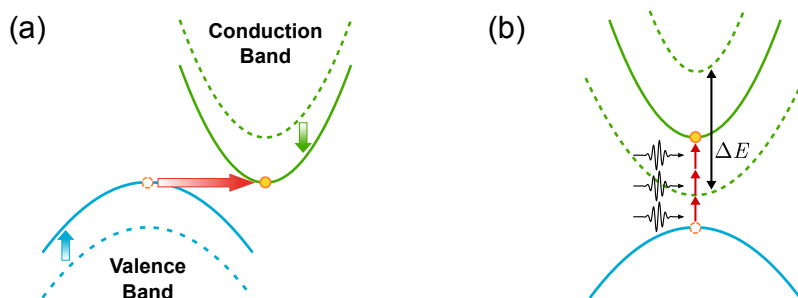


**Figure 1.9:** (a) Tunnel ionization: A strong electric field distorts the band structure and an electron can tunnel through the reduced band gap. (b) Multiphoton ionization: A number of photons is simultaneously absorbed to overcome the band gap. The green dashed lines indicate a broadened conduction band due to the uncertainty principle.

The transition between both processes is estimated by the Keldysh parameter

$$\gamma = \frac{\omega}{e} \sqrt{\frac{m_e c n \epsilon_0 E_g}{I}}, \quad (1.21)$$

where  $\omega$  is the angular laser frequency,  $e$  is the electron charge,  $m_e$  is the effective electron mass,  $c$  the vacuum speed of light,  $n$  the linear refractive index,  $\epsilon_0$  is the permittivity of free space and  $I$  the intensity at the focal spot. Multiphoton absorption is the dominant effect for  $\gamma \gg 1.5$  and tunnel ionization for  $\gamma \ll 1.5$ . Typical material characteristics and laser parameters for femtosecond laser micromachining applications in dielectrics yield a Keldysh parameter in the order of  $\gamma \approx 1.5$  which means that both processes contribute to the ionization event [Sch01].

Electrons promoted to the conduction band via nonlinear photoionization can continue to absorb energy linearly by free carrier absorption. If an electron consecutively

absorbs several photons, its kinetic energy may exceed the band gap energy. Such an electron becomes a so-called hot electron which can promote another bound electron from the valence band to the conduction band via impact ionization, schematically shown in Figure 1.10. These two free electrons may continue to linearly absorb photons and the process repeats itself as long as an electric field is present, ultimately producing an electron avalanche which ignites a plasma. The formation of a plasma in a medium by laser irradiation is also called optical breakdown.

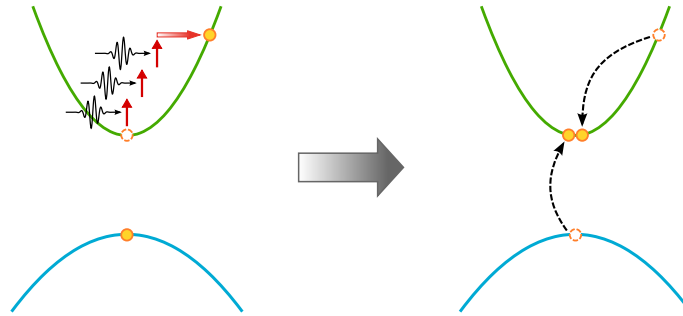


**Figure 1.10:** Schematics of avalanche ionization: A promoted electron continues to absorb photons linearly and can impact ionize a bound electron from the valence band when it has sufficient kinetic energy.

Whether avalanche ionization occurs strongly depends on the pulse duration and the band gap of the material [Len98]. Assuming a homogeneous and isotropic crystal without defects, numerical simulations have shown that for sub-100 fs pulse duration, impact ionization is of minor importance and nonlinear photoionization alone creates a free electron gas [Kai00]. Regarding the band gap of a material, it has been reported that for small band gaps, nonlinear photoionization is responsible for a significant amount of free electrons while for large band gaps, avalanche ionization is dominant [Sch01].

### 1.2.2 Energy distribution processes

The process of femtosecond laser material modification can be divided into three steps: the formation of a free-electron plasma (see Section 1.2.1), the heating of the material and finally the manifestation of a structural modification. The timescale of these three steps and the relevant physical effects are visualized in Figure 1.11.

Even though the pulse duration is in the order of tens to hundreds of femtoseconds, the material may still undergo changes microseconds after the absorption of photons. After the ignition of a plasma in the focal volume, a part of the energy is already transferred to the lattice via electron-phonon scattering on a sub-picosecond



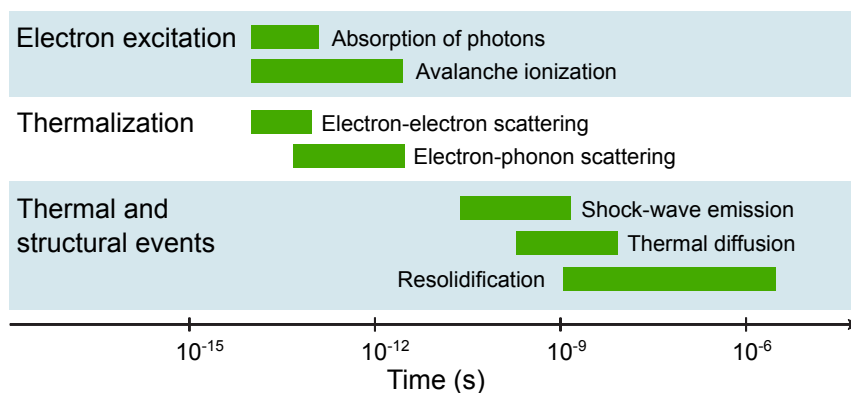


**Figure 1.11:** Typical time scales of relevant physical phenomena occurring during and after the interaction of a femtosecond laser pulse with a transparent material. Schematic based on [Gat08].

timescale. At high plasma temperatures, which result from high intensities, the pressure in the focal volume can be in the order of GPa [Gle97]. This pressure may cause a micro-explosion and a resulting shock-wave gets emitted within a few nanoseconds [Sak07]. When sufficient energy is deposited in the material permanent damage occurs in the form of cracks or voids. The thermal energy diffuses out of the focal volume into the bulk material on the microsecond scale. At sufficiently high energy, these thermal processes cause melting in the vicinity of the focal volume [Miy14].

As can be seen in Figure 1.11, the processes do not occur strictly sequentially but instead partially overlap which makes the overall energy distribution highly complex and sensitive to many parameters. It also becomes very difficult to study the processes independently from one another. In waveguide writing applications, a series of pulses which spatially overlap in the material are necessary to create a continuous track of refractive index modification. In this case, cumulative effects have to be considered. Further discussion on the accumulation of heat can be found in Section 1.3.1.

### 1.2.3 Origins of refractive index change

The processes of nonlinear photoionization and plasma formation will cause structural modifications in a material as was described in the previous section. These modifications may manifest in the form of local changes in refractive index. The morphology and magnitude of these changes strongly depend on the target material and laser properties. While a universal model to describe all the physical processes during femtosecond laser-material interaction is still an open question, individual effects contributing to a refractive index change have been identified. Working below

or above the damage threshold of a material defines Type I and Type II material modifications [Gro15]. In the following, the mechanisms in these two modification regimes will be discussed with respect to the target material and irradiation parameters.

### Glasses and crystals

Already early works have assumed densification of the material as a main mechanism for refractive index increase in the irradiated zone [Hir98]. It was believed that this densification may be accompanied by various other phenomena such as the formation of color centers and lattice defects [Mus11]. The existence of color centers was confirmed and found to be correlated with  $\Delta n$  [Str02]. However, the color centers vanished when the material was annealed while the refractive index change persisted. Therefore, color centers were ruled out as cause of the index modification. Working in a Type I energy regime in which structural damage and void formation are avoided, densification was reported as the sole mechanism responsible for the refractive index increase in glass as well [Pon08]. This observation is supported by pump-probe single-shot experiments which showed that fused silica is only densified along a plasma string triggered by nonlinear photoionization. The structural rearrangement of the material is attributed to gradually decaying electronic defect states caused by electrons trapped in excitons. Thermal effects were found negligible for single-pulse modifications and it was estimated that they will only become relevant above 100 kHz repetition rate [Pap11]. When thermal effects become relevant, the densification effect is attributed to rapid cooling of molten glass in the focal volume [Dub14]. Regarding crystalline materials, an increase in refractive index induced directly in the focal volume could also be observed in  $\text{LiNbO}_3$  [Bur07]. However, it only existed along one particular crystal axis and was unstable towards annealing.

At higher pulse energies in the Type II modification regime, an expansion of the lattice may be induced in the directly irradiated volume, which can also lead to micro-explosions and the emission of a shock-wave (see Section 1.2.2). This process may result in strong material damage in the focal volume or even void formation [Juo06]. The surrounding regions may however possess a relatively high refractive index due to stress related effects [Bur07]. Working above the damage threshold proves beneficial to create stable index modifications in crystals since a positive  $\Delta n$  typically requires an increase in material density and the crystalline structure naturally provides a greater positional order than amorphous materials. Although the response of a crystalline material to high power femtosecond laser irradiation depends on the crystal in use, some modification characteristics are quite general

[R609]. The focal volume is left with irreversible lattice damage, thermally removable defects and lattice imperfections in the vicinity. The surrounding areas display compressed crystalline material with a positive  $\Delta n$  which is thermally stable.

## Polymers

The mechanisms for refractive index change induced by femtosecond laser irradiation in polymers are more complex and several additional effects have to be taken into account. A polymer is a chemical compound consisting of macromolecules which are build up by many repeating subunits. Femtosecond laser pulses may cause chain scission and result in the decomposition of the polymer. This process is also called unzipping. In addition, the damage threshold is at least one order of magnitude smaller than for glass.

PMMA is a commonly available polymer and is used in the vast majority of reported work. It serves as a generic example for other polymers. In a study on the photochemistry of femtosecond laser induced index modifications, a broadening of the molecular weight distribution was observed, indicating the scission of the polymer backbone which causes depolymerization and the formation of MMA monomers [Bau07]. In a follow-up study, it was shown that an increase in refractive index in PMMA is caused by a combination of depolymerization and crosslinking [Bau10]. It was also demonstrated that an increased UV absorption due to a large number of end groups can cause an increase of the refractive index in the visible spectrum.

When thermal effects become dominant, ablative-type mechanisms, thermal unzipping and damaged structures are main modification processes [Eat12]. A decrease in refractive index in the directly irradiated volume surrounded by a ring-shaped area of increased refractive index was reported in [Zou04]. This observation was interpreted as thermal expansion of the core that compresses the material outwards. The formation of MMA monomers through thermal unzipping was believed to additionally decrease the refractive index in the center. The magnitude of the refractive index increase was linked to the pulse duration in some studies, with shorter pulses leading to a larger  $\Delta n$  [Bau08]. In some cases it was reported that repeated irradiation increases the magnitude of the refractive index modification [Scu03, Bau08] while others observed damage as a result of irradiating existing material modifications multiple times [Sow06].

Temporal dependence of the refractive index modification was observed on multiple occasions. In a study on femtosecond laser structured volume phase gratings a decay of the diffraction efficiency – and therefore  $\Delta n$  – was observed over a period of weeks. It was attributed to photoinduced MMA monomers which are soluble in

PMMA and diffuse into the bulk [Liu10]. An initially negative index modification that became a permanent positive  $\Delta n$  after 20 minutes was reported in [Wat06]. This effect was interpreted as a gradual release of tensile and compressive stress which was caused during laser fabrication. However, this observation could not be reproduced by a second group, despite working with a similar setup [DM11].

Regarding void formation in the irradiated medium, it was found that a cavity can form at around the focal volume when exposed to a series of femtosecond laser pulses [Zhe15a]. The cavity is believed to form when the irradiated region is heated up beyond the temperature for random chain scission [Zhe15b]. Surrounding the spherical cavity is a zone affected by melting due to heat accumulation in the material. This zone displays an increased refractive index. An SEM image is reproduced in Figure 1.12. It shows the exposed cavity and the zone affected by melting.

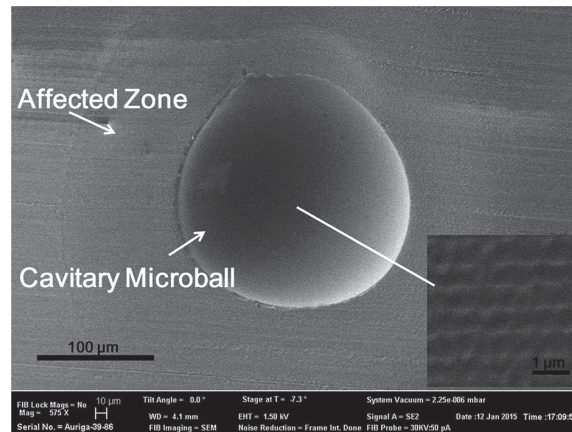


**Figure 1.12:** SEM image of a microball cavity in PMMA created by high power femtosecond laser pulses. Visible is also a zone affected by melting and resolidification around the cavity with an increased refractive index. Figure taken from [Zhe15a].

So far, the observed changes in chemical composition alone cannot fully explain the maximum observed index modification of up to  $\Delta n = 4 \cdot 10^{-3}$  [Bau10]. At the same time, a refractive index increase in zones affected by melting around micro cavities fabricated via stationary exposure were observed in PMMA. Refractive index increases in polymers can therefore be assumed to be a combination of densification and stress related effects, as well as changes in molecular composition.

## 1.3 Femtosecond laser waveguide writing

To create an embedded waveguide in a dielectric medium, the substrate needs to be translated relative to the femtosecond laser beam so that a continuous track of refractive index modification may form. This process is typically called waveguide writing. The feasibility of this technique was demonstrated in glass for the first time in 1996 [Dav96]. Femtosecond laser waveguide writing has since then become a versatile field of research with hundreds of publications [Ose04, Nol03]. It has some clear advantages over other fabrication techniques for planar waveguide networks, such as photolithography, sputtering or embossing:

- It is a direct fabrication technique which does not require specific masks for every desired geometry. This feature is especially advantageous for rapid prototyping applications and on-demand production. In addition, it is a one-step process.
- It has full 3D capabilities and virtually arbitrary structures can be created inside a sample. With modern positioning systems, accuracy on a nanometer scale is achieved. Therefore, multiple structures may be positioned relative to one another with very high precision.
- The technique is highly flexible and reproducible. The same setup can be used for different materials, e.g., glasses, crystals and polymers. It may also be combined with other femtosecond laser micromachining techniques, such as surface ablation/structuring, micro-channel fabrication and 2PP, with little to no adjustments (see Section 1.4).

The following section will focus on the experimental details of femtosecond laser waveguide writing, possible waveguide geometries and an overview of functional waveguides in polymers.

### 1.3.1 Irradiation parameters

As already mentioned in the previous sections, a large number of parameters affect the refractive index modification in an irradiated dielectric material. Here, the most important experimental parameters for the writing process will be discussed.

#### **Femtosecond laser source**

First of all, the wavelength has to be in the optical transparency regime of the target material to avoid linear absorption which would lead to an entirely differ-

ent light matter interaction and material modification. Commonly used systems are: Ti:sapphire sources ( $\lambda \approx 800$  nm) which, due to their broad gain spectrum, can easily provide sub-100-femtosecond pulses [Mor99] and Yb-based laser sources ( $\lambda \approx 1000$  nm) which usually deliver longer pulses but offer more flexibility regarding the repetition rate [Kil04]. Frequency doubling proved beneficial for the waveguide quality in some instances [Sha05] but in general, the exact wavelength does not appear to be a critical parameter.

The repetition rate of the laser source is a key parameter and establishes two fundamental writing regimes: single-pulse and heat accumulation regime. In the single-pulse or athermal regime, the time between two consecutive pulses is long enough for the deposited thermal energy to fully diffuse out of the focal volume, as shown in Figure 1.13(a). When, on the other hand, the time interval between two laser pulses is too short for complete diffusion, heat gets accumulated as shown in Figure 1.13(b). This condition is called heat accumulation or thermal regime. Working in the heat accumulation regime has the advantage of enabling higher processing speeds and decreases thermal cycling. However, the build up of heat in the focal volume can significantly increase the size of the laser modified structure [Eat05]. Heat accumulation and thermal diffusion depend very much on the focusing conditions and the material properties, making it difficult to define a universal transition value. Since thermal effects typically take place on the microsecond scale (see Section 1.2.2), the athermal regime can be estimated to be located in the kHz-range and the thermal regime in the MHz-range. More control over the heat accumulation process may be obtained by utilizing the burst-mode concept [Gat06], where a variable number of pulses is picked from a high repetition rate pulse train with a variable burst repetition rate.

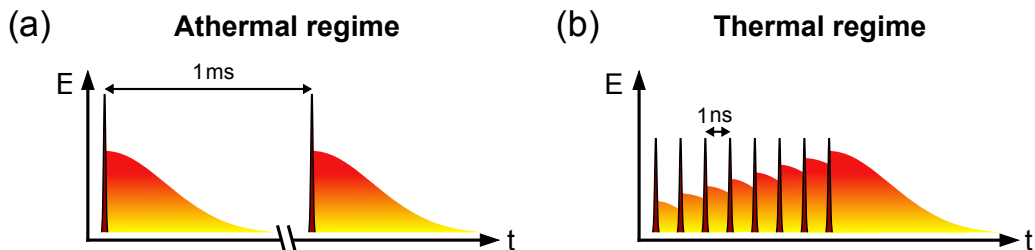


**Figure 1.13:** (a) Athermal regime: A low repetition rate results in single pulse modification. (b) Thermal regime: A high repetition rate enables heat accumulation.

Aside from the repetition rate  $f_{\text{rep}}$ , another essential parameter is the pulse energy  $E_p$ . In combination with the pulse duration  $\tau$ , it determines the peak intensity. The following simple equations relate these physical values:

$$E_p = \frac{P}{f_{\text{rep}}}, \quad (1.22)$$

$$P_{\text{peak}} = \alpha \frac{E_p}{\tau} = \alpha \frac{P}{\tau f_{\text{rep}}}. \quad (1.23)$$

The average power  $P$  is directly measurable with an integrating powermeter and  $\alpha$  is a dimensionless coefficient depending on the temporal shape of the pulse. A Gaussian-shaped pulse for example yields  $\alpha \approx 0.94$ . The fluence  $F$  is defined as the optical energy delivered per unit area

$$F = \frac{E_p}{A} = \frac{P}{A f_{\text{rep}}}, \quad (1.24)$$

and the peak intensity is related to the peak power via

$$I_{\text{peak}} = \frac{P_{\text{peak}}}{A} = \alpha \frac{E_p}{A \tau}. \quad (1.25)$$

The focal spot area is given by  $A = \pi \omega_0^2$ , with  $\omega_0$  being the beam waist at the focus. Also of great importance is the speed  $v$  with which the sample is translated since it defines the number of overlapping pulses per volume. For example, a translation speed of 1 mm/s at a repetition rate of 1 MHz results in 1000 pulses overlapping over a distance of 1  $\mu\text{m}$ . Finally, the energy dosage in units of energy per volume is defined as

$$D = \frac{E_p f_{\text{rep}}}{A v}. \quad (1.26)$$

It is the three-dimensional counterpart to the fluence [Zou05].

## Focusing

Since the conditions for nonlinear photoionization are only reached at the focus, the intensity distribution of the laser beam in the focal volume can be of the uttermost importance in waveguide writing.

Using the paraxial approximation of the Helmholtz equation gives the spatial dimension of a focused Gaussian beam in a medium with refractive index  $n$ . The waist  $w_0$  at the focal spot is then given by

$$w_0 = \frac{M^2 \lambda}{\pi \text{NA}}, \quad (1.27)$$

with NA being the numerical aperture of the focusing objective and  $\lambda$  the wavelength in free space. The beam quality factor  $M^2$  characterizes the deviation of a laser beam from a diffraction limited Gaussian beam [Wil02]. The Rayleigh range  $z_r$  is given by

$$z_r = \frac{M^2 n \lambda}{\pi \text{NA}^2}. \quad (1.28)$$

The confocal parameter is defined as  $2z_r$  and the spot size is given by  $2w_0$ . Deviations in the intensity distribution close to the focal spot may be caused by spherical or chromatic aberrations to a degree where the approximations of Equation (1.27) and 1.28 are no longer valid.

When focusing from air into a bulk material of refractive index  $n$ , refraction at the interface has to be taken into account. First of all, refraction leads to a larger effective focusing depth  $d_{\text{eff}} = d \cdot n$ , as depicted in Figure 1.14(a). Secondly, it causes additional spherical aberration resulting in a deformation of the intensity distribution in the focal spot. With increasing focusing depth and numerical aperture of the focusing lens, this effect results in an increased Rayleigh range and deformation of the intensity distribution primarily in the axial direction as depicted in Figure 1.14(b) [DB07, Mau08].

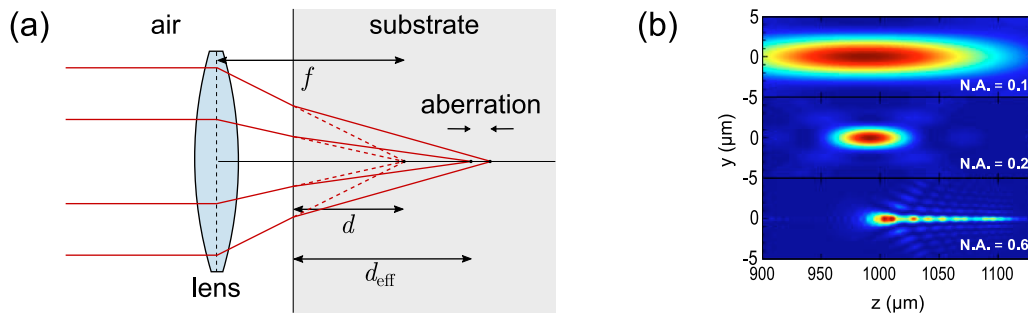


**Figure 1.14:** Schematic depiction of focusing from air into a medium with higher refractive index. Results are a higher effective focusing depth and additional spherical aberration. (b) Simulated intensity distribution of 800 nm light focused 1 mm below the surface of glass for NA = 0.1, 0.2 and 0.6, taken from [DB07].

Spherical aberration can be compensated to some degree by using multiple lenses, as it is the case for microscope objectives, or can be prevented by using aspheric focusing lenses. Chromatic aberration can be corrected by microscope objectives which are composed of lenses with specially designed dispersion properties. Additional dispersion, however, also affects the pulse duration when working with an ultra short laser source and may demand for compensation of these effects [Emo12].



## Non-linear propagation

When light propagates through a medium at high intensities, nonlinear effects occur. The Kerr effect is the change of refractive index proportional to the intensity, with the nonlinear refractive index  $n_2^I$  being the proportionality factor. Since  $n_2^I$  is positive for most materials, the refractive index at the center of a Gaussian laser beam is higher than on the outside. This refractive index gradient acts as a lens on the beam, a so-called Kerr lens. The strength of the focusing depends on the peak power. With decreasing beam radius the intensity increases and therefore the lensing effect as well. The result is further self-focusing which can lead to a collapse of the beam when the peak power of the pulse exceeds the critical power [Fib00]

$$P_{\text{crit}} = \frac{3.77\lambda^2}{8\pi n_0 n_2^I}. \quad (1.29)$$

This collapse may lead to very high intensities which can nonlinearly ionize the medium (see Section 1.2.1). The emerging free electron plasma diverges the beam and counteracts the Kerr lens. A balance between both effects can lead to filament propagation which results in elongated material modification in the propagation direction [Che14]. A microscope image of this effect is reproduced in Figure 1.15. If this effect is to be avoided during waveguide fabrication, one needs to tightly focus the laser beam so that it reaches intensities for nonlinear photoionization without exceeding the critical power. Filamentation during waveguide writing in polymers was, for example, reported in [Wat09].

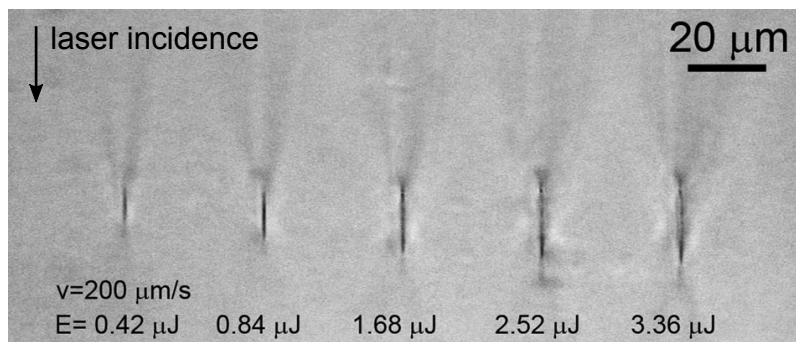


**Figure 1.15:** Microscope image of the cross section of modification tracks written in Nd:YAG. At larger peak powers the vertical dimension of the structures increases due to self-focusing and filamentation. Figure taken from [Che14].

### 1.3.2 Writing configuration

In ultrafast laser waveguide fabrication, two standard writing configurations are distinguished depending on the direction of sample movement relative to the laser incidence.

#### Longitudinal writing

In the case of longitudinal writing, the sample is scanned parallel to the laser beam as depicted in Figure 1.16(a). Assuming a Gaussian beam profile, the clear advantage of longitudinal writing is the resulting cylindrical symmetry of the waveguide. At the same time, a major disadvantage is the limitation of waveguide length by the working distance of the focusing objective. There exist special long working distance objectives which can compensate this drawback to some degree. Also writing is limited to one direction: from bottom to top. Otherwise, the light would have to propagate through modified material which it has previously created, which would distort the beam significantly. It also has to be considered that the amount of material the beam needs to propagate through before it reaches the focal spot constantly changes during the writing process. The position of the focus relative to the surface of the sample may have a considerable influence on the intensity distribution at the focal volume (see Section 1.3.1).

#### Transverse writing

In a transverse writing configuration, the sample is scanned perpendicularly to the laser incidence and the length of a waveguide is no longer restricted. Since the working distance of an objective usually surpasses the thickness of the sample, virtually any arbitrary three-dimensional structures may be created inside the sample.

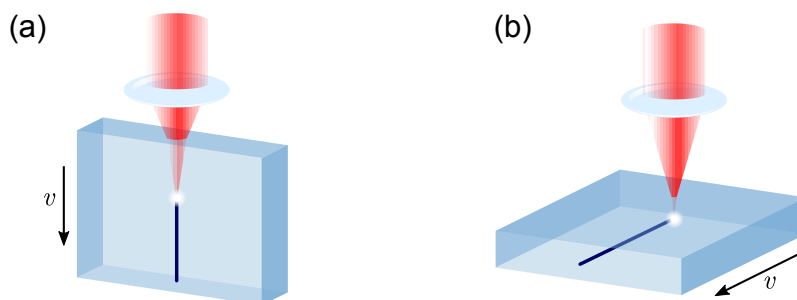


**Figure 1.16:** (a) Longitudinal writing: The sample gets scanned parallel to laser incidence. (b) Transverse writing: The sample is scanned perpendicularly to the laser incidence.

However, in this configuration, the axial intensity distribution of the focused writing beam may have a defining influence on the cross section of the resulting waveguide. The ratio of depth of focus and spot size is derived from Equations (1.27) and (1.28) to be

$$\frac{z_r}{w_0} = \frac{n}{\text{NA}} . \quad (1.30)$$

Typical values of  $n = 1.5$  for glass and NA between 0.2 and 0.8 (assuming simple focusing conditions without immersion oil) give ratios between 1.875 and 7.5. This results in elliptical waveguides which are often undesirable. The asymmetry can be decreased by high NA focusing which will reduce the size of the waveguide at the same time. The reduced size, on the other hand, becomes problematic if guiding at large wavelengths is to be supported, e.g., in telecommunication applications,  $\lambda = 1.5 \mu\text{m}$  is typical. If working in the heat accumulation regime (see Section 1.3.1) is possible, asymmetric waveguides may be prevented. Since heat diffusion, which intrinsically displays radial symmetry, becomes a dominant effect, resulting waveguides exhibit an almost circular cross section [Eat05]. For all other cases, beam shaping techniques may be applied (see Section 1.3.3).

The vast majority of experimental work nowadays applies the transverse writing geometry.

### 1.3.3 Beam shaping

The intensity distribution of the focused writing beam may lead to waveguides with elliptical cross section when working in the athermal regime with transverse writing configuration (see Section 1.3.2). The axial beam evolution of a focused symmetric Gaussian beam and the resulting material modification are shown in Figure 1.17(a) and (b), respectively. To overcome this asymmetry, beam shaping techniques may be applied to control the shape of the focus. The goal is to achieve an intensity distribution along the propagation axis as close to circular symmetry as possible.

One possibility is astigmatic beam shaping. The idea is that in transverse writing geometry, the focal size in the direction along which the sample is translated (x-direction) is irrelevant. Focusing very tightly in x-direction increases the divergence in the x-z-plane which lets the intensity quickly decline below the threshold for nonlinear photoionization, resulting in a reduced depth of focus. This technique was first demonstrated using a cylindrical telescope to create an astigmatic beam, resulting in symmetric fundamental-mode waveguides for  $1.5 \mu\text{m}$  wavelength in glass [Cer02, Ose03]. A simpler approach to obtain an elliptical writing beam uses a slit in front of the focusing objective. The resulting loss in power of the writing beam

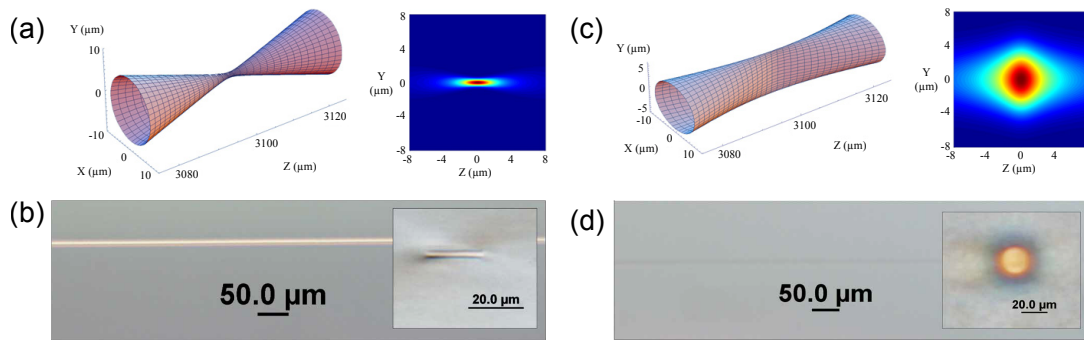


**Figure 1.17:** (a) Beam evolution of a focused symmetric Gaussian beam and energy distribution in the y-z-plane and (b) corresponding material modification. (c) Beam evolution of a focused elliptical beam and (d) resulting symmetric waveguide. Figures taken from [Ams05].

needs to be compensated by higher initial pulse energies in this case. The feasibility of this technique to create low-loss symmetric waveguides for the telecommunication wavelength was reported in [Ams05]. Figure 1.17(c) shows the evolution of a focused elliptical beam which leads to a more spherical intensity distribution in the y-z-plane at the focal spot. The result is a symmetric waveguide when scanning the sample in x-direction as can be seen in Figure 1.17(d). Other possibilities to introduce the necessary astigmatism to the beam are the use of deformable mirrors [Tho08] or a spatial light modulator (SLM) [Cru09, Sal12]. To really achieve a spherical focal volume, spatio-temporal focusing may be applied. The frequencies get dispersed by a prism or a grating and are recombined spatially and temporally only in the focal spot, resulting in a spherical modification [He10].

### 1.3.4 Track morphology

Aside from homogeneous material modification tracks, the structural alterations can manifest in various other morphologies such as periodic and non-periodic modulations. Spatio-temporal distortions, which are common to ultrashort laser pulses, may play a major role in these effects which may be observed in all target materials. However, to reduce scattering losses, smooth material modifications are preferred for waveguide writing.

A sharp transition from smooth structures to pearl-chains was observed in fused silica with increasing pulse energy [Gra07]. As a possible mechanism it was suggested that at a certain size an emerging material modification scatters so much light and distorts the beam in a way that the absorption drops. Since the sample is continuously translated through the focus, the absorption increases again as

soon as the light hits unmodified material and the process repeats itself periodically. An alternative explanation features hydrodynamic instability. It is assumed that a melted volume of liquid glass spontaneously decays into drops, much like a water jet in air, because of small periodic perturbations and the energetically favorable shape of a liquid drop [Gra07]. It was reported that the periodic and non-periodic disruptions in fused silica have a foam-like inner structure with cavities up to  $2\ \mu\text{m}$  [Ric13]. The formation of these disruptions was found to strongly depend on the writing parameters. They are periodic when written close to the surface and become chaotic with increased writing depth. The mechanism is believed to be caused by interruptions of the heating process through aberrations of the laser beam which result in rapid quenching of the material. Similar pattern formation was also observed in PMMA [Tho13a]. A microscopy image is reproduced in Figure 1.18 displaying pattern formation and writing anisotropy.

Despite the symmetry of a Gaussian laser beam, it was observed that the properties of laser induced tracks in an isotropic medium can depend on writing direction. This can obviously be a result of pattern formation where the writing direction also affects the position where the modification process is interrupted. But writing anisotropy may also be the result of a spatial frequency chirp which results in a pulse front tilt: a tilt in the intensity distribution which is a common phenomena in femto-second laser systems [Akt03]. In the presence of an intensity gradient, charges such as the free electrons present during ultrafast laser micromachining experience the ponderomotive force which moves them towards lower intensities [Kaz07], resulting in anisotropy effects during writing. A directional dependence of the birefringence of the material modification as well as nano-gratings at the center of the structures were reported in [Kaz07]. This effect was named “Quill writing” because of its resemblance to writing with a quill pen. By adjusting the pulse front tilt, control over this anisotropy was demonstrated and anisotropic bubble formation was observed [Yan08a, Yan08b].

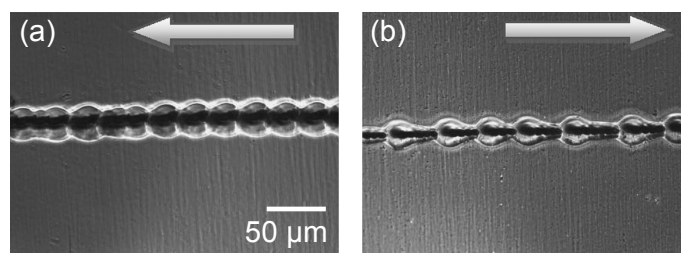


**Figure 1.18:** Pattern formation and writing anisotropy in PMMA. The arrows in (a) and (b) indicated the writing direction respectively, taken from [Tho13a].

### 1.3.5 Waveguide geometries

Up to this point a femtosecond laser written waveguide was considered to directly emerge from a refractive index increase caused by a single modification track. This geometry is therefore called single-track waveguide in the following and is once again depicted in Figure 1.19(a). The advantage of this geometry is that it can directly be used to build up three-dimensional structures, y-junctions, x-couplers or waveguide arrays. But there exists a large geometrical variety of waveguide structures based on the assembly of multiple modification tracks which can be applied if the single-track approach is insufficient for a given material or task.

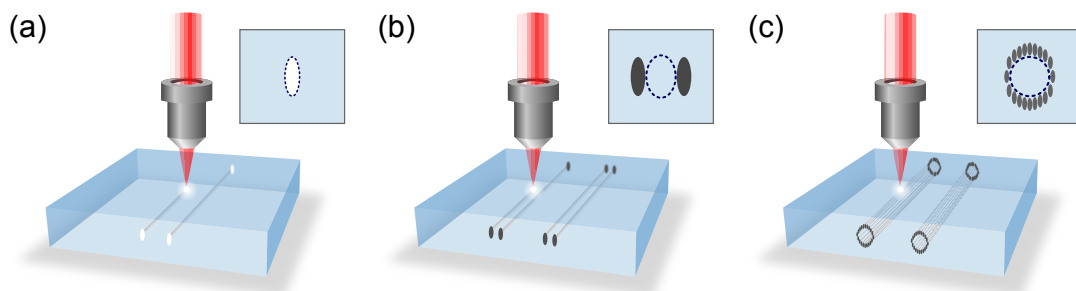


**Figure 1.19:** Schematic depiction of various waveguide geometries. The dashed lines indicate the waveguide core. (a) Single-track waveguide: A positive refractive index modification emerges directly in the focal volume and the track itself forms the waveguide core. (b) Dual-track waveguide: Zones of increased refractive index in the vicinity of two damage tracks are overlapped. The waveguide core is located between the tracks. (c) Depressed cladding waveguide: A number of modification tracks which exhibit a decrease in refractive index are symmetrically aligned around the waveguide core.

#### Dual-track waveguide

As described in Section 1.2.3, working in a pulse energy regime above the damage threshold may lead to an expansion of the lattice in the focal volume which is typically accompanied by material damage. The surrounding areas, on the other hand, may exhibit a relatively high increase in refractive index through compression and stress-related effects. With adequate spacing, lateral stress fields of two adjacent tracks may be overlapped to form a waveguide core, as demonstrated for the first time in [Bur06]. A schematic depiction of a so-called dual-track waveguide can be seen in Figure 1.19(b). One advantage of this geometry is that the cross-sectional dimensions of the guided mode may be controlled to some extent by the spacing between the tracks. This waveguide geometry is commonly used for ultrafast writing in

crystalline materials which typically require high pulse energies to achieve adequate refractive index modifications. In crystals, the dual-track geometry presents some additional advantages. Since the core of the waveguide lies between two modification tracks, the bulk characteristics of the material are only slightly affected there. This holds especially for the luminescence and nonlinear properties [Zha11, R609]. The conservation of these properties make applications such as frequency doubling [Bur06] or electro-optic modulation [Hor12] in a waveguide feasible. The guiding capabilities for this geometry may also be polarization dependent for some target materials [Sie10].

### **Depressed cladding waveguide**

A depressed cladding waveguide is built up by multiple modification tracks which exhibit a decreased refractive index. They are symmetrically aligned around the desired waveguide core in a way that forms a continuous cladding. This writing geometry was first demonstrated in [Okh05]. A schematic can be seen in Figure 1.19(c). Since many modification tracks are required in this approach, the resulting waveguide core might be relatively big which can result in a waveguide in the multi-mode regime. Nevertheless, this waveguide geometry probably gives the highest degree of freedom in designing the shape of the waveguide core, a circular cross section just being the most intuitive example. Also, tapered structures can possibly be realized with this approach which can be used to connect two waveguides with different dimensions.

### **Further geometries**

Aside from these three basic writing geometries, there exist many additional variations. In the following, a few examples shall be discussed briefly. Figure 1.20(a) shows a diamond configuration of a depressed cladding waveguide. This geometry may be used to achieve single mode guiding [Mü12]. Figure 1.20(b) displays a number of concentric modification rings which can be used to achieve a higher refractive index contrast at the core [Gro15]. A hexagonal lattice multi-core waveguide was demonstrated to increase the mode area [D'A14, Sak07] and is shown in Figure 1.20(c). In longitudinal writing configuration, a helical sample movement can be applied to achieve a homogeneous and continuous cladding of depressed refractive index [Cau13], displayed in Figure 1.20(d). Based on the photonic crystal fiber (PCF) geometry, guiding in a core surrounded by a periodic array of depressed index modifications was demonstrated [Gro15] and is shown in Figure 1.20(e). Also,

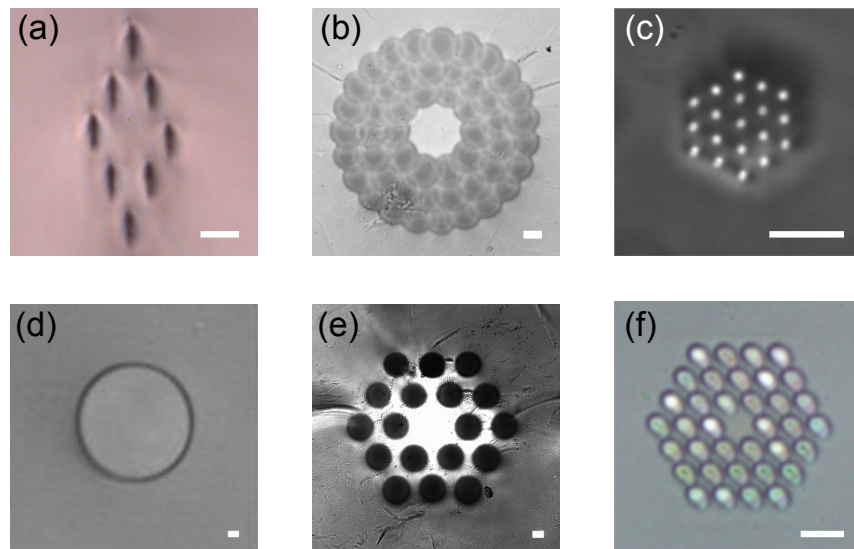


**Figure 1.20:** Some exemplary waveguide geometry variations. All scale bars correspond to  $10\ \mu\text{m}$ . (a) Rhombic depressed cladding structure in  $\text{Pr}:\text{LiYF}_4$  [Mü12], (b) Depressed cladding waveguide in glass built up from concentric rings [Gro15], (c) hexagonal lattice multi-core waveguide in chalcogenide glass [Mas16], (d) cladding waveguide written with a helical sample movement in  $\text{Nd}:\text{YAG}$  [Sal14], (e) White light guiding in a microstructured waveguide in ZBLAN glass using negative index contrast modifications [Gro15], (f) Antiresonant reflecting optical waveguide in borosilicate glass based on positive index modifications [Gro13].

guiding in a solid core surrounded by an array of modifications with increased refractive index proved feasible. The guiding mechanism in this case is based on the anti resonant reflecting optical waveguide (ARROW) model [Gro13]. The waveguide is displayed in Figure 1.20(f).

### Remark

It should be mentioned that in femtosecond laser waveguide writing the Type I and Type II classification – aside from its original meaning to distinguish between working below or above the damage threshold – is sometimes also used to categorize waveguide geometries. Type I then stands for a single-track and Type II for a dual-track waveguide. The scheme is even extended to Type III or Type IV for other geometries [Che14]. To avoid ambiguity, it was suggested to use Type I and Type II solely to specify fabrication regimes of waveguides as originally intended by [Bur06]. The possibilities for writing geometries are far too diverse and complex to be categorized by a simple numeration scheme [Gro15].



### 1.3.6 Functional waveguides in polymers

While ultrafast waveguide writing is widely applied in glasses and crystals, relatively little work has been reported on polymers so far. Additional effects during femtosecond laser irradiation, such as chain scission or crosslinking (see Section 1.2.3), and an overall low damage threshold make waveguide writing in polymers challenging. Those challenges result, amongst others, in high propagation losses in the order of 3–6 dB/cm [Eat12].

In [Zou04], embedded waveguides in PMMA were fabricated by femtosecond laser writing for the first time. An extended-cavity titanium-sapphire laser (Ti:sapphire) at 25 MHz repetition rate was utilized with 30 fs pulse duration and 20 nJ pulse energy at a center wavelength of 800 nm. The beam was loosely focused by a microscope objective with a numerical aperture of 0.25 and the writing speed was set to 20  $\mu\text{m}/\text{s}$ . With difference interference microscopy, a ring-shaped region with an increased refractive index was identified, reproduced in the left side of Figure 1.21(a). The increase in refractive index was attributed to thermal expansion from the core and compressive stress. The near-field intensity distribution of the guided light reveals several propagation modes with different azimuthal symmetries which are shown on the right side of Figure 1.21(a). The maximum index contrast was measured to be  $\Delta n = 2 \cdot 10^{-3}$ .

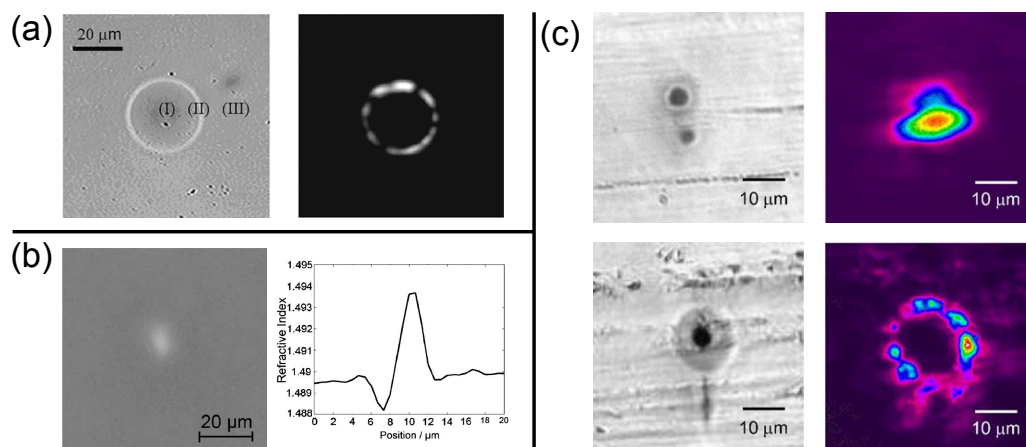


**Figure 1.21:** (a) Difference interference contrast microscope image of a tubular waveguide cross section and corresponding intensity distribution of guided light at 632.8 nm [Zou04]. (b) Microscope image of a waveguide in PMMA written in longitudinal configuration and the corresponding refractive index profile [Bau07]. (c) Microscope images of waveguides fabricated at 100 kHz (top) and 500 kHz (bottom) and the corresponding guided modes at 633 nm [Eat12].

First symmetric waveguides guiding a circular mode were reported in [Sow06, Wat06]. These waveguides were fabricated employing a Ti:sapphire laser system as well. The repetition rate in these cases was 1 kHz, with pulse durations of 85 fs and a writing speed of 0.2 mm/s. Slit beam shaping (see Section 1.3.3) was used to achieve circular symmetry of the waveguides. In these studies, the refractive index change was reported to increase with pulse energy and its maximum was determined to be  $\Delta n = 4.6 \cdot 10^{-4}$ . The measured propagation losses were reported to be 4.2 dB/cm. With a similar setup, symmetric waveguides were demonstrated in poly(ethylene glycol) methacrylate (PEG-MA) with slightly higher propagation losses [DM11]. Light guiding was also observed in structures fabricated in longitudinal writing configuration but these waveguides were not further characterized despite the fact that with  $\Delta n = 4 \cdot 10^{-3}$  they displayed the largest index contrast reported so far, as shown in Figure 1.21(b) [Bau07].

To investigate intermediate repetition rates between 1 kHz and 1 MHz, an Yb:KYW laser system was used in [Eat12]. Optimal guiding structures were obtained at 100 kHz repetition rate, 20 mm/s writing speed and 1.2  $\mu$ J pulse energy. A refocusing effect during writing created two vertically offset zones with depressed refractive index. The guided mode is confined between those two modifications and the propagation losses were measured to be 3 dB/cm. An exemplary microscope image of such a waveguide and the corresponding guided mode in false color representation is reproduced in the top row of Figure 1.21(c). At 500 kHz repetition rate, cumulative effects become more dominant and the modification at the first focus grows in diameter which reduces the refocusing effect, shown in the left image in the bottom row of Figure 1.21(c). In this case, guiding occurs around the modification core.

One advantage of polymers is that they can easily be doped with other components. Disperse Red 13 (DR13) is an azoaromatic chromophore with interesting linear and nonlinear properties which can be applied for electro-optic modulators, second-harmonic generation and birefringent devices [Fer14]. Waveguide writing in PMMA doped with DR13 was demonstrated in [Men08, Fer14]. The resulting waveguides displayed a tubular structure and exhibited propagation losses of 8 dB/cm.

An issue that needs to be considered as well for waveguides written in polymers is their long term stability. The decay or alteration of index modifications in polymers over time was reported on numerous occasions (see Section 1.2.3). This degradation also affects any polymer waveguide system created by femtosecond laser writing. Working in the thermal regime was reported to result in more stable waveguides since zones of refractive index increase based on compressive stress relates on material damage which is less prone to decay [Eat12].

## 1.4 Photonic devices

After a detailed look on the fabrication procedure, geometries and characteristics of femtosecond laser written waveguides, the final section of this chapter will give a brief overview of actual and possible applications in all kinds of target materials. Femtosecond laser written waveguides are ideal for lab-on-a-chip (LOC) applications. A lab-on-a-chip integrates one or several sensory functions on a single small-footprint chip. The necessary waveguide networks are built up of a number of basic and advanced elements which will be addressed in the following.

Two of the most basic elements to direct and distribute light through a network are directional couplers and beam splitters. They have been demonstrated in a multitude of materials, including polymers [Eat06, Wat06, Pos10, Arr14]. For sensing applications, high-Q ring resonators are useful tools since they can detect even the smallest changes in refractive index in their surroundings. They were realized, for example, in chalcogenide glass [Lev15]. Arrayed waveguide gratings (AWGs) are a standard device for multiplexing or demultiplexing, especially in telecommunications applications. A femtosecond laser written A WG prototype was fabricated by [Dou15]. Waveguide-based optical waveplates were demonstrated by tuning the angle of incidence of the writing beam during fabrication [Cor14]. This component was then applied to realize a compact device for the quantum state tomography of two polarization-entangled photons. Another field of applications is waveguide lasers as a compact source for coherent, monochromatic light. The fabrication of femtosecond laser written waveguide lasers in various crystalline materials has been demonstrated on many occasions [DV05, Sie10, Mü12, Cal13].

The feasibility of femtosecond laser written waveguides for lab-on-a-chip applications was also demonstrated on numerous occasions. Waveguides have, for example, successfully been implemented in a commercial fused silica lab-on-a-chip [MV09]. An entire chip fabricated just by femtosecond laser micromachining was demonstrated in [Bra12]. An optofluidic cell sorter was assembled by first creating microfluidic channels via femtosecond laser irradiation and then including optical waveguides in the system utilizing the same laser source. All-waveguide networks are of great interest in fundamental research and for applications alike. A special zigzag array of waveguides in glass allows for the investigation of second order coupling which is otherwise hard to access experimentally [Dre08]. With specially designed two-dimensional evanescently coupled waveguides of Y- and T-junctions, routing and switching light by light was demonstrated [Kei11]. All-optical switching in integrated photonic circuits

will be of great importance in future data processing and telecommunications where the electronic part is the bottleneck in scaling of the network.

All these examples are of course just a small overview of the great variety of work that has been conducted with femtosecond laser written waveguides in all sorts of materials and writing geometries. For further reading, the reader is referred to [DV09], [Ose12], [Eat12], and [Cho14].

# Chapter 2

## Experimental methods

This chapter will introduce all the relevant devices employed in the waveguide writing setup and the applied experimental methods. The fabrication procedure will be described in detail starting with the sample preparation and going all the way to post-processing. Finally, methods to evaluate and characterize the waveguides will be addressed, especially focusing on measuring the occurring losses.

### 2.1 Writing setup

The writing setup consists of a femtosecond laser source, 3D translation stages and all the optics in between to shape the beam properties in the desired way. The setup is displayed in Figure 2.1. The components will be described in detail in the following sections.

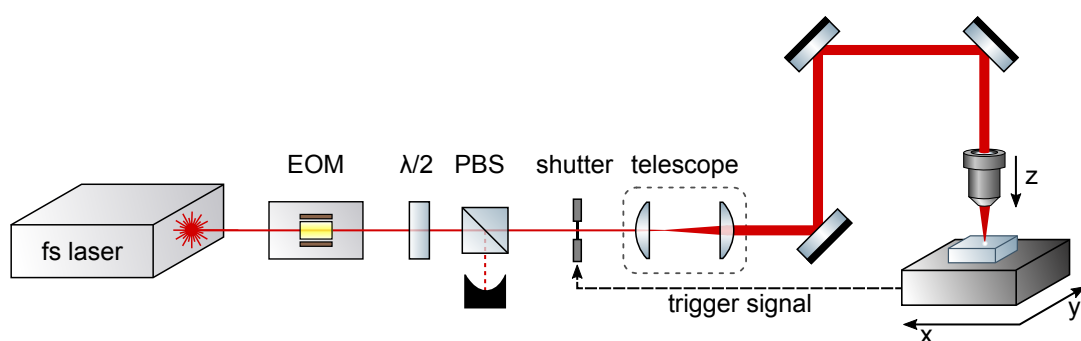


**Figure 2.1:** Schematic diagram of the writing setup. An electro-optic modulator (EOM) picks pulses from the femtosecond laser source to tune the repetition rate. A half-wave plate and polarization beam splitter (PBS) are utilized to control the pulse energy. A mechanical beam shutter clears or blocks the beam path. It gets triggered by the 3D translation stages. The beam diameter is adjusted by a telescope and then focused into the substrate by an aspheric lens or microscope objective.

### 2.1.1 Femtosecond laser source

The employed laser is a chirped-pulse two-crystal Yb:KYW oscillator with cavity dumping [Pal10]. The host material is potassium-yttrium-tungsten (KYW) doped with 5 % ytterbium (Yb). Mode-locking is achieved using a semiconductor saturable absorber mirror (SESAM) by the company BATOP (SAM-1040-2-1ps-4.0-12.7-s-c, #517-la.26). The central frequency lies at 1048 nm with a spectral bandwidth of 8 nm. The internal repetition rate of the oscillator is 17 MHz. A barium borate (BBO) Pockels cell in combination with a thin film polarizer (TFP) couples a portion of every 17<sup>th</sup> pulse out of the system, resulting in an output repetition rate of 1 MHz. Figure 2.2(a) shows an exemplary oscilloscope track of the intra-cavity intensity signal at  $\sim 40\%$  dumping depth. The output pulse energy depends on pump power and dumping depth and can go up to  $7\ \mu\text{J}$  for this system. For micromachining of polymers, however, energies of  $E_p \leq 2\ \mu\text{J}$  proved to be sufficient.

Using a grating compressor, the pulses are externally compressed. The pulse duration is measured by a commercial auto-correlator (APE PulseCheck USB150). With a built-in photomultiplier it is sensitive enough to measure the autocorrelation function using the leakage of a high reflectance mirror. It thereby enables constant monitoring of the pulse duration without interfering with the writing beam. An exemplary spectrum and autocorrelation function are depicted in Figure 2.2(b) and (c), respectively. Note that with increasing cavity dumping the bandwidth decreases. From the full width at half maximum (FWHM)  $\tau_a$  of the autocorrelation function, the pulse duration  $\tau_p$  is calculated by applying the appropriate deconvolution factor. For a Gaussian pulse, for example, the relation is  $\tau_a = \sqrt{2}\tau_p$ . The exact pulse duration could vary based on the day-to-day performance of the oscillator. It was also affected by necessary replacements of laser crystals and the SESAM which always resulted in slightly different specifications. Over the course of this work,

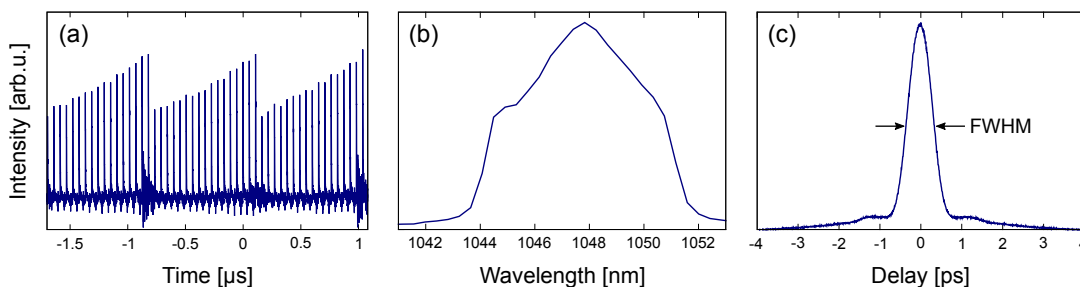


**Figure 2.2:** (a) Exemplary intra-cavity pulse evolution with cavity dumping. (b) Measured spectrum and (c) autocorrelation function of the corresponding pulse.

typical pulse durations were measured to be  $\tau_p = 500 - 600$  fs. This variation, however, did not affect the waveguide writing experiments significantly.

An external Pockels cell based pulse picker (Bergmann PCD9f2) can gradually tune down the output repetition rate of 1 MHz to 1 kHz by picking every  $n^{\text{th}}$ -pulse which gives the freedom to explore different writing regimes. A halfwave-plate in combination with a polarizing beam splitter is used to set the pulse energy to the desired value.

### 2.1.2 3D translation stages

Precise three-dimensional motion is crucial to the fabrication of 3D devices. The accuracy of the translation stages is directly reflected in the quality of the structural modifications in a material. High quality low-loss waveguides demand for the lowest possible oscillations and vibrations of the stages to obtain smooth structures.

The Aerotech ABL1000 air-bearing translation stages, run by linear brushless servomotors, meet these requirements. One key feature of this system is the coordinated movement of three axes in a way that keeps the tangential velocity constant along any continuous three-dimensional path. This is achieved by a computer and a controller unit A3200 which enables the system to automatically control the individual speeds of each axis. The coordinates are set as follows: The x- and y-axis form a horizontal plane which later bears the sample for manufacturing. The vertical z-axis holds the focusing optics and sets the writing depth. Traveling ranges of 10 cm in x- and y-direction, respectively, and 5 cm in z-direction, combined with a maximum scanning speed of 300 mm/s, give a high degree of flexibility. High precision is guaranteed by sub-nanometer resolution and a repeatability of 50 nm. A trigger signal can be set off at any three-dimensional coordinate. It synchronizes the stages with a mechanical beam shutter (Thorlabs SH05) which clears or blocks the optical path to turn the writing process on and off. The user controls the stages via a dedicated software environment. The programming language is Aerobasic which is based on G-code. To execute various parameter scans for different waveguide geometries automatically, specific scripts have been written.

### 2.1.3 Alignment procedure

To ensure reproducibility of the experiments and to achieve the best quality and well-defined material modifications, the laser beam needs to be carefully aligned with respect to the 3D stages and focusing optics. The top-plate of the horizontal stages serves as the reference plane to which the beam is aligned perpendicularly

as a first step. Next, a kinematic mount which will later hold the focusing optic is aligned to be perpendicular to the beam as well. After doing so, the focusing optic is inserted and adjusted in x- and y-direction so that the beam passes directly through the center of the free aperture. After completing these three steps, the initial configuration for each writing process is comparable.

As focusing optics, a set of aspheric lenses (Newport 5720-B) is utilized for waveguide writing. These lenses have an antireflection coating from 625–1050 nm and the manufacturer specifies a transmission of 97%. The specifications of the lenses are given in Table 1.

NA	0.16	0.25	0.5	0.4	0.55	0.65
Magnification	10×	16×	20×	30×	40×	60×
Focal Length [mm]	15.4	11.0	8.0	6.2	4.5	2.8

**Table 1:** Specifications of the utilized aspheric lenses (Newport 5720-B).

## 2.2 Waveguide fabrication

The waveguide fabrication process is divided into three steps: The preparation of a sample, its insertion into the setup and the actual writing process, and finally post-processing to prepare the sample for optical inspection and characterization. The following sections will address each step more closely.

### 2.2.1 Sample preparation

The polymer used for this work is Poly(methyl methacrylate) (PMMA). PMMA (chemical formula  $C_5H_8O_2$ ) is an amorphous thermoplast – a polymer which becomes deformable in a certain temperature range and can be repeatedly molded by heating and cooling of the material. The structural formula of the basic monomer methyl methacrylate (MMA) and the polymer chain can be seen in Figure 2.3(a) and (b), respectively.

PMMA displays high durability and is polishable. It is persistent against unpolar solvents like oils but non-persistent against polar solvents such as Aceton [Kai16]. The glass transition temperature of PMMA is  $T_g \approx 105^\circ\text{C}$ . The temperature for random chain scission is around  $350^\circ\text{C}$  [Fer03]. The linear refractive index of PMMA is typically  $n \approx 1.49$  and its non-linear refractive index is in the order of  $n_2^I \approx 2.7 \cdot 10^{-14} \text{ cm}^2/\text{w}$  [Miw01]. Because of its high light transmittance, PMMA



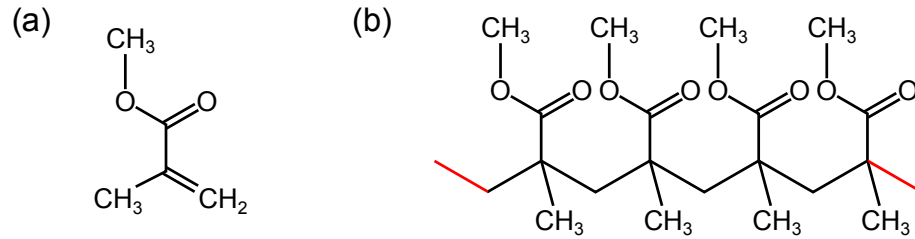


**Figure 2.3:** Structural formulas: (a) Methyl methacrylate monomer, (b) Poly(methyl methacrylate) chain.

is an excellent material for optical applications [Kai16]. It is widely used as core material for communications grade polymer optical fibers (POF).

Mainly two types of commercially available PMMA have been used throughout this work: Clinical grade PMMA (containing minimal residual monomer levels of 0.4 weight percent) “Vistacryl CQ” by the company VistaOptics and “PMMA-03” by the company ChipShop. Initially, the results in both materials were almost identical. However, a second acquired batch of Vistacryl material could not hold up to the performance of the first batch. PMMA-03, on the other hand, continuously delivered reliable results. For this reason, PMMA-03 by ChipShop was chosen as the material to conduct detailed waveguide writing studies.

PMMA-03 comes in dimensions of microscope slides (75.7 mm × 25.6 mm) which are cut to the desired length using a diamond band-saw. Substrates with 1.5 mm and 1 mm thickness are available. PMMA-03 is produced via injection molding which leaves numerous circular marks close to the edges on one side of the material. For reference, this side is always used as top side. The entering facet gets pre-polished to reduce disturbances on the beam upon entering. The intrinsic material attenuation is given by the data sheet of the manufacturer to be in the order of 0.1 dB/cm in the visible spectrum.

## 2.2.2 Writing Process

The sample is fixed in place by a vacuum mount which is attached to a two-axis mirror mount and a rotation mount. To avoid unwanted surface ablation, a low-power laser diode at 630 nm is used during alignment of the sample. The alignment beam is superimposed with the writing laser beam via dichroite before the writing laser is blocked by a mechanical shutter. The focusing lens is then positioned in z-direction so that the focal spot of the alignment laser lies directly on the surface of the substrate. Part of the back reflection is reflected by a 50:50 beam splitter and gets imaged onto a CCD camera. Via triangulation, the sample is then aligned

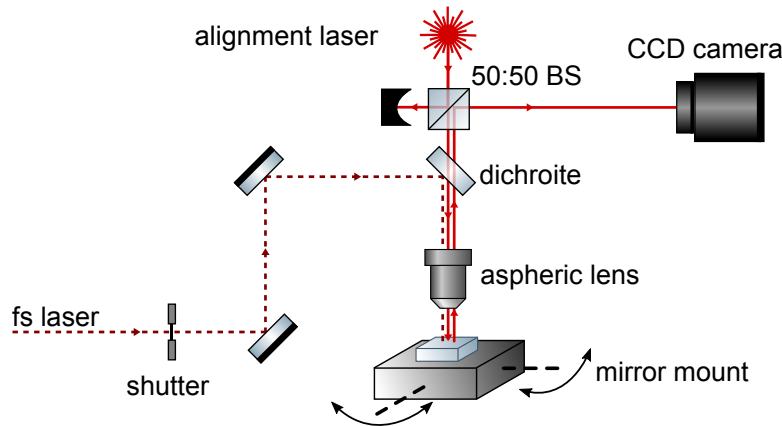


**Figure 2.4:** An alignment laser is coupled into the writing setup via a dichroite and superimposed with the writing beam. A 50:50 beam splitter (BS) sends part of the back reflection from the surface of the substrate onto a CCD camera. Using a mirror mount the sample is aligned perpendicular to the beam via triangulation.

perpendicular to the beam using the mirror mount. This step ensures a constant writing depth later on since the transverse writing configuration (see Section 1.3.2) is applied for the following studies. The optical path and the utilized optics are displayed in Figure 2.4. Finally, one edge of the sample is aligned parallel to the x-axis of the translation stages with the help of the rotation mount.

To create a material modification at a desired writing depth  $d$ , refraction at the air-material-interface (see Section 1.3.1) needs to be compensated for. The effective displacement of the z-axis is calculated to be  $d_{\text{eff}} = d \frac{n_{\text{air}}}{n_{\text{medium}}}$ . Measuring relative distances between modifications at different depths showed that this correction is very precise. The absolute writing depth needs to be calibrated once for every lens since the alignment laser has a different wavelength and divergence than the writing beam and the position of the lenses in the holder varies.

It should be mentioned that the available substrates are not perfectly plane. Especially the edges display a slight upward or downward bend, probably due to manufacturing reasons. These deviations in planarity can affect the absolute writing depth with respect to the surface along the waveguide, therefore, an uncertainty in the order of  $\pm 1 \mu\text{m}$  is assumed. During experimentation however, slightly concave or convex surfaces did not affect the results noticeably.

### 2.2.3 Sample post-processing

The edges of the sample are polished to an optical surface quality. A specially designed sample holder with an edge guide is utilized so that the polished sur-

faces are parallel to one another and perpendicular to the femtosecond laser written structures. An edge is polished in six steps. The first four steps apply different sandpapers with grain sizes gradually decreasing from 26  $\mu\text{m}$  to 5  $\mu\text{m}$  (Presi: P600, P1200, P2400, P4000). In the final two steps, polishing cloths and aluminum oxide suspensions are applied, with grain size 1  $\mu\text{m}$  and 0.3  $\mu\text{m}$ , respectively.

The samples are stored in opaque plastic boxes (GelPak) to ensure protection from environmental influences and degradation from UV light. Also, a desiccator is available to store samples in a low humidity environment.

## 2.3 Waveguide characterization

The different characterization methods that were applied to analyze the waveguides regarding their dimensions and guiding properties are explained in detail in the following sections. A special focus lies on the various losses which can occur in a waveguide and how to experimentally determine them. For reference and statistical evaluation, a number of waveguides with identical writing parameters are created and analyzed.

### 2.3.1 Optical evaluation

The first step in waveguide characterization is the optical evaluation of the morphology and dimensions of the structures. For this purpose, a Zeiss AxioTech Microscope with magnifications ranging from 2.5 $\times$  to 100 $\times$  is employed. A top view gives insight into the quality and homogeneity of a modification. Smooth and continuous tracks are desirable to reduce scattering losses. Deviations in form of periodic or non-periodic disruptions (see Section 1.3.4) become apparent at this stage of assessment. On the basis of the structural modifications, the onset of non-linear photoionization can be identified as well as the threshold for material damage or unstable fabrication regimes.

The cross-sectional profile is evaluated by imaging the polished edges. It gives insight about the symmetry and dimensions of the structure. Possible self-focusing or refocusing effects may also be studied by this analysis step.

### 2.3.2 Characterization Setup

For waveguide analysis, the following characterization setup was assembled: Light is butt-coupled into a waveguide from a cleaved single-mode fiber (Thorlabs SM600). The transmitted light is collected by a microscope objective and is imaged onto a

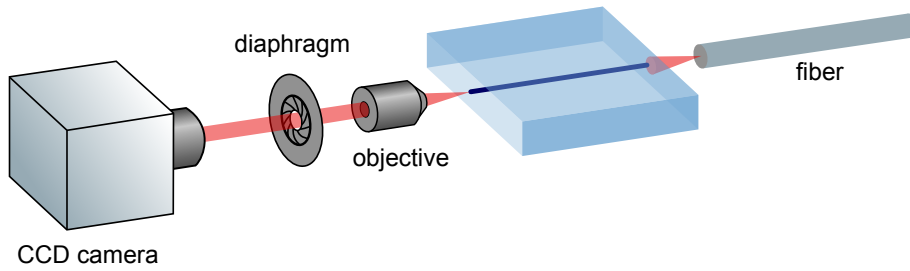


**Figure 2.5:** Schematic diagram of the waveguide characterization setup. Light is coupled from a fiber into a waveguide. At the exiting facet, the transmitted light gets collected by an objective and imaged onto a CCD camera. An iris diaphragm shields from scattered light.

12-bit CCD camera (IDS 3370 CP) to observe the mode profiles. Scattered light which is not part of the guided mode is shielded by an iris diaphragm to the best possible degree. The components are schematically depicted in Figure 2.5. To measure the transmitted power, the camera is simply replaced by a power meter (Coherent FieldMaxII-To).

To precisely align the fiber with respect to a waveguide, all components are placed on micropositioning stages. The fiber and microscope objective are placed on three-dimensional translation stages (Melles Griot 17AMB003/MD) and centered with respect to one another. The sample with the embedded waveguides is placed on a 4-axis-stage (Thorlabs MBT402D/M) with vertical and horizontal translation as well as pitch and yaw. In this way, the sample can always be positioned relative to the fiber to achieve optimal coupling efficiency. The entire setup is placed under a stereo microscope (Zeiss Stemi 2000-C) to help with the alignment procedure and to correctly identify each coupled waveguide. Figure 2.6(a) shows a picture of the

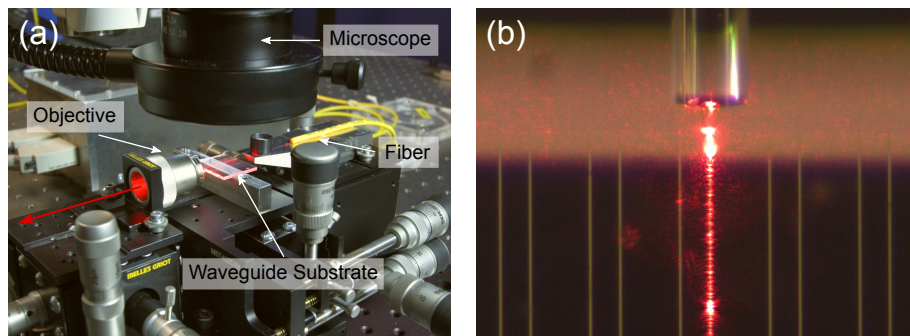


**Figure 2.6:** (a) Photograph of the analysis setup. Visible are the translation stages which hold all components and a part of the stereo microscope which is used for observation. (b) Exemplary microscope image showing a fiber coupling light into a waveguide. Visible scattering losses highlight the coupled waveguide.

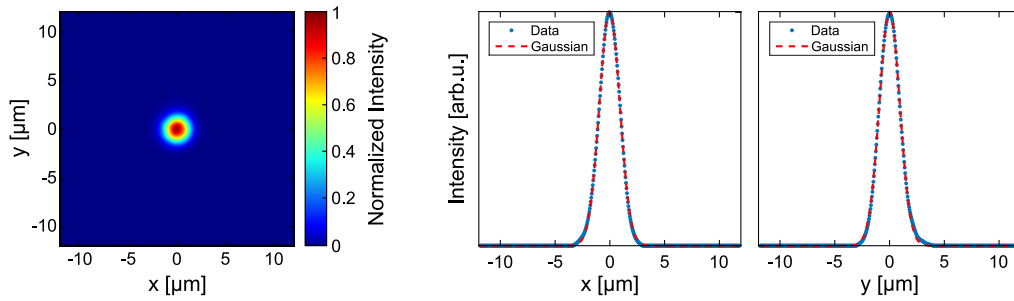


**Figure 2.7:** Left: False color representation of an intensity distribution of a Thorlabs SM600 fiber at 638 nm. Right: Horizontal and vertical cut of the same profile. Red line shows the fit of a Gaussian distribution. The mode field radius is calculated to be  $1.85 \mu\text{m}$  on both axis.

analysis setup and Figure 2.6(b) shows a microscope image of the fiber coupling into a waveguide. A temperature stabilized 4-channel fiber-coupled laser source allows for analysis of the waveguides at four different wavelengths: 406 nm, 520 nm, 638 nm, and 850 nm. Additionally, a fiber coupled laser source at 660 nm is available.

The images of the guided modes taken by the CCD camera are automatically post-processed by a Matlab script. First the data gets normalized and then a region of interest (ROI) centered around the guided mode is converted into a false color representation of the intensity distribution. Scaling is done according to a reference measurement. As an example, the fundamental mode of the utilized fiber is shown in Figure 2.7, as well as a cut in horizontal and vertical direction. A Gaussian distribution was fitted to the data and is shown as a red dotted line. It shows how well the  $\text{LP}_{01}$  mode can be approximated with a Gaussian distribution. The mode field radius is defined as the radius where the peak intensity has dropped to  $1/e^2$ . The mode field diameter is then twice the mode field radius and is measured to be  $3.7 \mu\text{m}$  at 638 nm for the present fiber.

A small rearrangement of the setup also allows for coupling of a free propagating beam. For this purpose, an aspheric lens replaces the fiber on the translation stage to focus a collimated beam into the waveguide. The 0.16-NA lens is used in this case to match the numerical aperture of the waveguide in the best possible way. This approach allows for manipulation of the polarization of the coupled light with the help of a halfwave-plate. It also becomes feasible to couple the femtosecond laser pulses from the writing laser into the waveguides to study non-linear effects during propagation such as self-phase modulation.

### 2.3.3 Numerical aperture measurement

To measure the numerical aperture (NA) of a waveguide, a method proposed in [Hom99] is adopted. It is based on interference between unguided light from the fiber and light exiting the waveguide which results in a pattern of concentric rings. Measuring the radius at which the fringes decay at different positions in the far field allows for calculating the acceptance angle of the waveguide and therefore the numerical aperture. A schematic is shown in Figure 2.8(a). The light in the far field is collected by a CCD camera, an exemplary image is shown in Figure 2.8(b). The concentric rings are not completely visible because part of the material modification becomes opaque and blocks part of the light. The original publication estimates the error of this method to be around 30 %.

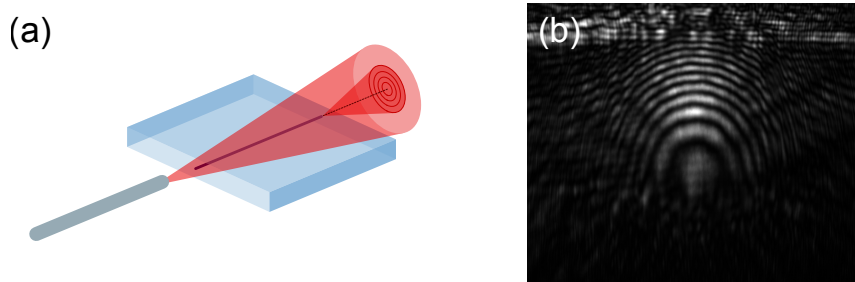


**Figure 2.8:** (a) Schematic of the NA measurement method. Interference between guided and unguided light allows for the calculation of the acceptance angle of a waveguide. (b) Typical CCD image of the interference fringes.

From Equation (1.4), the relation  $NA \approx \sqrt{2n\Delta n}$  is known which holds for small  $\Delta n$ . The NA measurement can therefore also be used for an estimation of the refractive index contrast of a waveguide.

### 2.3.4 Waveguide losses

In accordance with the usual nomenclature in fiber optics and to make diagrams more intuitive, the losses will be given as positive values throughout this work. The unit of choice is decibel (dB).

A fundamental parameter to characterize the quality of a fabricated waveguide is given by the insertion losses which are induced by the device as a whole. They are easy to measure: First, the input power  $P_{in}$  is determined by collecting all the light exiting the fiber with a high-NA objective and send the collimated beam onto a powermeter. Then the waveguide gets inserted and the transmitted power  $P_{out}$  is measured. It is important to optimize the coupling efficiency by carefully translating

and tilting the sample with respect to the fiber. Now the only difference between  $P_{\text{in}}$  and  $P_{\text{out}}$  is the absence or presence of the inserted waveguide. Therefore, the insertion losses in decibel are given by

$$\text{IL} = -10 \cdot \log \left( \frac{P_{\text{out}}}{P_{\text{in}}} \right). \quad (2.1)$$

The insertion losses are composed of all the terms causing losses in a device. In the following, these different contributions will be discussed.

### Coupling losses

Typically, the waveguide and fiber modes differ from one another regarding shape and size. This mode mismatch results in a certain loss when transferring light from one mode to the other. Light which does not couple into the waveguide is scattered away, these are the coupling losses. The theoretical coupling efficiency  $\eta$  is calculated from the overlap integral

$$\eta = \frac{|\int E_1(x, y) E_2^*(x, y) dx dy|^2}{\int |E_1(x, y)|^2 dx dy \cdot \int |E_2(x, y)|^2 dx dy}, \quad (2.2)$$

with  $E_1$  and  $E_2$  the electric field of the waveguide and fiber respectively. Since  $E \propto \sqrt{I}$ , the electric field (without phase information) can be directly obtained from the acquired intensity distributions recorded by the CCD camera. At this point, it is important that the magnification stays the same, meaning the distances between sample and microscope objective, and microscope objective and camera must be kept constant (see Figure 2.5). The coupling efficiency  $\eta$  may be calculated directly from the discrete values. The coupling losses in decibel are then typically displayed as

$$\text{CL} = -10 \cdot \log(\eta). \quad (2.3)$$

If no experimental fiber mode is available, one can calculate the deviation of the waveguide mode from a perfect Gaussian distribution with appropriate dimensions. Assuming that light is coupled from a single-mode fiber, this approach gives an estimate of the best possible coupling efficiency between the waveguide and a fiber. In doing so, the estimated coupling losses are as low as possible, thus preventing the underestimation of other loss terms.

### Fresnel losses

Another loss term arises from reflection at the air-sample interface due to a discontinuity in the refractive index distribution. These Fresnel losses – assuming perpendicular irradiation – are calculated according to

$$\text{FL} = -10 \cdot \log \left[ 1 - \left( \frac{n - n_0}{n + n_0} \right)^2 \right]. \quad (2.4)$$

The refractive index of the substrate and air are  $n$  and  $n_0$ , respectively. A typical refractive index value for PMMA of  $n = 1.49$  results in Fresnel losses of  $\text{FL} \approx 0.17$  dB. Fresnel losses can be avoided by using an index matching liquid between the substrate edge and the fiber.

### Propagation losses

One of the defining characteristics of a waveguide is the attenuation of light during propagation. These propagation losses (PL) are the remaining contribution to the insertion losses of a straight waveguide. To some degree, the losses are caused by absorption. But the main cause for propagation losses in femtosecond laser written waveguides is Rayleigh-scattering due to inhomogeneities along the waveguide path, structure roughness, small defects and micro-bendings [Hun09]. Propagation losses directly depend on the length  $l$  of a waveguide and are therefore given in decibel per unit length.

Summing up all discussed terms and taking into account that Fresnel losses occur at two surfaces gives the following composition of the insertion losses:

$$\text{IL} = \text{CL} + 2 \cdot \text{FL} + l \cdot \text{PL}. \quad (2.5)$$

Assuming that all other loss terms are well known, the propagation losses may now be calculated by rearranging the formula to:

$$\text{PL} = \frac{\text{IL} - 2 \cdot \text{FL} - \text{CL}}{l}. \quad (2.6)$$

The error of this calculation is the sum of all the errors of the contributing terms.

Another way of directly obtaining the propagation losses is the “cutback technique”. In this case, the transmitted power  $P_1$  of a waveguide is measured for its initial length. Then the sample gets cut back by  $\Delta l$  and the transmitted power  $P_2$



is measured. Assuming that all other loss sources stay constant, the propagation losses can be calculated as

$$\text{PL} = -10 \cdot \frac{1}{\Delta l} \cdot \log \frac{P_1}{P_2}. \quad (2.7)$$

In the course of the presented work, this technique proved unsuitable to characterize femtosecond laser written waveguides in polymers. The problem is that cutting and repeated polishing affects the substrate in a way that all other loss sources may not be assumed constant anymore. As an alternative, the following method was developed: Multiple samples at different lengths are fabricated, each containing numerous waveguides written with identical writing parameters. The measured insertion losses are averaged for identical waveguides. As a function of  $l$ , these insertion losses allow for the calculation of the propagation losses as the slope of a linear fit, in accordance with Equation (2.5). Variations in coupling efficiency are to be expected but average out when considering a larger set of waveguides. The y-intercept gives additional information about Fresnel and coupling losses. This method has the advantage of being non-destructive compared to the cutback technique and it gives additional insight about the reliability and reproducibility of the fabrication procedure. However, it requires more time and effort since multiple samples with a large number of waveguides need to be fabricated and characterized.

### Bend losses

When a curved waveguide is analyzed, additional losses need to be taken into account. The physical origins of bend losses in a waveguide have been discussed in Section 1.1.3. Here, the experimental evaluation of the bend losses will be described.

Pure bend losses (BL) in decibel per unit length strongly depend on the radius of curvature  $R$ . Also, transition losses through mode-mismatch between a straight and a curved segment can occur and are directly related to  $R$  as well. This adds two additional terms to the insertion losses

$$\text{IL} = \text{CL} + 2 \cdot \text{FL} + \text{PL} \cdot l + \text{BL}(R) \cdot b(\delta, R) + \text{TL}(R). \quad (2.8)$$

The angle  $\delta$  which is covered by a curve of radius  $R$  defines the length of the bent segment which is given by  $b(\delta, R) = \pi R \delta / 180^\circ$ .

To determine the pure bend losses experimentally, waveguides with an s-curve segment are fabricated. This geometry has the advantage that entrance and exit facet are parallel to one another and the waveguide is perpendicular to these surfaces

which allows for characterization with the present setup. An s-curved waveguide is also the basic building block for more complex waveguide networks. Waveguides with curves at constant  $R$  but varying  $\delta$  are fabricated, resulting in varying curve lengths  $b$ . Almost all other loss terms are constant. The total length  $l$  of a waveguide composed of straight and bent segments is in principle a function of  $\delta$  and  $R$  as well. However, if the propagation losses are very small compared to the bend losses and  $l \gg b$ , the propagation loss term  $PL \cdot l$  may be assumed constant for small changes in curve length. Therefore, IL becomes a linear function of  $b$ . The pure bend losses can now be calculated from the slope of a linear fit. If the properties of straight waveguides are well known, the transition losses can be determined from the y-intercept.

# Chapter 3

## Results

The previous Chapter 2 introduced all experimental techniques required for femto-second laser waveguide writing. Different writing configurations and waveguide geometries were discussed in detail in Section 1.3. This chapter will now present the main results of this thesis which enable the fabrication of single-mode waveguides with a large refractive index contrast core and low propagation losses.

The chapter covers two main experimental topics: Firstly, the interaction of femto-second laser radiation with polymer substrates and the formation of a continuous modification track are studied. The resulting material modifications are evaluated by optical microscopy regarding shape and dimension, with respect to irradiation and writing properties. The writing parameters most suitable for waveguide fabrication are determined. Secondly, the refractive index modifications are tested regarding their optical guiding capabilities and various writing geometries are thoroughly studied and characterized. The main focus lies on single-track, dual-track and multi-track waveguides (see Section 1.3.5).

Throughout the experimental work, the central wavelength of the writing laser beam is 1048 nm and the pulse duration is between 500 fs and 600 fs. All studied waveguides were written in transverse writing configuration (see Section 1.3.2).

### 3.1 Structure of a modification track

As described in Chapter 1, many experimental parameters can influence femtosecond laser waveguide writing but there are three key parameters: The pulse energy  $E_p$ , the repetition rate  $f_{\text{rep}}$  and the writing speed  $v$  (see Section 1.3.1). The pulse energy has to be large enough to trigger nonlinear photoionization but small enough to avoid substantial damage in the material. The repetition rate and writing speed define temporal and spatial separation of consecutive pulses, respectively.

In the following sections, the interplay of these three parameters and the emerging structural changes in PMMA are investigated. The goal is to reveal the most adequate experimental parameters which enable material modifications suitable for waveguiding.

### 3.1.1 Single-pulse modification

To study the modification process, only a single laser pulse is allowed to interact with a volume of the substrate. To achieve this situation experimentally, low repetition rates and high translation speeds of the sample are utilized. For instance, at  $f_{\text{rep}} = 1 \text{ kHz}$  and  $v = 100 \text{ mm/s}$ , the sample moves  $100 \mu\text{m}$  between two consecutive pulses, thereby separating the modification spots. Experimentally it was found that a distance of  $10 \mu\text{m}$  is already large enough for an observation of modifications free of interaction with any adjacent structural changes. During the duration of a  $600 \text{ fs}$  pulse, the sample only moves a distance in the order of a proton diameter which is negligible.

In the experiment the laser beam is focused  $150 \mu\text{m}$  below the surface by a  $0.55\text{-NA}$  aspheric lens and the sample is scanned with a speed of  $20 \text{ mm/s}$  at a repetition rate of  $1 \text{ kHz}$ . As a first step, the threshold energy for the onset of nonlinear photoionization is determined. For pulses with a duration of  $600 \text{ fs}$ , it was found at

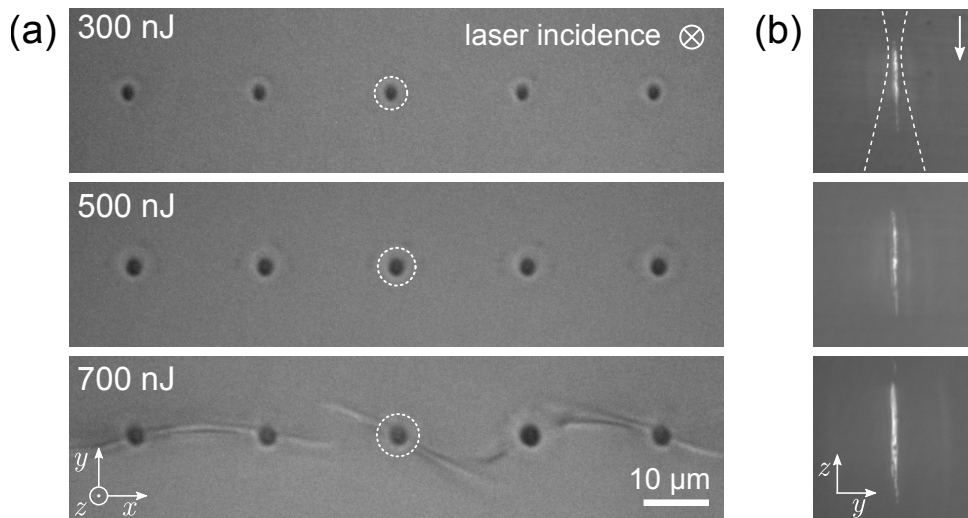


**Figure 3.1:** (a) Top view of single-pulse modifications, separated by a distance of  $20 \mu\text{m}$ , for pulse energies of  $300$ ,  $500$  and  $700 \text{ nJ}$ . The laser incidence was into the plane. The white dotted circles mark the outside margins of the visible structural changes. (b) Corresponding cross-sectional morphology of a single-pulse modification. Laser incidence was from the top. The white dashed line marks the waist evolution of the focused Gaussian beam. The scaling is identical for all images.

100 nJ. Below this energy, no visible alterations to the material can be observed with light microscopy. Next, the influence of increasing pulse energies is investigated. Figure 3.1(a) shows top view microscope images of single-pulse modifications at 300 nJ, 500 nJ and 700 nJ, respectively, with separations of 20  $\mu\text{m}$  between each spot. Due to the spatial and temporal separation of consecutive pulses, heat accumulation effects are negligible in this configuration. One can see that each spot is composed of a dark center with a diameter of about 2–3  $\mu\text{m}$  depending on the pulse energy. This diameter matches the spot size of the focused laser beam which was calculated to be 2  $\mu\text{m}$  using a beam propagation software (vWaistWatcher). A faint outer ring of material modification is also visible. The diameter of this outer ring grows with increasing pulse energy, the outside margins are marked by white dotted circles in Figure 3.1(a). This second zone of material modification can be attributed to thermal effects caused by heat diffusion from the focal spot.

At 700 nJ pulse energy, tension cracks emerge from the modification spots and extend some tenths of micrometers into the substrate. These cracks are a clear sign that the core of the structure applies a considerable amount of stress onto its surroundings which is the result of a quickly expanding plasma core after non-linear photoionization in the irradiated zone. Cracks in a material, however, are a source of scattering losses which are undesirable for waveguide applications. Therefore, going beyond a pulse energy of 700 nJ is expected to be unfavorable for waveguide writing in polymers.

The cross-sectional appearance of the modification spots at 300 nJ, 500 nJ and 700 nJ are shown in Figure 3.1(b). The microscope images were taken through the polished edges of the sample. Elongated structures are visible and grow in vertical dimension with increasing pulse energy. For example, at 300 nJ the length is 14.5  $\mu\text{m}$  while at 700 nJ it extends to 20.5  $\mu\text{m}$ . Measuring a distance of 150  $\mu\text{m}$  from the surface of the substrate puts the expected position of the focal spot 1.5  $\mu\text{m}$  below the tip of the structure. An overlay in the top image of Figure 3.1(b) shows the waist evolution of the focused laser beam as a white dashed line. Taking systematic errors and self-focusing effects into account, an uncertainty of  $\pm 2 \mu\text{m}$  is estimated. Nevertheless, one can already conclude that the structure evolves from top to bottom.

Even at 100 nJ, the peak power of the laser beam is – at approximately 150 kW – more than three times as large as the critical power  $P_{\text{crit}}$  for a collapse of the beam. Surpassing  $P_{\text{crit}}$  in femtosecond laser waveguide writing is known to cause filament propagation whenever self-focusing is dynamically balanced by de-focusing effects of the free electron gas induced by nonlinear photoionization (see Section 1.3.1). Filamentation was reported to result in elongated material modifications in axial

direction in PMMA [Wat09, Upp08]. Repeating the experiment with 0.40-NA and 0.65-NA aspheric lenses leads to modifications with almost exactly the same dimensions. Filamentation can therefore explain the elongated appearance of the structure in axial direction as this process does not depend on the intensity distribution in the focal spot.

Additionally, material damage as a result of optical breakdown is known to occur above the critical power [Sch01]. The center may therefore be an area of carbonized material or even a cavity [Zhe15a]. Damage of this kind would explain the black appearance of the center in the top view of the sample in Figure 3.1. The varying brightness in any cross-sectional view is caused by scattering and deflection of the illuminating light at an uneven interface between the modification core and the surrounding material.

The analysis of simple single-pulse modifications has already given insight into the structural changes occurring in the material. Damage zones have been identified, as well as zones affected by thermal effects. It has also become clear that these modifications cause stress to the material which can extend far beyond the directly irradiated volume.

### 3.1.2 Heat accumulation

As a next step, the temporal spacing between consecutive pulses is investigated. It is determined by the repetition rate of the laser system and defines the heat accumulation (thermal) and single-pulse (athermal) regime (see Section 1.3.1). Since the thermal diffusivity of polymers is very small compared to other materials, such as glass, heat accumulation needs to be carefully balanced for waveguide writing.

#### Experimental investigation

To investigate heat accumulation experimentally, substrates are exposed to stationary irradiation of a varying number of pulses. The smallest number of pulses is limited by the shortest opening time of the shutter which is set to 20 ms for the following experiments. Figure 3.2 shows microscope images of spots exposed to  $2 \cdot 10^3$ ,  $2 \cdot 10^4$  and  $2 \cdot 10^5$  pulses, respectively, at repetition rates of 1 kHz, 10 kHz, 50 kHz and 100 kHz. The pulse energy is set to 200 nJ.

For  $2 \cdot 10^3$  pulses, the irradiated spots look almost identical with a diameter of  $5 \mu\text{m}$  for 1 kHz and 10 kHz, and a slightly larger diameter of  $7 \mu\text{m}$  for 50 kHz and 100 kHz. Visible in all four cases are tension cracks in the material emerging from the center.

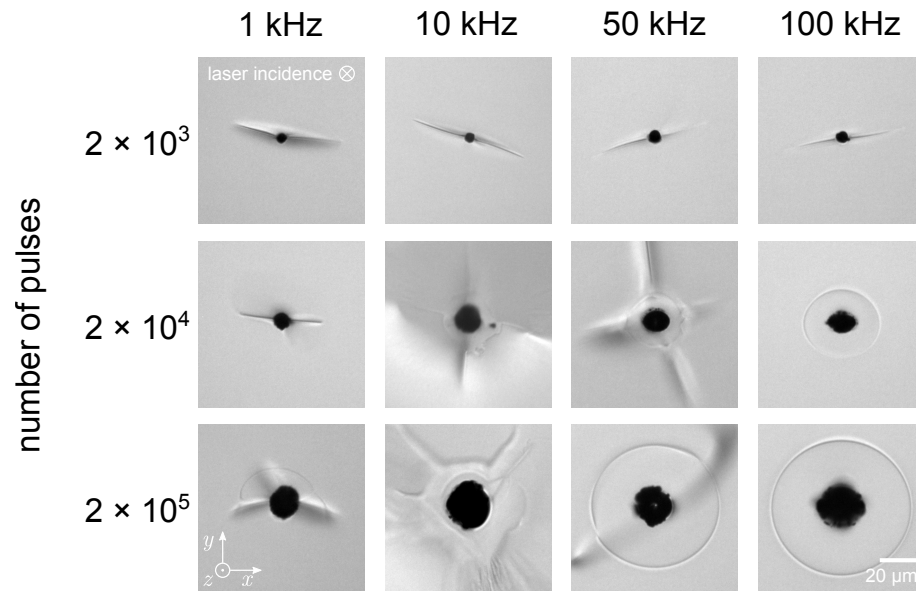


**Figure 3.2:** Light microscopy image of zones exposed to stationary irradiation of laser pulses with an energy of 200 nJ. The number of pulses per spot was  $2 \cdot 10^3$ ,  $2 \cdot 10^4$  and  $2 \cdot 10^5$  at repetition rates of 1, 10, 50 and 100 kHz. The laser incidence was into the plane.

With  $2 \cdot 10^4$  pulses per spot, deviations at different repetition rates become apparent. At 1 kHz, modifications do not show any signs of accumulated thermal effects. Only the dark core region grows slightly due to increased net-energy input. At 10 kHz, the onset of heat accumulation becomes apparent. An area of molten and resolidified material becomes visible around the center, accompanied by even larger cracks as a result of stress due to high temperature gradients. The heat affected zone looks very irregular which indicates that the heating process is still largely affected by thermal cycling – the process of repeated alternations between two temperature extremes at a high rate. The corresponding 50 kHz spot looks very similar, only featuring a slightly larger zone affected by thermal diffusion which is to be expected due to increased heat accumulation. A repetition rate of 100 kHz, on the other hand, is clearly identified as the thermal regime. Initial tension cracks get melted away by a growing thermally affected zone. Strong heat accumulation reduces thermal cycling which in turn prevents the formation of new cracks. The result is a sphere of molten and resolidified material with a diameter of 39  $\mu\text{m}$  and a dark center.

Increasing the number of pulses to  $2 \cdot 10^5$  continues the trend. A repetition rate of 1 kHz still shows no signs of heat accumulation effects and at 10 kHz, the onset of heat accumulation is still very irregular. At 50 kHz, however, heating of the material becomes continuous and results in a homogeneous thermally affected zone except for a single crack. The modification at 100 kHz simply grows in size.

It was reported that a cavity can form in polymers under stationary femtosecond laser irradiation when the temperature at the core exceeds the temperature for random chain scission [Zhe15a] (see Section 1.2.3). In this context, the black appearance of the centers under light microscopy is explained by total internal reflection of the illuminating light at the polymer-cavity-interface. At higher repetition rates, the stronger laser flux creates additional micro-bubbles in the molten zone which can assemble around the core. In Figure 3.2 these bubbles are responsible for the blurring of the interface between the core and the molten region since naturally not all bubbles are in focus.

### Simulation of the heat-diffusion equation

To study the dynamics of the heating process, basic heat accumulation simulations are conducted. It is especially of interest to see when the local temperature in the material surpasses the glass transition temperature  $T_g$  as well as the temperature for random chain scission  $T_{cs}$ . For simplicity, radial symmetry is assumed and therefore the governing one-dimensional heat-diffusion equation is given by

$$\frac{\partial}{\partial r} \left( r^2 \frac{\partial T}{\partial r} \right) = \frac{r^2}{\alpha} \frac{\partial T}{\partial t}, \quad (3.1)$$

with  $T(r, t)$  the temperature of the material as a function of space  $r$  and time  $t$ , and  $\alpha$  the thermal diffusivity of a given material. The equation is discretized by applying the finite difference method Forward-Time-Centered-Space (FTCS) [Ple12]. Discretization can be found in Appendix A.

Further assumptions are based on an approach proposed in [Eat05]. The energy volume density of the heat source is considered to be of a spherical Gaussian distribution

$$E(r) = E_0 \exp \left( -\frac{r^2}{w_0^2} \right), \quad (3.2)$$

with  $w_0 = 1 \mu\text{m}$  the waist at the focal spot of a laser beam focused by a 0.55-NA lens. The normalization constant  $E_0$  is calculated by setting the pulse energy  $E_p$  equal to the volume integral over  $E(r)$  which yields

$$E_p = 4\pi E_0 \int_0^\infty r^2 \exp \left( -\frac{r^2}{w_0^2} \right) dr \quad \Rightarrow \quad E_0 = \frac{E_p}{(\sqrt{\pi} w_0)^3}. \quad (3.3)$$



Whenever a new laser pulse arrives, the temperature profile is increased by an instantaneous temperature change of

$$\Delta T(r) = \frac{E(r)}{\rho c_p}, \quad (3.4)$$

with  $\rho = 1.19 \cdot 10^3 \text{ kg/m}^3$  the density of PMMA and  $c_p = 1.47 \cdot 10^3 \text{ J/(kg K)}$  its specific heat capacity. With the thermal conductivity  $\kappa = 0.19 \text{ W/mK}$  [Ass05], the thermal diffusivity of PMMA is calculated to be

$$\alpha = \frac{\kappa}{\rho c_p} \approx 0.11 \cdot 10^{-6} \text{ m}^2/\text{s}. \quad (3.5)$$

Not the entire energy of a laser pulse is absorbed by the medium in a nonlinear photoionization processes. In accordance with [Eat05], the energy absorption is assumed to be 50 %.

A pulse train of 12 pulses is simulated to illustrate the trend of the heat accumulation. The ambient temperature is set to  $T_0 = 20 \text{ }^\circ\text{C} = 293 \text{ K}$ . Figure 3.3(a) shows the results of the temperature evolution  $3 \mu\text{m}$  from the center for a pulse energy of 200 nJ at four repetition rates: 1 kHz, 10 kHz, 50 kHz and 100 kHz. The red dashed line marks the glass transition temperature at  $T_g = 99 \text{ }^\circ\text{C} = 372 \text{ K}$  and the black dashed line marks the temperature for random chain scission  $T_{cs} = 350 \text{ }^\circ\text{C} = 623 \text{ K}$ .

It can be seen, that even the input energy of a single 200 nJ laser pulse results in a temperature peak above  $T_{cs}$ , a condition which can result in the formation of a cavity in the material. Also, repetition rates of 50 kHz and 100 kHz are clearly in

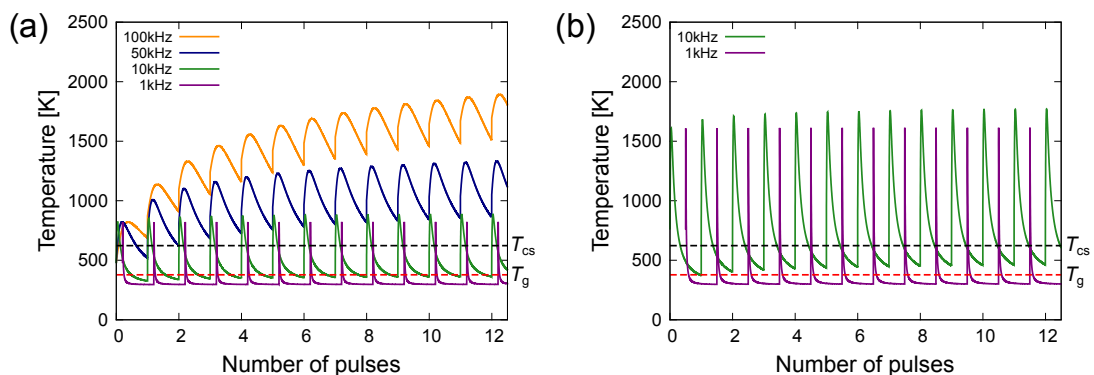


**Figure 3.3:** Evolution of the material temperature  $3 \mu\text{m}$  from the center of the focus over the course of 12 consecutive pulses. (a) 200 nJ pulse energy at 1 kHz, 10 kHz, 50 kHz and 100 kHz. (b) 500 nJ pulse energy at 1 kHz and 10 kHz. The dashed red line marks the glass transition temperature of PMMA at  $T_g = 372 \text{ K}$  whereas the black dashed line marks the temperature for random chain scission at  $T_{cs} = 623 \text{ K}$ . The data for 1 kHz set has a small offset on the horizontal axis to increase its visibility.

the heat accumulation regime since the average temperature constantly rises with an increasing number of pulses. Slight heat accumulation is also visible at 10 kHz, but the temperature always descends below the glass transition temperature. However, the trend shows that the accumulated temperature will ultimately pass  $T_g$  which is consistent with the experimental observation that thousands of pulses lead to a zone affected by melting (see Figure 3.2).

Looking at the transition from the athermal to the thermal regime in more detail, Figure 3.3(b) shows simulation data for pulse energies of 500 nJ for 1 kHz and 10 kHz repetition rate. At 1 kHz, the medium still completely returns to ambient temperature after each pulse. At 10 kHz, on the other hand, the temperature quickly moves past the glass transition temperature and the molten zone can expand further into the material. The accumulated heat still remains below the chain scission temperature, however. Considering that random chain scission may lead to cavity formation (see Section 1.2.3), it can be regarded as the more important temperature threshold. When the temperature close to the focal volume constantly stays above  $T_{cs}$ , it may have a significant influence on the waveguide writing process.

In summary, experiments and simulations have both confirmed that a repetition rate of 1 kHz leads to material modifications in the athermal regime. For waveguide writing in the heat accumulation regime, a repetition rate of 100 kHz appears to be the proper choice. Here, reduced thermal cycling prevents the formation of tension cracks. In a dynamic process like waveguide writing, where the sample is scanned through the laser focus, consecutive pulses never fully overlap and the number of pulses affecting a volume in the substrate strongly depends on the translation speed. Therefore, the threshold for fabrication in the athermal regime may be at a higher repetition rate than for stationary exposure.

### 3.1.3 Evolution of the track morphology

To create a structure suitable for waveguiding a continuous modification track has to be written. That means, the modifications of each pulse have to spatially overlap in the substrate. This superposition leads to an entirely different dynamic for the modification process. To study the merger of individual spots into a continuous track, the distance between consecutive pulses was stepwise reduced from 10  $\mu\text{m}$  to 0.5  $\mu\text{m}$  by adjusting the writing speed. To rule out heat accumulation effects, the experiment was first conducted at 1 kHz with a small pulse energy of 200 nJ. The beam was focused 150  $\mu\text{m}$  below the surface by a 0.55-NA aspheric lens. Figure 3.4 shows the resulting structures in top view and cross-sectional view microscope images.

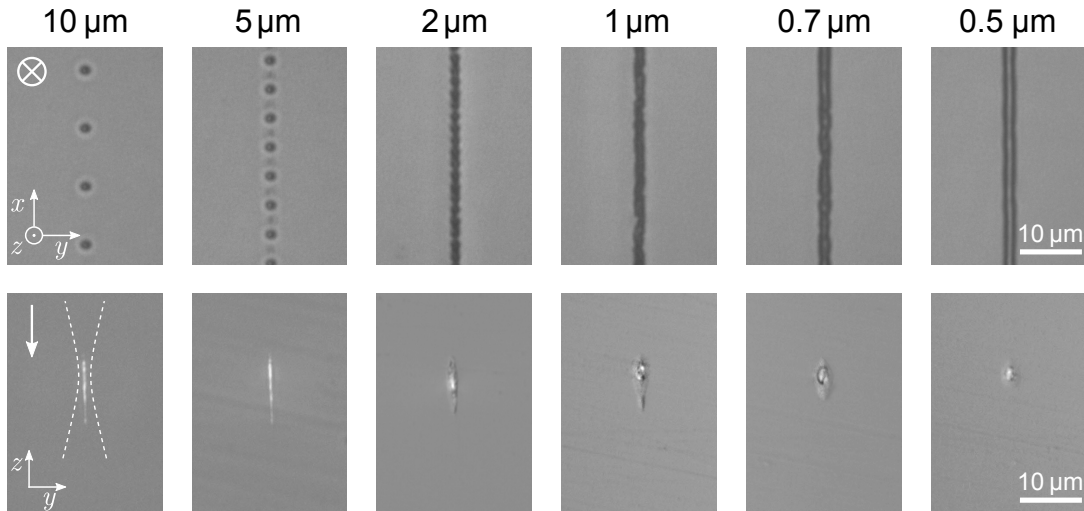


**Figure 3.4:** Top row: Top view of modification tracks with spacings from  $10\ \mu\text{m}$  to  $0.5\ \mu\text{m}$  between consecutive pulses, written at  $200\ \text{nJ}$ . Laser incidence was into the plane. Bottom row: corresponding cross-sectional morphology of the material modification.

Although the modifications do not yet physically overlap at a distance of  $5\ \mu\text{m}$ , small tension cracks already begin to form between them. However, the cross-sectional appearance is not affected yet and the elongated shape due to filamentation is still preserved. When the black cores begin to overlap at a spacing of  $2\ \mu\text{m}$ , a “pearl chain”-like structure emerges at the core of the track. In cross section, the modification begins to grow in width and to shrink in length, forming a more droplet-like appearance. With the onset of spatial overlap the beam is distorted by the existing material modification and self-focusing, which strongly depends on the intensity, is affected as well. Decreasing the spacing further merges the spots more and more together. The edges become smoother and the cross section takes a more ellipsoid shape. At a spot spacing of  $0.5\ \mu\text{m}$ , the structure becomes a smooth and continuous modification track. In cross section, it now displays circular symmetry. Reducing the distance below  $0.5\ \mu\text{m}$  did not have any additional effects on the morphology of the structural changes when observed under light microscopy.

The center of the circular structure was measured to originate directly at the preset writing depth of  $150\ \mu\text{m}$  and the core diameter matches the spot size of the focused laser beam. Around the core extends a faint ring of modified material with a diameter of  $3\ \mu\text{m}$ , similar to the heat affected zone visible for single-pulse modifications (see Section 3.1.1). The diameter of the entire structure slightly grows when the pulse energy is increased. The fact that the cross-sectional appearance of a continuous modification track displays spherical symmetry shows that the intensity

distribution of the focused writing beam has only little influence on the morphology. This observation is further supported by repetition of this experiment with a 0.40-NA and a 0.65-NA aspheric lens which results in the same morphology, except for some variation in the diameter.

It should be noted that the morphology of the track core only depends on the spatial separation of the pulses. In other words, it makes no difference if the experimental parameters are 1 kHz and 0.5 mm/s, 10 kHz and 5 mm/s or 100 kHz and 50 mm/s. This means that even though thermal diffusion from the center plays a role in the formation of the circular symmetry, heat accumulation does not.

To expose and study the internal structure of the modifications further, focused ion beam (FIB) milling was applied. A high energy ion beam removes material by sputtering and thereby allows precise milling of a surface. Imaging is achieved by a scanning electron microscope (SEM). For this purpose, a special sample is fabricated with structures in very close proximity to the surface. The substrate is then coated with a few nanometers of gold so surface electrons may discharge and artifacts in the image are reduced. A tilt of the imaging stage by  $54^\circ$  is digitally corrected. Consequently, the scaling in x- and y-direction is identical. A platinum bar is deposited over the embedded structure to achieve a cross-sectional cut perpendicular to the surface. This platinum bar can be seen in Figure 3.5(a). It emphasizes the surface bulge created by the material modification which confirms that great pressure arises from the core and pushes the material outwards. With focused ion beam milling, material gets removed and a wedge to a depth of 10  $\mu\text{m}$  is machined into the surface which allows a cross-sectional view into the embedded structure.

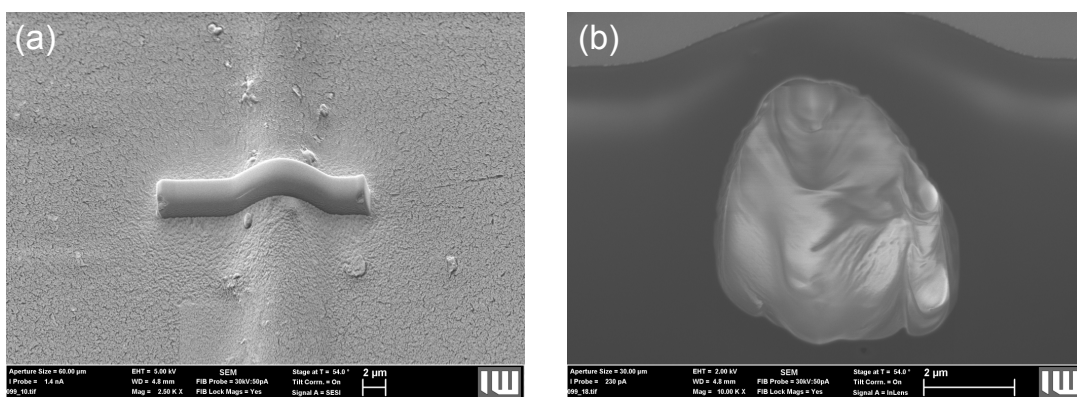


**Figure 3.5:** SEM images of embedded femtosecond laser written structures. (a) Surface bulge due to pressure from the core of the modification track, emphasized by a 2  $\mu\text{m}$  thick Platinum bar. (b) Cross-sectional cut through the structure, exposing a cavity at the core.

A cross-sectional cut is shown in Figure 3.5(b). The core of the structures is confirmed as a cavity which forms during the fabrication process. The slight asymmetry of the structure, in contrast to Figure 3.4, is explained by its proximity to the surface. While an expanding plasma spot at a writing depth of  $150\ \mu\text{m}$  is experiencing the same back pressure in every radial direction, close to the surface, the material buckles more easily.

The utilized FIB-SEM setup is located at the *Institut für Werkstoffkunde* and was operated with the help of Dr.-Ing. Torsten Heidenblut.

### Discussion

Combining the results for the evolution of a modification track obtained in the previous sections leads to the proposal of the following mechanism: A single tightly focused femtosecond laser pulse triggers nonlinear photoionization in the material and ignites a plasma. Since the critical power is exceeded, a short segment of filament propagation occurs. The temperature rises above the threshold for random chain scission of the polymer which results in a small cavity. Since the glass transition temperature of PMMA is surpassed even some micrometers away from the focal spot, the area surrounding the structure is still affected by heat due to thermal diffusion from the center. Also, a quickly expanding plasma core applies stress on the medium which can result in tension cracks. When the structures of individual pulses begin to spatially overlap, the focused laser beam is distorted by existing material modifications and the filament propagation is disturbed. The cavities of adjacent structures begin to merge. The encapsulated gas is repeatedly heated by subsequent pulses and applies pressure on the surrounding material. At sufficiently small distances between consecutive pulses, a continuous modification track with circular symmetry emerges.

This analysis leaves the following key parameters for waveguide writing in PMMA:

- The utilized pulse energies should be in the order of  $E_p = 100\ \text{nJ} - 700\ \text{nJ}$ .
- For waveguide writing in the athermal and thermal regime repetition rates of  $f_{\text{rep}} = 1\ \text{kHz}$  and  $f_{\text{rep}} = 100\ \text{kHz}$  are applied, respectively.
- To achieve a continuous and homogeneous modification track, the spacing between consecutive spots should be in the order of  $\Delta x \approx 0.5\ \mu\text{m}$ . Consequently, at a given repetition rate, a guiding value for the writing speed  $v$  is given by  $v = f_{\text{rep}} \Delta x$ .

## 3.2 Single-track waveguides

In the previous sections, the morphology and evolution of femtosecond laser written modification tracks were studied. Now their waveguiding capabilities are examined.

### 3.2.1 Refractive index change mechanism

To observe waveguiding, light at different test-wavelengths is coupled into the structures utilizing the setup described in Section 2.3.2.

In the athermal regime, at 1 kHz and 10 kHz repetition rate, no waveguiding is observed for continuous modification tracks with circular cross section. However, when moving the fabrication parameters deep into the heat accumulation regime, at 100 kHz, light can be guided across the entire sample. Figure 3.6(a) shows a microscope image of the polished end-facet of such a modification track. Figure 3.6(b) shows the annular intensity distribution of a guided mode completely surrounding the modification track; it can therefore be called a tubular waveguide. The non-guiding part in the center exactly matches the diameter of the structural modification visible in Figure 3.6(a). This means that the refractive index increase responsible for waveguiding can not be seen under light microscopy. Similar tubular waveguides in the thermal regime were reported in [Zou04] and [Eat12] with repetition rates of the writing laser of 25 MHz and 500 kHz, respectively. Images of the referenced waveguides were reproduced in Figure 1.21 in Section 1.3.6.

These results indicate that heat-accumulation plays an important role in the formation of a continuous refractive index modification. It can be assumed that a gas at a constant high temperature inside the cavity of a modification track homogeneously applies pressure on the surrounding medium. The material gets compressed

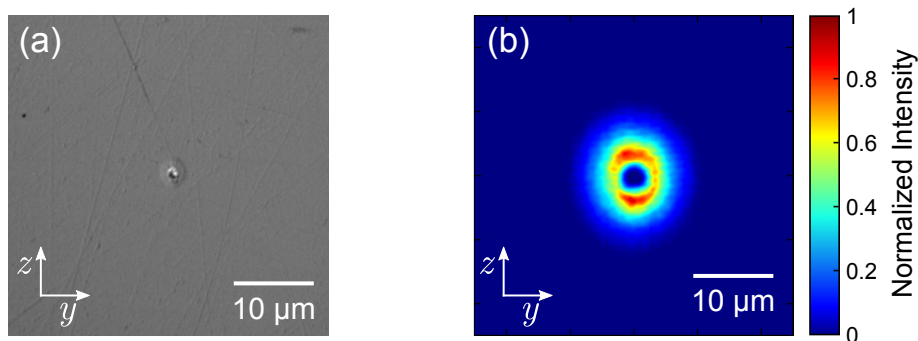


**Figure 3.6:** Left: Microscope image of a waveguide written at the low-energy thermal regime. Right: False color representation of an annular intensity distribution of the corresponding guided mode.

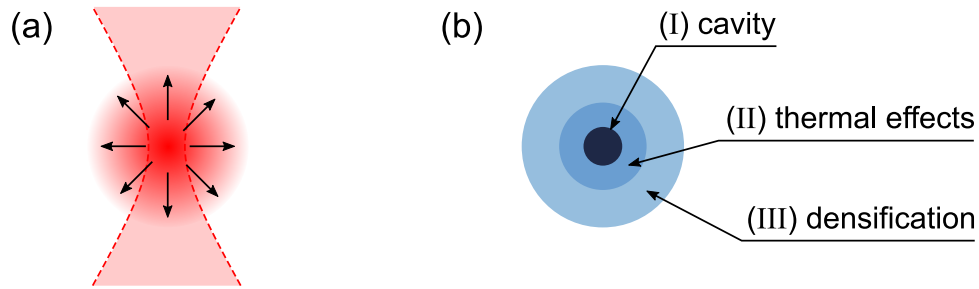


**Figure 3.7:** Schematic representation of the refractive index change mechanism during waveguide writing. (a) An expanding plasma core at the center of the focus spot applies radial pressure on the surrounding material. (b) After processing, three zones can be distinguished on the final structure: (I) A cavity at the center which matches in dimension the spot size of the focused laser beam. (II) An inner ring of material modification affected by melting and resolidifying. (III) An outer ring of increased refractive index due to material densification.

even in areas that are not visibly affected by melting, resulting in an increase in refractive index. The proposed mechanism for the formation of a positive refractive index contrast is schematically depicted in Figure 3.7.

It should be noted that, even at an optimal repetition rate of 100 kHz, not every track with a circular cross section supports tubular waveguiding. The other writing parameters still have to be chosen carefully. To reliably achieve a tubular waveguide, pulse energies of 180–220 nJ and writing speeds of 50–60 mm/s yield the best results when focusing with a 0.55-NA aspheric lens.

Even though no waveguiding was observable when writing with lower repetition rates, zones of increased refractive index are still expected to form. The fundamental mechanism of a quickly expanding plasma at the focal spot which applies stress on the surrounding material is still valid. However, for waveguiding, a smooth and uniform refractive index modification is required to keep scattering losses at a minimum. It appears as if heat-accumulation is the key to achieve a continuous refractive index modification suitable for waveguiding. In the athermal regime, the refractive index modification is likely disturbed along the track which quickly results in the loss of coupled light. Since the exact morphology of the refractive index modification is currently not experimentally accessible, further investigations are necessary.

At this point it becomes clear that the most basic waveguide geometry, where the refractive index increase emerges directly from the irradiated volume (see Section 1.3), can not be realized with the available laser system. A huge writing parameter scan was performed to find a different modification regime. But since all suitable pulse energies yield peak powers above the critical power, material damage always

emerges at the center of the focal volume. If waveguides with a circular instead of an annular guided mode are desired, different writing geometries have to be explored.

### 3.2.2 Refocusing effect

In a nonlinear photoionization process, not the entire pulse energy is transferred into the material. Studies suggest that an absorption of approximately 50% can be expected [Eat05]. If enough energy is left, the pulse can in principle trigger another nonlinear photoionization process if it is focused again.

Refocusing is experimentally found to appear during femtosecond laser waveguide writing. The annular refractive index increase thereby acts as a lens on the unabsorbed light while self-focusing counteracts the divergence of the beam and a secondary focus forms resulting in a secondary material modification. This process, however, turns out to strongly depend on the initial focusing conditions. The evolution of the track morphology for pulses with 500 nJ energy focused with 0.40-NA, 0.55-NA and 0.65-NA aspheric lenses is displayed in Figure 3.8.

As already discussed in Section 3.1.1, single pulse modifications look alike regarding physical appearance and size for all focusing lenses. This feature can be seen

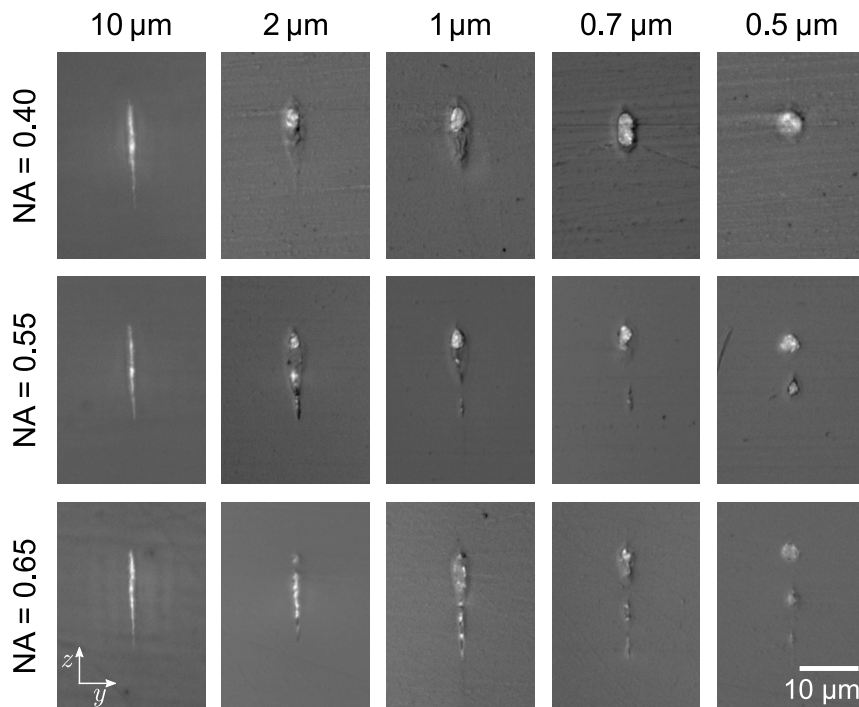


**Figure 3.8:** Microscope images of the cross-sectional evolution of the modification track at 500 nJ. Focusing was done with different aspheric lenses with a numerical aperture of 0.40, 0.55 and 0.65. Laser irradiation was from top.



in Figure 3.8 for a spacing of 10  $\mu\text{m}$  between spots. At a distance of 2  $\mu\text{m}$  between consecutive pulses, the deviations for different focusing lenses become apparent. For a 0.40-NA lens, a droplet begins to form which evolves into a circular modification much like it does for low-energy pulses (see Figure 3.4). At stronger focusing on the other hand, the vertical dimensions of the structures remain very much the same as for a single-pulse modification. At 0.55-NA focusing, the modification ultimately splits into two separate parts while at 0.65-NA, even a third modification emerges. The onset for a secondary modification is observed at pulse energies around 250 nJ. A tertiary modification begins to form at pulse energies around 400 nJ when the beam is focused with the 0.65-NA lens. This effect occurs independently of the repetition rate which is consistent with previous observations (see Section 3.1.3).

The exact mechanism responsible for the formation of this refocusing effect is a complex interaction of many variables. The change in refractive index caused by the primary modification as well as the cavity at the core and the thermally affect zone have to be taken into account. When the beam overlaps with an existing material modification, the light-material interaction is not a symmetric process anymore as it would be the case for a homogeneous medium. As a result of this overlap, the assumption of a Gaussian beam may become invalid and result in an entirely different intensity distribution at the focal spot. To disentangle all possible influences additional investigations and experiments are necessary, e.g., pump-probe experiments. However, the size of the primary modification is identified to play an important role in the formation of a secondary modification. If it becomes too big, the refocusing effect is reduced and no secondary track occurs which seems to be the case when focusing with a 0.40-NA lens. Similar observations regarding refocusing effects in PMMA were reported in [Eat12]. It is an interesting question if this is a material specific effect or if refocusing during waveguide writing appears in other materials as well. Throughout the literature research conducted for this work, no publications were encountered with similar refocusing effects in either glasses or crystals.

With the onset of the refocusing effect, the morphology of the refractive index modification becomes more complex due to the interaction of two simultaneously forming modification tracks. Waveguide writing with a refocusing effect is from now on called *cascaded-focus writing*. Figure 3.9 shows three possible intensity distributions of guided modes for structures written with a cascaded focus. The waveguides are written at the standard depth of 150  $\mu\text{m}$  below the surface. Focusing of the laser beam is done with the 0.65-NA aspheric lens for which the refocusing effect is most prominent.

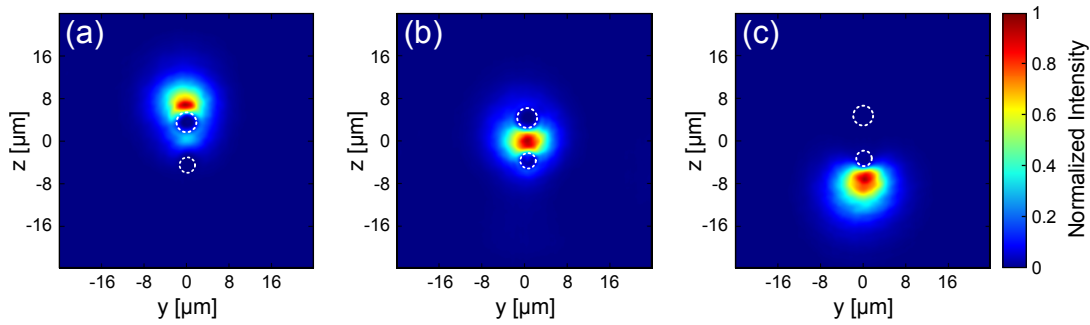


**Figure 3.9:** Intensity distributions of waveguides written with an aspheric lens with an NA of 0.65. (a) 300 nJ and 40 mm/s. Guiding takes place above the primary modification. (b) 300 nJ and 50 mm/s. Guiding takes place between the primary and the secondary modification. (c) 400 nJ and 50 mm/s. Guiding takes place below the secondary modification. The white dotted circles mark the outside margins of the visible primary and secondary modifications.

At the onset of the refocusing effect, at 300 nJ and a writing speed of 40 mm/s, the emerging secondary structure distorts the lower half of the index modification created by the primary modification. The upper part, however, is unaffected and light guiding is still observable there. This situation is displayed in Figure 3.9(a). If the writing speed is increased to 50 mm/s, the dynamic changes. Light may now be guided between the primary and secondary modification, as is shown in Figure 3.9(b). A similar configuration was reported in [Eat12]. This observation suggests a constructive interaction between two simultaneously forming modifications. The vertical space between the tracks can then be thought of as being compressed from above and below, resulting in a waveguide core of increased refractive index.

If the pulse energy gets increased to values  $\geq 400$  nJ, the interaction changes again. An almost symmetric fundamental mode waveguide forms beneath the secondary modification. At the same time, the index modification of the primary modification is fully distorted and no waveguiding is observable there. This configuration is shown in Figure 3.9(c). The primary modification appears to channel the stress caused by the secondary modification downwards. At higher pulse energies, more energy is available for the modification process in the secondary focus as well and it becomes responsible for the dominant index modification. This configuration proves to form very reliably for a large set of writing parameters when the pulse energy is above 400 nJ. Furthermore, the highest light transmission is measured for this type of waveguide. This kind of cascaded-focus waveguide, with guiding below the secondary modification, will be thoroughly characterized in the next section.

### 3.2.3 Cascaded-focus waveguide writing

The refocusing effect, introduced in the previous section, was shown to be beneficial for creating almost symmetric waveguides with a circular cross section below the secondary material modification. An exemplary cross-sectional microscope image of the the material modification and the intensity distribution of the corresponding guided mode is shown in Figure 3.10(a) and (b), respectively [Pä16].

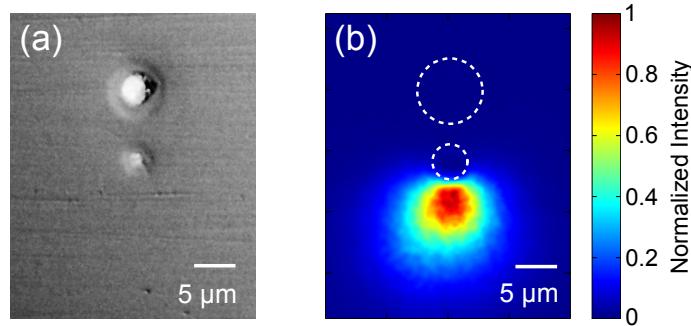


**Figure 3.10:** (a) Bright-field microscope image of a polished end facet of a cascaded-focus material modification fabricated at 100 kHz repetition rate. Pulse energy was 550 nJ and the writing speed 35 mm/s. (b) Intensity distribution of the corresponding guided mode at a 660 nm test-wavelength. The white dotted line marks the outside margins of the primary and secondary modification.

To limit the number of material modifications to two, the 0.55-NA aspheric lens is chosen for the following experiments. Optimal waveguides are achieved for pulse energies between 400–650 nJ at a fixed repetition rate of 100 kHz and a writing depth of 150 μm. The entrance facet of a waveguide is scanned horizontally and vertically with the tip of the single-mode fiber coupling light into the waveguide. When doing so, no higher-order modes are observed, only a variation in transmitted power due to changes in coupling efficiency. The normalized frequency  $V = \frac{2\pi a}{\lambda} \text{NA}$  is calculated by estimating the radius of the waveguide core from the mode-field diameter of the measured intensity distribution. The calculated values between  $V = 1.2$  and  $V = 2.0$  satisfy the condition  $V < 2.405$  for single-mode operation (see Section 1.1.2).

#### Writing parameter evaluation

Even though the waveguide morphology and guiding properties appear to be identical within the just established fabrication regime, the success of the fabrication process can strongly vary depending on the writing parameters. Non-optimal writing parameters result in a higher likelihood for a defective waveguide. A statistical

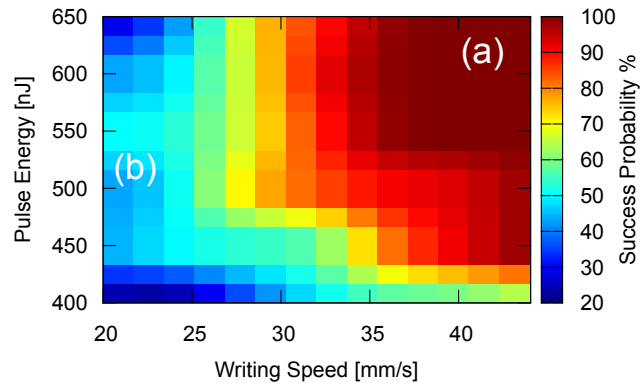


**Figure 3.11:** Success probability of the fabrication process as a function of the writing speed and the pulse energy. (a) A success probability of almost 100 % is achieved in the dark red area. (b) Too slow writing speeds has the success probability quickly drop below 50 %.

analysis of 650 individual waveguides relates pulse energy and writing speed to a success probability expressing if the writing process leads to a functional waveguide or not. The results are displayed in Figure 3.11 [Pä16].

In parameter ranges of  $v = 35 - 45 \text{ mm/s}$  and  $E_p = 550 - 650 \text{ nJ}$ , the success probability for the fabrication process is almost 100 %, as indicated by the dark red area in Figure 3.11. An exemplary microscope image shows a top view of an optimal homogeneous waveguide structure in Figure 3.12(a). A malfunction of the waveguide only occurs if the sample exhibits massive shortcomings, such as deep surface scratches, craters or enclaves in the material. Moving towards lower writing speeds and pulse energies, the success probability quickly drops below 50 %. Lower writing speeds correspond to more pulses overlapping at each point in space. Thereby, the risk for defects is increased and the edges of the modification track become rougher

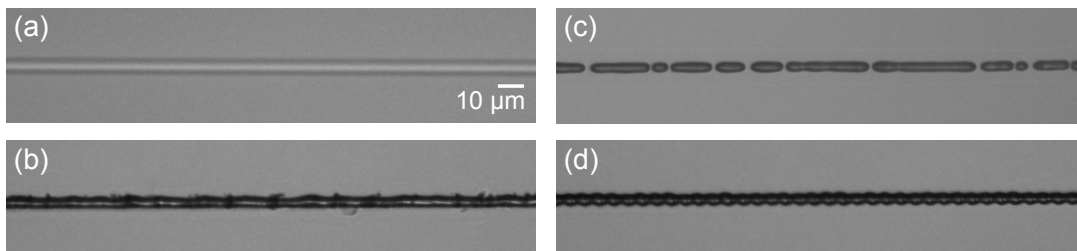


**Figure 3.12:** Microscope images of modification tracks fabricated with different writing parameters. Writing direction was from left to right in every image. (a) Homogeneous material modification optimal for waveguiding. (b) Frayed edges caused by too slow writing speeds. (c) Nonperiodic disruptions caused by too large pulse energies. (d) Periodic disruptions triggered by disturbances on the laser beam.

as well which can significantly increase the propagation losses. Figure 3.12(b) shows the frayed edges of a waveguide due to too low writing speed. Pulse energies above 650 nJ result in nonperiodic disruptions along the waveguide track which can be seen in Figure 3.12(c). Fluctuations in the energy input can be the cause of these disruptions and indicate that the writing process becomes instable. Periodic disruptions as shown in Figure 3.12(d) can occur at any writing parameter combination. They are linked to disturbances of the laser beam upon entering the substrate or hitting a material impurity during the writing process. The influence of the edge was eliminated by pre-polishing the substrates. A smooth edge allows for a clean transition of the laser beam from air into the medium. The origins of periodic modulations are discussed in Section 1.3.4.

### Refractive index contrast

The refractive index contrast is an important characteristic of a femtosecond laser written waveguide. From Equation (1.4), the relation  $NA \approx \sqrt{2n_1\Delta n}$  is known which links the numerical aperture to the refractive index increase of the waveguide core. Therefore, measuring the NA gives an estimate for  $\Delta n$ . The numerical aperture is calculated by measuring the acceptance angle of a waveguide using the method described in Section 2.3.3. There was no obvious dependence of  $\Delta n$  on the writing speed or the pulse energy. Both variables were then combined into the energy dosage  $D = E_{p,rep}/A_v$  (see Section 1.3.1), with  $A$  being the focal spot area. The refractive index contrast  $\Delta n$  as a function of  $D$  is shown in Figure 3.13. The average refractive index contrast is calculated to be  $\Delta n = 6.2 \cdot 10^{-4}$ . The missing dependency of  $\Delta n$

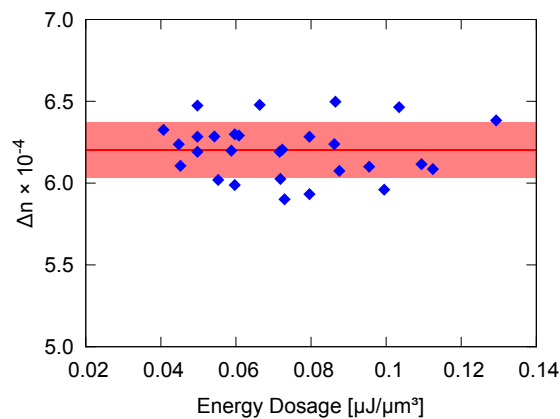


**Figure 3.13:** Refractive index contrast  $\Delta n$  as a function of the energy dosage  $D$ . The red line marks the average  $\Delta n$ , with the highlighted background being the standard deviation.

on the writing parameters is contrary to reports in [Sow06] where the index contrast of femtosecond laser written waveguides in PMMA was clearly linked to the pulse energy. This discrepancy can be explained by the fact that most likely two different mechanisms are responsible for the formation of the index contrast. In [Sow06], the refractive index increase is reported to form directly in the focal volume whereas in this work it forms outside the focus. For the proposed model of material stress being the cause for the refractive index increase (see Section 3.2.1), the lack of dependence of  $\Delta n$  on the pulse energy implies that the maximum possible densification by a single modification track is already reached at much lower pulse energies. However, increasing the pulse energy to a certain point has the advantage of stabilizing the writing process to a 100% fabrication success rate if the writing speed is matched appropriately (see Figure 3.11).

Scanning the same track multiple times, also called “overscanning”, was reported to increase the magnitude of the refractive index modifications in some instances [Bau08, Scu03]. During the experimentation done for this work, however, overscanning was found to have no benefit. Rather to the contrary, existing waveguides are corrupted or destroyed by repeatedly scanning the same track. Overscanning may be beneficial when working in a writing parameter regime below the critical power.

## Losses

The attenuation of light during propagation is the key property for defining the quality of a manufactured waveguide. These propagation losses were experimentally obtained by the method proposed in Section 2.3.4. Averaging over multiple waveguides written with the same parameters gives a good estimation for the losses in a specific processing window.

The pulse energy was set to 550 nJ for the conducted experiments and the writing speed was set to four different values in the optimal range: 32 mm/s, 36 mm/s, 40 mm/s and 44 mm/s. The length  $l$  of the waveguides was between 18 mm and 46 mm. Waveguides were analyzed at 660 nm and 850 nm test-wavelength. The insertion losses averaged over all waveguides of the same length as function of  $l$  are shown in Figure 3.14. The average propagation losses are measured to be  $0.59 \pm 0.07$  dB/cm and  $0.54 \pm 0.05$  dB/cm for 660 nm and 850 nm, respectively. Slightly lower losses in the NIR may be explained by the smaller intrinsic absorption of PMMA at that wavelength. The propagation losses are significantly lower than the losses reported in the literature so far which are stated to be around 3–6 dB/cm [Eat12].

The y-axis intercept gives information about further loss terms. Assuming that the Fresnel losses can be regarded as constant with  $FL \approx 0.17$  dB (see Section 2.3.4),

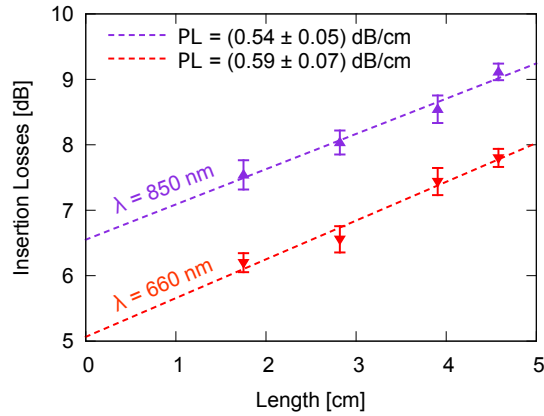


**Figure 3.14:** Insertion losses as function of the waveguide length for guided light at 600 nm and 850 nm. The propagation losses (PL) are determined from a linear fit. The errorbars are the standard error of the sampling distribution.

the coupling losses are calculated to be in the order of 4.6 dB at 660 nm and 6.2 dB at 850 nm. Variations in the mode field overlap are expected when coupling light from different fibers at different wavelengths. The result is a difference in coupling efficiency.

Evaluating this data set regarding the employed writing speeds shows no dependence of the propagation losses on the writing parameters within the investigated frame. The results are summarized in Table 1. Since the insertion losses for waveguides written at different pulse energies between 450 nJ and 650 nJ are identical to the values obtained at 550 nJ, it is concluded that the propagation losses are identical as well.

$v$ [mm/s]	$PL_{660}$ [dB/cm]	$PL_{850}$ [dB/cm]
44	$0.66 \pm 0.25$	$0.68 \pm 0.11$
40	$0.60 \pm 0.11$	$0.52 \pm 0.11$
36	$0.52 \pm 0.06$	$0.35 \pm 0.05$
32	$0.68 \pm 0.12$	$0.64 \pm 0.09$

**Table 1:** Propagation losses of waveguides fabricated at 100 kHz with a pulse energy of 550 nJ and different writing velocities, measured with 660 and 850 nm test wavelength.

## Summary

Cascaded-focus writing has proven to be a reliable approach for the fabrication of nearly symmetric fundamental-mode waveguides in PMMA with a single scan of the sample. A broad parameter frame of pulse energies and writing speeds has been established with a success probability of the writing process of almost 100 %. The av-

erage refractive index contrast which is achieved with this method is  $\Delta n = 6.2 \cdot 10^{-4}$ . The propagation losses are measured to be  $0.5 - 0.6 \text{ dB/cm}$  for wavelengths at 660 nm as well as 850 nm.

### 3.2.4 Phase gratings

Aside from their use as a waveguide, a single-track modification with a homogeneously distributed tubular refractive index increase (see Section 3.2.1) is a promising structure to create phase gratings. To fabricate gratings a series of modification tracks is consecutively written into a substrate with a lateral offset. Thereby, a set of gratings with a periodicity of  $10 \mu\text{m}$  was fabricated in PMMA at pulse energies between 100 nJ and 200 nJ to avoid the refocusing effect and obtain radially symmetric structures. The following analysis of phase gratings was done in collaboration with Christian Kelb. The gratings are evaluated utilizing a phase-retrieval algorithm developed and programmed by Christian Kelb which is based on a phase-retrieval approach first proposed in [Far91]. For detailed descriptions of the algorithm, the reader is referred to the original publication [Far91] as well as [Kel16].

To measure the diffraction efficiency, a grating is positioned perpendicular to the beam of a He-Ne laser at 633 nm wavelength and 4.5 mW average power. The intensities at the diffraction maxima of the orders  $\# = -8, \dots, +8$  are measured with a power meter. The experimental setup is displayed in Figure 3.15.

The diffraction efficiency of the  $+1^{\text{st}}$  diffraction order is measured to be  $\eta = 0.4\%$  at 100 nJ and  $\eta = 5.9\%$  at 200 nJ, respectively. This observation hints at the possibility of an energy dependence of the refractive index modification for pulse energies below the threshold for the refocusing effect. From the overall diffraction pattern, the phase retrieval algorithm calculates the phase function. The algorithm proves to be very robust and efficient. Results show that the pulse energy is correlated with

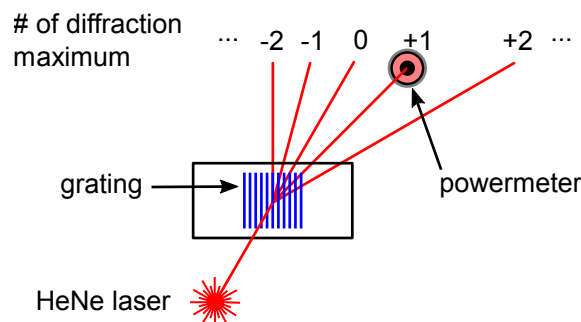


**Figure 3.15:** Setup to measure diffraction efficiencies of femtosecond laser written gratings.



the maximum phase deviation as well as the width of the modified volume. The latter is also observed experimentally when waveguide structures are evaluated via light microscopy (see Section 3.1.3). This phase retrieval-algorithm might prove a useful tool in future analysis of femtosecond laser written gratings.

### 3.3 Multi-track waveguides

In the following sections, the possibility to create waveguides by combining multiple modification tracks will be investigated. It starts with a simple dual-track approach and then moves on to more complex geometries. Waveguide geometries in general are discussed in Section 1.3.5.

#### 3.3.1 Dual-track waveguides

To create dual-track waveguides, the modification track written by the femtosecond laser has to create a horizontally distributed refractive index increase to its left and right flank. For fully merged modification tracks, discussed in Section 3.2.1 and 3.2.2, no strictly left-right distribution of the index modification was observed. Now, the not fully merged modification tracks are examined for waveguiding capabilities. The most promising candidates are tracks with spacings of  $\Delta x > 2 \mu\text{m}$  between the spots, when the cores do not get into contact yet. The necessary writing speeds for this configuration can be achieved for repetition rates  $f_{\text{rep}} \leq 10 \text{ kHz}$ .

Figure 3.16(a) shows a microscope image of the cross section of a modification track. The writing conditions in this exemplary case are  $f_{\text{rep}} = 10 \text{ kHz}$ ,  $E_p = 250 \text{ nJ}$  and  $v = 40 \text{ mm/s}$ . The laser beam is focused with a 0.55-NA aspheric lens. The key difference to previous writing parameters is that the resulting track consists of a series of individual spots which have not yet merged together. The result is an entirely different cross-sectional morphology. Figure 3.16(b) shows the intensity distributions of guided modes. It can be seen that guiding takes place on the left and the right side of the structure. However, only one waveguide can be coupled at a time and no cross-talk is observed between the two waveguides.

The refractive index increase is believed to be caused by a material densification in the vicinity of the quickly expanding irradiated core which applies stress on the surrounding material (see Section 3.2.1). A single-pulse modification can be assumed to be symmetric in the axial direction. Due to its elongated dimensions, as can be seen in Figure 3.16(a), it has a large surface area distributed around the axial direction. Therefore, a stress distribution and resulting radial refractive index increase,

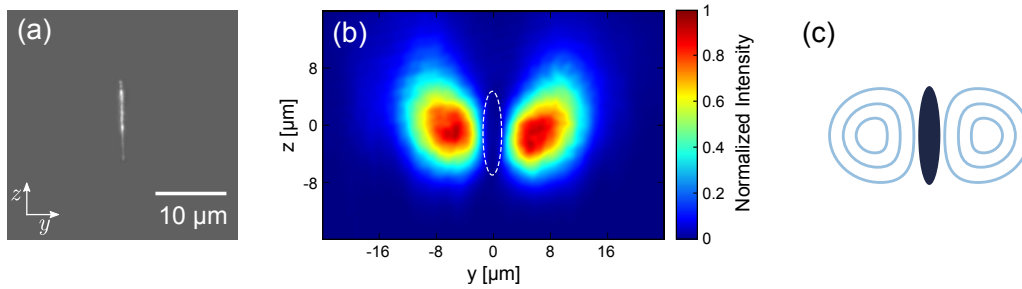


**Figure 3.16:** (a) Microscope image of the cross section of a single-pulse modification. The track was written with a 0.55-NA aspheric lens 150 μm below the surface at a repetition rate of 10 kHz, 250 nJ pulse energy and a writing speed of 40 mm/s. (b) False color representation of the intensity distribution of the corresponding guided modes at 638 nm. The plot is composed of two images since only one waveguide can be coupled at a time. (c) Schematic depiction of the material modification and stress distributions surrounding it.

as schematically depicted in Figure 3.16(c), can be expected. Since this zone of increased refractive index lies outside of the modification core, zones of adjacent spots can overlap without physical contact between the cores. Sufficient spacing between consecutive laser pulses also keeps the distortion of the laser beam at a minimum. The result is a continuous refractive index modification suitable for waveguiding as was demonstrated in Figure 3.16(b).

The proper spacing between spots was experimentally found to be 3–6 μm. Identical results may be achieved by applying any pulse energy between 200 nJ and 300 nJ. Within this frame, the writing parameters did not seem to affect the waveguide quality. At higher pulse energies, on the other hand, the observed effect vanished again. Additionally, the experiments were repeated at 1 kHz with the same spacing and pulse energies with identical results. This observation allows for the conclusion that the refractive index increases to the left and right of a track are independent of heat accumulation effects. They solely depend on the spatial overlap of index modifications created by individual pulses. Different focusing conditions did not affect the results, which is consistent with the observation that the modification morphology is dominated by filamentation before spots begin to merge together. The overall modification morphology appears very similar to observations made on femtosecond laser written waveguides in many crystalline materials (see Section 1.2.3).

### Fabrication method

To create a lateral overlap of the increased refractive index zones, two tracks are consecutively written next to each other with a lateral spacing of  $s$ , as schematically

shown in Figure 3.17. This spacing can also be used to influence the core size to some degree. Dual-track waveguides are written with a 0.55 NA aspheric lens at pulse energies between 200 nJ and 300 nJ at a depth of 150  $\mu\text{m}$ . The spatial separation between consecutive pulses is varied between 3  $\mu\text{m}$  and 5  $\mu\text{m}$ . To achieve higher processing speeds, the repetition rate was set to 10 kHz resulting in writing speeds of  $v = 30 - 50 \text{ mm/s}$  for the desired pulse spacing.

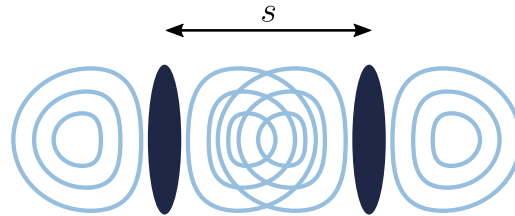


**Figure 3.17:** Schematic of a dual track waveguide. It is built up by overlapping two adjacent refractive index modification zones by placing two single-pulse tracks close to each other at a distance  $s$ .

### Characterization

After fabrication, the waveguides are optically evaluated. Bright-field microscopy images of the polished end-facet for the waveguides written at 200 nJ are depicted in the top row of Figure 3.18. Next, light is coupled into the structures to analyze the guiding properties. The bottom row of Figure 3.18 displays the mode profiles, each corresponding to the microscope image above.

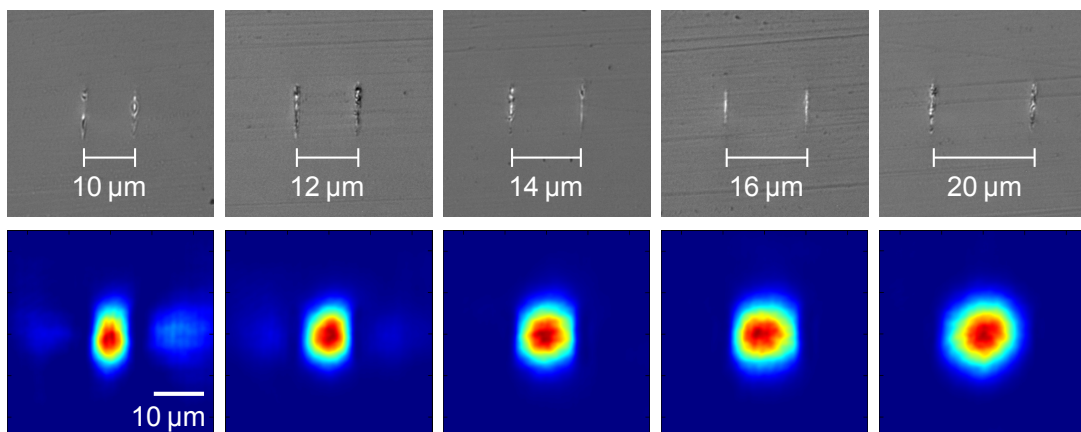


**Figure 3.18:** Dual-track waveguides with spacings of 10  $\mu\text{m}$ , 12  $\mu\text{m}$ , 14  $\mu\text{m}$ , 16  $\mu\text{m}$  and 20  $\mu\text{m}$ . Top row: bright field microscopy images of the waveguide cross section. Bottom row: Intensity distribution of the guided mode at 638 nm.

The best waveguides are achieved for writing speeds of 32–40 mm/s. At higher writing speeds, the transmitted power starts to decrease due to insufficient overlap between the index modification in writing direction. For  $s \leq 10 \mu\text{m}$ , no guiding is observed in between the two tracks. The mode profile is elliptical for  $s = 10 \mu\text{m}$  but it gets more and more circular with increasing  $s$  while the mode field diameter increases, as can be seen in Figure 3.18. The results at 250 nJ are virtually identical to experiments conducted at 200 nJ. At 300 nJ, guiding can still be observed to some degree but the mode profiles become less symmetric and less well-defined. The transmitted power is also reduced.

The refractive index contrast is measured to vary between  $\Delta n = 0.9 \cdot 10^{-3}$  and  $\Delta n = 1.2 \cdot 10^{-3}$  with no systematic dependence on the writing speed and pulse energy within the investigated parameter frame. However, it appears as if spacings of  $s \geq 12 \mu\text{m}$  are favorable. The average refractive index contrast is  $\Delta n = (1.0 \pm 0.1) \cdot 10^{-3}$  which is slightly larger than the value of  $6.2 \cdot 10^{-4}$  measured for single-track waveguides in Section 3.2.3. This result indicates that the influence of several modification tracks on the material may add up and result in a larger net refractive index modification.

The insertion losses are measured to be fairly high with values around 9–10 dB for a sample with 1 cm length. Assuming similar coupling losses as for single-track waveguides would result in propagation losses around  $4.5 \text{ dB/cm}$  which is nowhere near the previously measured values in the order of  $0.5 \text{ dB/cm}$ . With further adjustment of the writing parameters, it is imaginable to decrease the propagation losses of these dual-track waveguides in the future.

### 3.3.2 Cascaded-focus multi-track waveguides

The guiding between two fully merged modification tracks in the thermal regime was already shown for cascaded-focus waveguide writing (see Figure 3.9(b) in Section 3.2.2). However, in this configuration, the two modification tracks are vertically aligned and, since they are the result of a refocusing effect, their offset is not a controllable parameter. It is nevertheless desirable to combine the low propagation losses of cascaded-focus waveguides written in the thermal regime with the flexibility and control over the waveguide dimensions demonstrated for the dual-track approach.

First experiments showed that the dual-track approach is not suitable for modifications written with a cascaded focus. Waveguiding is not supported in between tracks but only at the outer edges. However, it is observed that both tracks have a mutual influence on the morphology of the induced refractive index change long

before the directly irradiated zones overlap. In a second step, a block of numerous modification tracks with a constant spacing of  $\Delta y = 16 \mu\text{m}$  was created. A dark-field microscope picture is shown in Figure 3.19(a). The interaction of several modifications over a larger distance leads to a collective densification between each set of neighboring tracks. This densification creates a well-defined zone of increased refractive index relative to the unaffected material which is suitable for waveguiding. An exemplary intensity distribution of a guided mode measured at 638 nm test-wavelength is shown in Figure 3.19(b).

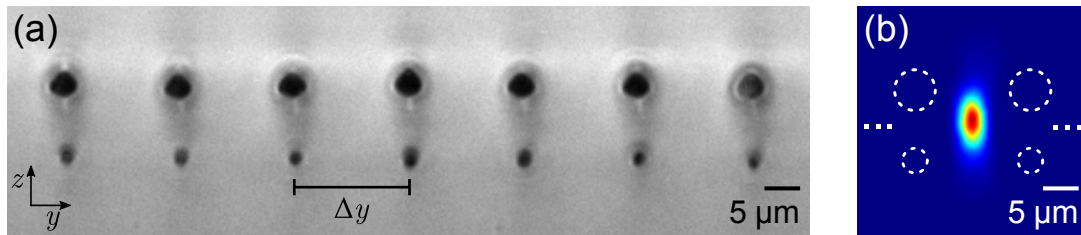


**Figure 3.19:** (a) Dark-field microscopy image of an ensemble of cascaded-focus modification tracks at a constant spacing of  $\Delta y = 16 \mu\text{m}$ . (b) Exemplary intensity distribution of a mode that can be guided between every two neighboring tracks. The white dotted circles mark the outside margins of the primary and secondary modification.

### Fabrication method

To maximize the densification effect for a single waveguide core and to minimize the lateral dimension of the structure at the same time, the modification tracks were moved as close together as possible except for a single variable spacing  $s$  in the middle. This concept is schematically depicted in Figure 3.20(a). Decreasing  $\Delta y$  below  $10 \mu\text{m}$  can result in distortions of the laser beam by the existing material modifications and lead to defects during the writing process. Therefore, the spacing in the blocks was kept constant at  $\Delta y = 10 \mu\text{m}$ . A dark-field microscope image of

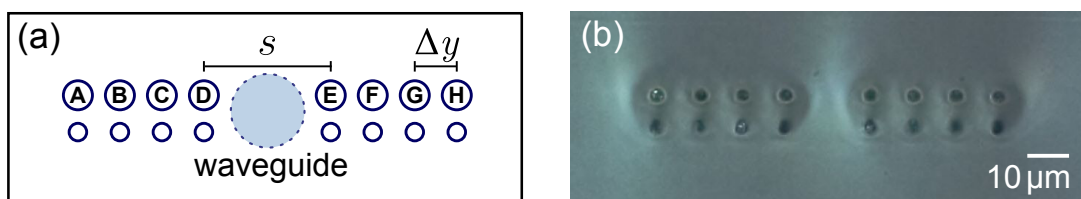


**Figure 3.20:** Cascaded-focus multi-track waveguide scheme. (a) Two blocks of four modifications with a spacing  $\Delta y$  in between are written into the material. In between the blocks, a lateral spacing  $s$  forms the core of the waveguide. (b) Cross-sectional dark field microscopy image of the end-facet of a multi-track waveguide.

the end-facet of a waveguide is shown in Figure 3.20(b). It can be seen that the heat affected zones of the modification tracks on each side of the core merge together and form a single modification block. At the waveguide core, the material gets compressed from two sides to achieve the highest densification for an optimal refractive index contrast. The spacing  $s$  between blocks may be used as a tuning parameter to influence the mode-field diameter of the waveguide, as was demonstrated for dual-track waveguides in Section 3.3.1. In principle, this writing geometry also works with blocks of two or three modifications on each side. The power transmission is reduced in this case, however. Increasing the number of modifications to five, on the other hand, did not show additional benefits. Therefore, four modifications on each side appear to be the optimal configuration.

Several experiments with varying writing parameters are conducted and optimal waveguides are observed at a repetition rate of  $f_{\text{rep}} = 100$  kHz, pulse energy of  $E_p = 450$  nJ and writing speed of  $v = 40$  mm/s which will be applied for the fabrication of all further multi-track waveguides. With the present setup, the modification tracks have to be written consecutively. Therefore, the influence of various writing sequences needs to be checked. For clarity, the tracks are labeled “A” through “H” as shown in Figure 3.20(a). No difference in the performance of the waveguide is found when writing “from-left-to-right” (A,B,C,D,E,F,G,H), “from-outside-to-inside” (A,B,C,D,H,G,E,F) and “from-inside-to-outside” (D,C,B,A,E,F,G,H). Alternating sequences, such as (A,H,B,G,C,F,D,E), were examined as well but experimentation showed that this scheme increases the risk of material defects during fabrication and a corrupted waveguide will later display higher scattering losses. For simplicity, the basic “from-left-to-right” sequence is chosen for the following measurements.

### Characterization

Typical mode profiles for multi-track waveguides are shown in Figure 3.21 for different lateral spacings [Pä17]. The smallest possible distance between two modification blocks for which waveguiding is still supported is observed at  $s = 16$   $\mu\text{m}$ . The mode profile is elliptical in this case as can be seen in Figure 3.21(a). The guided modes become more and more circular with increasing  $s$  as shown in Figures 3.21(b) and 3.21(c). This behavior is analogous to the observations for dual-track waveguides (compare Figure 3.18).

On the horizontal axis, the mode field diameter varies between 5  $\mu\text{m}$  and 10  $\mu\text{m}$  for  $s \leq 20$   $\mu\text{m}$ . On the vertical axis, on the other hand, it does not display any systematic dependence on the gap size and the dimension of the guided modes remains fairly

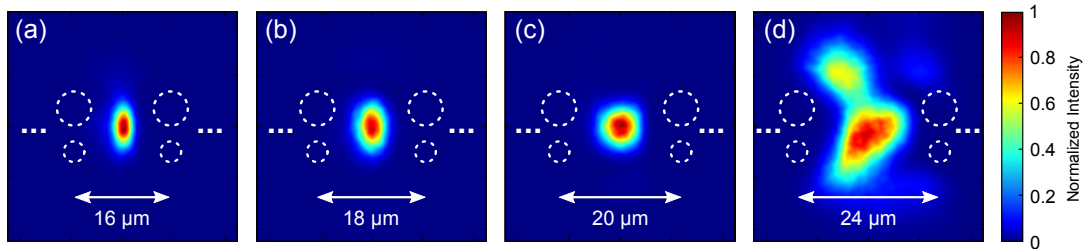


**Figure 3.21:** Intensity distributions of guided modes in false color representation for varying core sizes  $s$ . The white dots represent three additional modifications on each side with a respective distance of  $10\ \mu\text{m}$ .

constant at  $\sim 10\ \mu\text{m}$ . When scanning the entrance facet of the waveguide with the tip of the single-mode fiber horizontally, only changes in intensity of the transmitted light are observed but no higher-order modes. Doing the same in vertical direction gives similar results. However, additional waveguiding zones – above or below the central guide – can sometimes be coupled but display less transmission efficiency and poorer confinement. For  $s \geq 24\ \mu\text{m}$ , the guiding becomes multimode as can clearly be seen in Figure 3.21(d).

The numerical aperture is measured with the established method to get an estimate for the refractive index increase. Values between  $\Delta n = 1 \cdot 10^{-3}$  and  $\Delta n = 2 \cdot 10^{-3}$  are calculated, with higher values achieved at smaller  $s$ . Smaller lateral block-spacings result in a more dense compression of the material at the waveguide core which explains the larger refractive index contrast. The index contrast is larger than what was measured for single-track waveguides where the refractive index increase was only  $\Delta n = 6.2 \cdot 10^{-4}$ . The maximum measured value of  $\Delta n = 2 \cdot 10^{-3}$  even exceeds the index contrast of dual track waveguides. The values are also in the range of femtosecond laser induced refractive index modifications in PMMA reported in the literature [Zou04, Sow06, Bau10]. To calculate the normalized frequency, the core radius of a waveguide was estimated by the mode-field diameter of the measured intensity distributions. For  $s \leq 20\ \mu\text{m}$ , the values are between  $V = 1.8$  and  $V = 2.3$  which satisfy the condition  $V < 2.405$  for single-mode operation at 638 nm and 850 nm, respectively. This result is in agreement with experimental observations.

### Propagation losses

The propagation losses are measured using the established technique from Section 2.3.4. A set of samples with varying lengths between  $10\ \mu\text{m}$  and  $50\ \mu\text{m}$  were fabricated. The measured insertion losses as a function of  $l$  for 638 nm and 850 nm

test-wavelengths, are shown in Figure 3.22(a) and (b), respectively. The propagation losses were then calculated as the slope of a linear fit.

At a test-wavelength of 638 nm, the measured propagation losses are identical for spacings  $s = 18 - 22 \mu\text{m}$  and go down to  $0.3 \text{ dB/cm}$ . At  $s = 16 \mu\text{m}$ , the losses are a little bit higher which is an indication that the spacing between blocks is approaching its lower limit for an optimal waveguide core. A similar result is obtained for 850 nm, with losses as low as  $0.26 \text{ dB/cm}$ . The error of the linear regression is in the order of  $\pm 0.05 \text{ dB/cm}$  for both test-wavelengths. Taking systematic errors into account, such as the detection of scattered light, which is not part of the guided mode, the total error can conservatively be estimated to be  $\pm 0.1 \text{ dB/cm}$ . These measured propagation losses are one order of magnitude smaller than losses reported for other femtosecond laser written waveguides in polymers [Wat06, Eat12]. They also surpass the propagation losses of  $0.5 \text{ dB/cm}$  measured for single-track waveguides written with a cascaded focus which were discussed in Section 3.2.3. Recalling that the intrinsic material attenuation is given by the manufacturer as  $0.1 \text{ dB/cm}$ , the presented multi-track waveguides are getting close to this value.

The Fresnel losses are estimated to be  $0.17 \text{ dB}$  (see Section 2.3.4). Taking the entrance as well as the exiting facet into account and subtracting this value twice from the y-intercept gives an experimental value for the average coupling losses. The corresponding coupling efficiency therefore is around  $45 - 60\%$  depending on  $s$  as can be seen in Figure 3.22.

Coupling a free propagating beam into the waveguide via the  $0.16\text{-NA}$  lens allows for investigation of the polarization dependence of the waveguide. The beam is initially linearly p-polarized (parallel to the plane of the modification tracks) and is then rotated with a half-wave plate. Waveguiding was confirmed for p-polarization

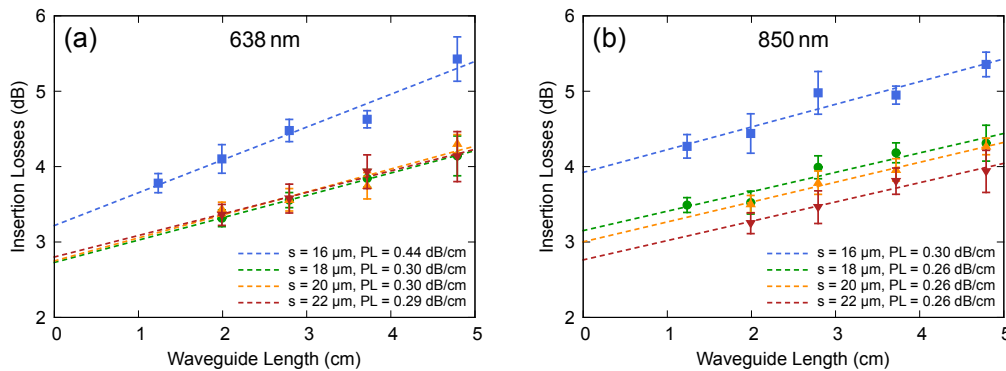


**Figure 3.22:** Insertion losses as a function of waveguide length for test-wavelengths (a)  $\lambda = 638 \text{ nm}$  and (b)  $\lambda = 850 \text{ nm}$ . Spacing for the waveguide core was  $s = 16, 18, 20$  and  $22 \mu\text{m}$ . Propagation losses are determined from a linear fit.



as well as for s-polarization. The transmitted power is measured to be approximately 15% higher for the s-polarization state. This can potentially be explained by micro roughnesses and inhomogeneities along the modification tracks which affect p-polarized light more.

### Bend losses

With the highest achieved refractive index contrast so far in this work and the lowest propagation losses, the multi-track waveguides are a good candidate for a systematical investigation of bend losses. Waveguides with a core spacing of  $s = 18\ \mu\text{m}$ , which show minimal propagation losses and an index contrast of  $\Delta n = 1.5 \cdot 10^{-3}$ , are chosen to achieve optimal bend performance.

To create an s-curved waveguide in this writing geometry, each modification track has to follow an individual path with varying radii of curvature at a constant angle  $\delta$  as shown in Figure 3.23. The radius  $R$  always refers to the center of the waveguide core and is constant for both curve segments. The length of the curve depends on  $R$  and the total covered angle which is  $2\delta$ .

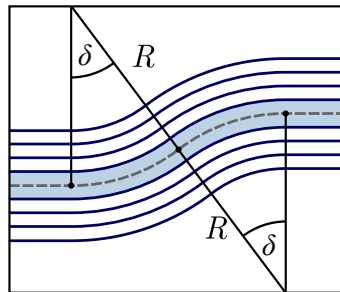


**Figure 3.23:** Schematic of a multi-track waveguide with an s-curve segment. Each track has to follow an individual path with varying radii of curvature. The reference radius  $R$  refers to the center of the waveguide.

Multiple waveguides with s-curve segments of varying lengths are fabricated. According to the method described in Section 3.3.2, the pure bend losses are obtained at 638 nm test-wavelength. The experimental data is to be compared to theoretically expected bend losses according to Equation (1.15) (see Section 1.1.3). The core radius of a waveguide is estimated from the mode-field diameter to be  $a = 3\ \mu\text{m}$ . The propagation constant is determined from the boundary condition that the electric field has to be continuous and differentiable at the interface between core and cladding (see Equation (1.12), Section 1.1.2). The effective refractive index then calculates to  $n_{\text{eff}} = 1.49062$ . With all the waveguide specifications known, the the-

oretical pure bend losses are calculated and displayed alongside the experimental data as a function of curve radius  $R$  in Figure 3.24.

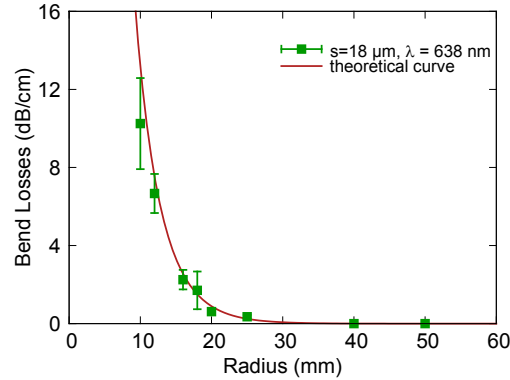


**Figure 3.24:** Bend losses per unit length of s-curved waveguides with  $s = 18 \mu\text{m}$  in dependency of the bend radius  $R$  measured at  $\lambda = 638 \text{ nm}$ . The theoretical curve was calculated with  $a = 3 \mu\text{m}$ ,  $\Delta n = 1.5 \cdot 10^{-3}$  and  $n_{\text{eff}} = 1.49062$ .

The agreement between the measured data and the theoretical curve is very good. It thereby confirms the refractive index contrast determined from the numerical aperture. Figure 3.24 shows that the bend losses are negligible for radii of curvature  $R \geq 20 \text{ mm}$ . The same applies for transition losses between a straight and a curved segment due to mode mismatch. For  $R < 20 \text{ mm}$ , the bend losses quickly increase to  $10 \text{ dB/cm}$  at a radius of  $10 \text{ mm}$ .

The literature reports on bend losses for femtosecond laser written waveguides in other materials. Similar bend losses were measured, for example, with a dual-track approach in Yb:YAG with a refractive index contrast of  $\Delta n = 3.2 \cdot 10^{-4}$  [Cal13]. Utilizing an annealing technique on single-track waveguides in glass [Arr13], the refractive index contrast was shown to increase up to  $\Delta n = 8.4 \cdot 10^{-3}$  which resulted in tolerable bend losses even at  $R = 16.6 \text{ mm}$ .

## Summary

The cascaded-focus multi-track waveguides exhibit by far the best performance of all waveguides investigated in this work. A symmetric fundamental mode is guided and the mode-field diameter can be influenced to some degree by adjusting the size of the waveguide core. The combined effect of multiple modification tracks involved in the formation of the waveguide results in an refractive index contrast of up to  $\Delta n = 2 \cdot 10^{-3}$ . The propagation losses were measured to go down to  $0.3 \text{ dB/cm}$ , approaching the limit of intrinsic material attenuation at  $0.1 \text{ dB/cm}$ . The

high refractive index contrast enables the fabrication of curved waveguides with negligible bend losses for radii of curvature  $R \geq 20$  mm.

Aside from all the advantages, it has to be mentioned that the fabrication time is increased by the larger number of modification tracks involved. Writing with multiple foci might be a solution here. Single-track waveguides displayed a broad parameter frame which basically results in identical quality waveguides (see Section 3.2.3). To achieve optimal multi-track waveguides, on the other hand, the pulse energy needs to be set very precisely to 450 nJ and the writing speed has to be 40 mm/s.

### 3.3.3 Photonic-crystal geometry

By distributing a cladding of air filled holes around a solid core, photonic crystal geometries have already been applied to confine a guided mode (see Section 1.1). The guiding principle is based on an effective index contrast between the core and the cladding. A periodic array of depressed index modifications in a honeycomb geometry was, for example, used to achieve waveguiding in glass [Gro15].

The single-track modifications with circular symmetry and a hollow core, as they form for pulse energies  $E_p \leq 250$  nJ (see Section 3.1.3), are ideal structures to establish this writing geometry for polymers as well. For first experiments, a honeycomb geometry is chosen with a periodic spacing of 10  $\mu\text{m}$  between the spots. Figure 3.25(a) shows a microscope image of an exemplary structure consisting of three rings. Light at 638 nm is coupled into the structure and guiding of a radially symmetric fundamental mode is observed, shown in Figure 3.25(b). It is unclear whether the cavities at the center of each modification track form cladding with

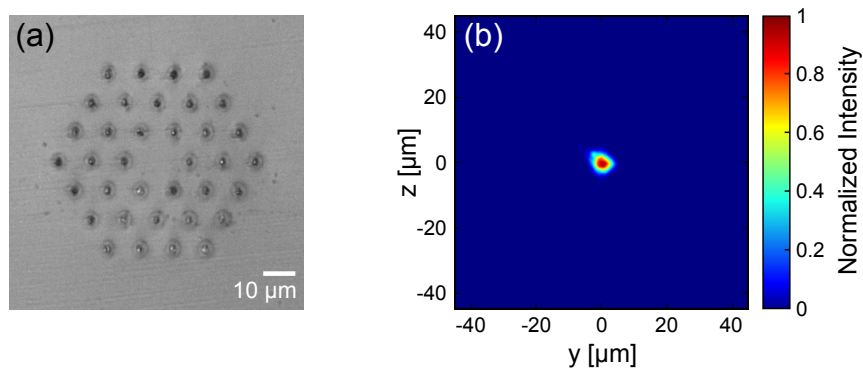


**Figure 3.25:** (a) Microscope image of the cross-section of a periodic cladding structure surrounding a waveguide core. (b) Intensity distribution of the corresponding mode guided at the core of the structure.

decreased effective refractive index or if the core displays a refractive index increase due to compression from every side. Taking all the observations from the previous sections into account, the latter is the more likely explanation. It was observed that at least three rings of material modification are necessary before guiding is supported at the core. That the cumulative effects of several modification tracks are needed to fabricate a functional waveguide is in agreement with observations made for multi-track waveguides (see Section 3.3.2).

After these successful proof-of-principle experiments, extensive parameter studies will be required to optimize the guiding properties of this waveguide geometry. Nevertheless, it is a promising design which especially has potential to further reduce bend losses due to a higher confinement of the guided mode.

## 3.4 Applications

The successful fabrication of low-loss single-mode waveguides in polymers in various writing geometries was demonstrated in the previous sections. In the following, some preliminary results for possible applications will be discussed.

### Surface interaction

All waveguides presented so far were written at a depth of 150  $\mu\text{m}$ . But it is of course possible to write a waveguide much closer to the surface. However, proximity to the surface can affect the emerging refractive index distribution for multiple reasons. Firstly, the surface may buckle under the pressure from the plasma core during the writing process (see Figure 3.5(a) in Section 3.1.3). Secondly, the focusing conditions of the writing beam can be different closer to the surface than at a larger depth (see Section 1.3.1). The second point may have an influence in particular when waveguide writing is done with a cascaded focus.

Nevertheless, with proper adjustment of the writing parameters, it is possible to fabricate a single-track waveguide just a few micrometers below the surface. If the refractive index increase is achieved above the primary modification, as was shown in Figure 3.9(a), interaction of the evanescent field with the surface is possible. It is demonstrated that the transmitted power of such a waveguide decreases when a droplet of index-matching oil is placed on the surface above it. The evanescent field of the guided mode leaks into the oil and light is lost. If the droplet is removed, the transmission returns to its original value.

Instead of an oil droplet, it is now imaginable to place a device, such as a ring resonator, on the surface directly above the waveguide. Via surface interaction,

various sensing applications become possible that depend on changes in resonance frequency of the ring resonator and the spectrum of light transmitted through the waveguide. For lab-on-a-chip applications, a whole waveguide network below the surface can be created to distribute light to a multitude of sensor elements located on the surface which enable space resolved measurements.

### Thin-film filter

Aside from evanescent coupling on the surface, another way of having a waveguide interact with another device is to have the light propagate right through it. For a proof-of-principle experiment, a set of multi-track waveguides is fabricated at the usual depth of  $150\ \mu\text{m}$ . Afterwards, a groove of  $300\ \mu\text{m}$  depth and  $25\ \mu\text{m}$  width is milled into the surface. The use of a polymer substrate is very advantageous at this point since milling can be done very easily. Test measurements confirm that light is still guided across the entire sample, despite the interruption along the way. However, the groove is responsible for additional losses in the order of 3–4 dB.

In a next step, a thin-film filter – fabricated by Melanie Gauch at *Laser Zentrum Hannover e.V.* – is inserted into the groove. A photograph of this assembly is shown on the left side of Figure 3.26. White light from a plasma source is coupled into the waveguide and the spectrum of the transmitted light is recorded by a spectrometer. The right side of Figure 3.26 shows a spectrum of the light transmitted through the thin-film filter via a waveguide. The design curve of the filter is also displayed in the graph. The experimental data overlaps quite well with the design curve if a tilt of  $17^\circ$  is considered. The tilt accounts for the fact that the filter does not sit perfectly upright in the groove, even though it was less than  $17^\circ$  in the tested configuration.

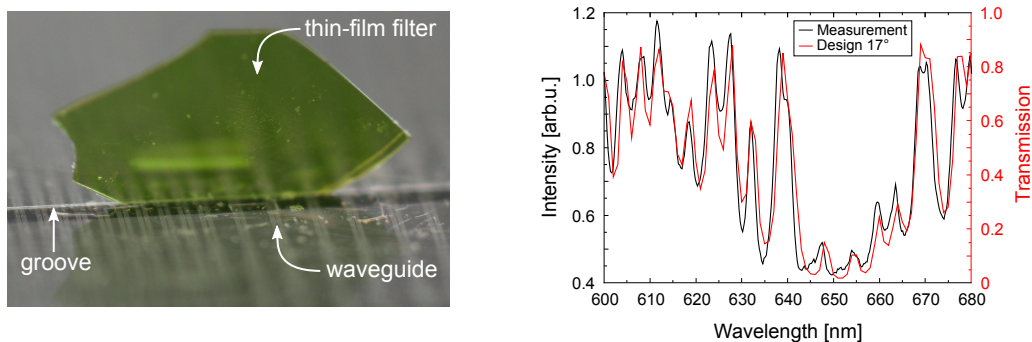


**Figure 3.26:** Left: Photograph of a thin-film filter sitting in a groove cut through a set of multi-track waveguides. Right: The black curve shows an excerpt of the intensity distribution of a measured spectrum of white light propagating through the filter via a waveguide. The red curve shows the design transmission of the filter at a tilt of  $17^\circ$ .

This discrepancy can be explained by deviations of the fabricated filter from its design. If light at the output of a waveguide which is unaffected by the filter is analyzed, no modulations in the spectral distribution are visible.

This configuration of a waveguide device can, for example, be used to separate certain wavelengths from a broad-band source in future waveguide networks and direct them to different channels when multiple band-pass filters are applied. The losses generated by the groove can be minimized by filling the gaps between filter and waveguide with an index matching liquid polymer and curing it.

### Self-phase modulation

The nonlinear refractive index of PMMA is in the order of  $n_2^I \approx 2.7 \cdot 10^{-14} \text{ cm}^2/\text{W}$  [Miw01]. Polymers can also easily be doped with additional components to shape the nonlinear refractive index in a desired way [Fer14]. This fact makes polymers an interesting material for applications relying on nonlinear effects. One common nonlinear effect is self-phase modulation (SPM). Self-phase modulation is caused by the Kerr-effect which is also responsible for self-focusing (see Section 1.3.1). The time-dependent intensity of an ultrashort pulse results in a time-dependent change in refractive index due to the Kerr-effect. This effect results in a phase-shift which leads to the formation of new frequency components.

For the first basic experiments, the writing laser at a central wavelength of 1048 nm is frequency doubled to 525 nm using a lithium triborate (LBO) crystal. The collimated beam is then coupled into a multi-track waveguide with a length of 35 mm by a 0.16-NA aspheric lens. The repetition rate is set to 1 kHz and the pulse energy is initially small to keep the average power low. The output of the waveguide is sent onto a spectrometer. The spectrum of small energy pulses is displayed in Figure 3.27(a).

The pulse energy is then slowly increased. With growing pulse energy, a spectral broadening due to self-phase modulation becomes apparent. The spectrum broadens by approximately 12 nm, as can be seen in Figure 3.27(b). However, the effect is short-lived since the pulse energies quickly reach values that trigger nonlinear photoionization as well. The spectral broadening vanishes again after a couple of seconds, most likely because of emerging alterations of the material.

From the referenced nonlinear refractive index a much larger spectral broadening due to SPM is to be expected. However, the deterioration of the waveguide makes it difficult to estimate experimental values for beam propagation simulations, because it is unknown how it affects the guiding properties of the waveguide. In experimentation it is observed that the transmitted power decreases significantly when

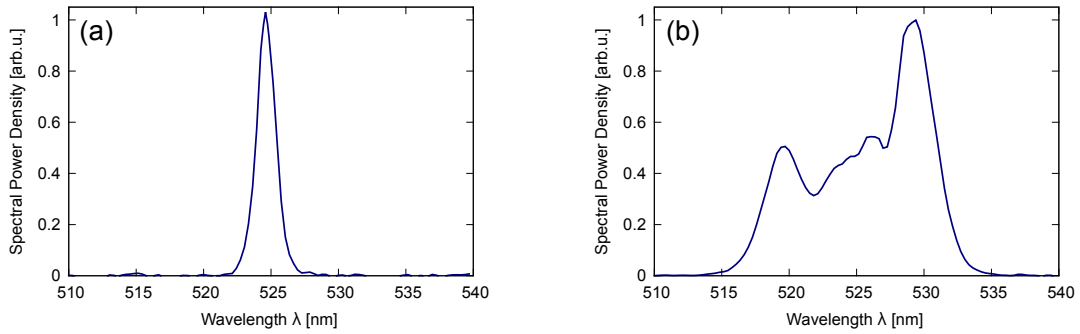


**Figure 3.27:** (a) Spectrum of a frequency doubled pulse at 525 nm central wavelength, recorded at the waveguide output for small pulse energies. (b) Spectral broadening due to self-phase modulation at increased pulse energies.

the waveguide is damaged. As the attenuation is continuously decreasing the peak power as a pulse propagates along a sample, it quickly becomes irrelevant to SPM contributions. This signifies that all spectral broadening would be generated in a small fraction of material at the beginning of the sample. Further experiments are required to find an operation regime where stable SPM is observable, that means below the modification threshold of the material. As soon as the effect is stable a solid foundation for beam propagation simulations is given and theoretical expectations can be compared to the experiment.

These preliminary studies open up a huge field of fundamental research on nonlinear effects in femtosecond laser written polymer waveguides. A point of special interest is how the refractive index modification created during the writing process affects the nonlinear refractive index and if special writing parameters can be used to achieve an optimal modification in  $n_2^I$ .

### 3.5 Critical remarks

The final section of this chapter will discuss some open questions and current limitations of waveguide writing in polymers.

One topic that needs to be addressed is the longterm stability of the waveguides. A time-dependence of such refractive index modifications was, for example, reported in [Liu10, Wat06] and attributed to stress relaxation and diffusion of photoinduced monomers into the bulk. To investigate longterm stability, the performance of the waveguides fabricated during this work was repeatedly tested over several months.

A majority of the single-track waveguides exhibit a decline in light transmission with progressing time. Recording the mode profile of a decaying waveguide during

that time frame shows that the mode-field diameter grows as the transmission decreases. This observation indicates that the induced refractive index modification spreads over a larger volume with time. Stress-relaxation is a possible cause for this behavior and would be consistent with the proposed mechanism that the refractive index increase is stress induced (see Section 3.2.1). But the results are ambiguous since a small number of waveguides display a stable performance over months and even years. Efforts to identify the mechanism or effect which is responsible for this stability have been unsuccessful so far. It should, however, be noted that either all waveguides in a sample decayed with time or all waveguides remained stable. By performing extensive parameter scans, the writing conditions could be ruled out as the source for the decay of the waveguides. Therefore, it is likely that fundamental material properties and ambient conditions play an important part in the stability of a waveguide. Storing the samples in opaque boxes in a low-humidity environment did have some beneficial effects on the durability but it could not stop the decay altogether.

At this point, it is unclear why some individual samples with single-track waveguides displayed longterm stability over the time frame of this work. The most likely explanation is based on intrinsic characteristics of the polymer material on a molecular level. Taking all precautions that were identified as beneficial for the waveguide stability and using optimal writing parameters results in single-track waveguides which display a stable performance for a period of more than 8 weeks before a decline in performance becomes noticeable. Multi-track waveguides on the other hand, did not show any signs of decay over the course of this work. Since the waveguide core is confined by a larger number of modification tracks, stress relaxation is apparently successfully prevented. Tempering a sample at 70 °C for 2 hours let the waveguides disappear in all cases.

The presented work was conducted in the material PMMA-03 by the company ChipShop. The writing principle is found to be transferable to PMMA materials by other manufacturers. The writing parameters always have to be adjusted to achieve similar waveguide performance, however. This means that the refractive index modification mechanism is very sensitive to the unique composition of additives in each individual material. Especially flexibilizers, which become relevant when working with polymer foils, seem to have a major impact on the formation of refractive index changes during femtosecond laser irradiation. Attempts to write single-track waveguides in a 175  $\mu\text{m}$  thin PMMA foil were hardly successful. Multi-track waveguides, on the other hand, were achieved in this material after a proper adjustment of the writing parameters. It should therefore be kept in mind that each new material



requires an optimization of the writing parameters and maybe even an adjustment of writing geometry. Also, some materials might be more suitable for femtosecond laser waveguide writing than others.

An overview of existing work on waveguide writing in polymers was given in Section 1.3.6. It has to be acknowledged that it was not possible to achieve an increase in refractive index directly in the focal volume, as was reported in [Sow06, Bau07]. In these works, Ti:sapphire laser sources with sub-200 fs pulses were applied. A waveguide configuration where the guiding takes place directly at the core of the modification track is still a desirable feature to achieve. However, it probably requires a femtosecond laser source with fundamentally different specifications from the one used in this work.



# Chapter 4

## Conclusion and Outlook

Within the scope of this thesis, femtosecond laser writing schemes for the fabrication of low-loss single-mode waveguides in PMMA have been developed. A refocusing effect during the writing process proved very beneficial for waveguide writing. Single-track waveguides fabricated with just a single scan of the material were achieved as well as multi-track waveguides composed of multiple structural modifications in the material.

First, the key writing parameters (pulse energy, repetition rate and translation speed) were thoroughly studied to reveal the optimal writing regime and investigate the evolution of a modification track. Optimal results are achieved in the heat accumulation regime at a repetition rate of 100 kHz. For low pulse energies ( $E_p \leq 250$  nJ), a cylindrical structure with a hollow core forms in the material. An annular zone of increased refractive index is induced by material compression and is uniformly distributed around the core. The index modification is found to be the result of stress and material densification caused by a quickly expanding plasma in the focal volume. The core of a modification track is determined to be a cavity.

Increasing the pulse energy can lead to a refocusing effect during the writing process which results in a secondary material modification below the primary modification track. The refocusing effect is found to strongly depend on the initial focusing conditions and requires an aspheric lens with a numerical aperture of 0.55 or higher. Using this effect for waveguide fabrication is named *cascaded-focus writing*. Writing with a cascaded focus results in a complex interaction between two simultaneously forming material modifications which also affects the distribution of the refractive index contrast. A configuration with a zone of increased refractive index below the secondary modification proved optimal for waveguiding. A detailed characterization of these single-track waveguides confirmed single-mode guiding, a refractive index contrast of  $\Delta n = 6.2 \cdot 10^{-4}$  and propagation losses in the order of 0.5 dB/cm for light at 660 nm and 850 nm alike.

In a second step, more complex waveguide geometries were studied. By far the best results were achieved using a multi-track approach where two blocks, each consisting of four modification tracks written with a cascaded focus, are fabricated. A gap between the blocks forms the waveguide core and exhibits stress from two sides which creates an optimal refractive index contrast of up to  $\Delta n = 2 \cdot 10^{-3}$ . The dimensions of the guided mode can be controlled by the size of the gap. Guiding of a symmetric fundamental mode is confirmed for this waveguide geometry and the propagation losses decrease to  $0.3 \text{ dB/cm}$ , the lowest value reported so far for femtosecond laser written waveguides in polymers. Due to the large index contrast, guiding through curves becomes feasible. A study on s-curved waveguides was conducted and the bend losses were found to be negligible for radii of curvature larger than 20 mm which is consistent with theoretical expectations.

In summary, the writing schemes for waveguide fabrication in PMMA presented in this work solve one of the biggest downsides of femtosecond laser written waveguides in polymers reported in the literature: High propagation losses in the order of  $3 - 6 \text{ dB/cm}$  [Eat12]. With only  $0.3 \text{ dB/cm}$  measured for multi-track waveguides, the propagation losses are approaching the intrinsic material attenuation. The demonstrated low-loss s-curved waveguides are the basic building blocks for waveguide splitters and couplers. Therefore, the application of femtosecond laser written waveguides becomes viable for all-polymer waveguide networks.

## Outlook

Future work may cover three different directions: Advanced studies regarding the fundamental modification process, further improvement of the waveguide performance and the implementation of the waveguides in lab-on-a-chip applications.

Pump-probe experiments would be the experimental tool of choice to deepen the understanding of the material modification process itself. A second laser beam has to be superimposed with the writing beam and provide probe pulses which interact with the excitation in the material caused by the pump pulse. The probe pulse is then collected by a detector. With an optical delay line, the time delay between pump and probe pulse is tuned and the variations in the probe signal gives insight about the excitation generated by the probe pulse, e.g., the decay of the free-electron density.

To increase the waveguide quality, various additions to the writing setup are imaginable. For example, an active beam-stabilization system can be implemented to counterbalance beam pointing fluctuations. A higher positional stability of the beam will result in decreased micro roughness of the modification tracks and therefore re-

duced scattering losses. For multi-track waveguides, it might also be advantageous to write the tracks simultaneously instead of consecutively. A spatial light modulator (SLM) can create multiple foci and was demonstrated to be suitable for simultaneous femtosecond laser writing [Pos09]. Another advantage of applying an SLM would be an increased processing speed. Complex waveguide geometries, such as the honeycomb waveguide in Section 3.3.3, also have the potential to advance the field of waveguide writing in polymers.

For applications in waveguide networks, the next logical step would be to fabricate x-couplers or y-junctions to be able to distribute light from one source into various waveguides. If a waveguide network gets combined with surface sensor elements which interact with the waveguides via evanescent coupling, space-resolved sensing becomes feasible. In the long run, it is imaginable that lab-on-a-chip devices are fabricated in a polymer foil which can be placed on the display of a hand-held device such as a smartphone or a tablet computer. The display supplies light for the waveguides and the signal of the surface sensors is collected by the front camera. An application analyzes the data and displays the result directly on the screen.



# Bibliography

- [Akt03] S. Akturk, M. Kimmel, P. O’Shea, R. Trebino, *Measuring pulse-front tilt in ultrashort pulses using GRENOUILLE*, *Optics Express* **11**(5), 491–501 (2003).
- [Ams05] M. Ams, G. D. Marshall, D. J. Spence, M. J. Withford, *Slit beam shaping method for femtosecond laser direct-write fabrication of symmetric waveguides in bulk glasses*, *Optics Express* **13**(15), 5676–5681 (2005).
- [Arr13] A. Arriola, S. Gross, N. Jovanovic, N. Charles, P. G. Tuthill, S. M. Olaizola, A. Fuerbach, M. J. Withford, *Low bend loss waveguides enable compact, efficient 3D photonic chips*, *Optics Express* **21**(3), 2978–2986 (2013).
- [Arr14] A. Arriola, S. Mukherjee, D. Choudhury, L. Labadie, R. R. Thomson, *Ultrafast laser inscription of mid-IR directional couplers for stellar interferometry*, *Optics Letters* **39**(16), 4820–4822 (2014).
- [Ass05] M. J. Assael, S. Botsios, K. Gialou, I. N. Metaxa, *Thermal conductivity of polymethyl methacrylate (PMMA) and borosilicate crown glass BK7*, *International Journal of Thermophysics* **26**(5), 1595–1605 (2005).
- [Bau07] A. Baum, P. J. Scully, M. Basanta, C. L. P. Thomas, P. R. Fielden, N. J. Goddard, W. Perrie, P. R. Chalker, *Photochemistry of refractive index structures in poly(methyl methacrylate) by femtosecond laser irradiation*, *Optics Letters* **32**(2), 190–192 (2007).
- [Bau08] A. Baum, P. J. Scully, W. Perrie, D. Jones, R. Issac, D. A. Jaroszynski, *Pulse-duration dependency of femtosecond laser refractive index modification in poly(methyl methacrylate)*, *Optics Letters* **33**(7), 651–653 (2008).
- [Bau10] A. Baum, P. J. Scully, W. Perrie, D. Liu, V. Lucarini, *Mechanisms of femtosecond laser-induced refractive index modification of poly(methyl*

- methacrylate*), Journal of the Optical Society of America B **27**(1), 107–111 (2010).
- [Bra12] F. Bragheri, P. Minzioni, R. Martínez Vázquez, N. Bellini, P. Paiè, C. Mondello, R. Ramponi, I. Cristiani, R. Osellame, *Optofluidic integrated cell sorter fabricated by femtosecond lasers*, Lab on a Chip **12**(19), 3779–3784 (2012).
- [Bur06] J. Burghoff, C. Grebing, S. Nolte, A. Tünnermann, *Efficient frequency doubling in femtosecond laser-written waveguides in lithium niobate*, Applied Physics Letters **89**(8), 081108 (2006).
- [Bur07] J. Burghoff, S. Nolte, A. Tünnermann, *Origins of waveguiding in femtosecond laser-structured LiNbO<sub>3</sub>*, Applied Physics A **89**(1), 127–132 (2007).
- [Cal13] T. Calmano, A.-G. Paschke, S. Müller, C. Kränkel, G. Huber, *Curved Yb:YAG waveguide lasers, fabricated by femtosecond laser inscription*, Optics Express **21**(21), 25501–25508 (2013).
- [Cau13] O. Caulier, D. Le Coq, E. Bychkov, P. Masselin, *Direct laser writing of buried waveguide in As<sub>2</sub>S<sub>3</sub> glass using a helical sample translation*, Optics Letters **38**(20), 4212–4215 (2013).
- [Cer02] G. Cerullo, R. Osellame, S. Taccheo, M. Marangoni, D. Polli, R. Ramponi, P. Laporta, S. De Silvestri, *Femtosecond micromachining of symmetric waveguides at 1.5 μm by astigmatic beam focusing*, Optics Letters **27**(21), 1938–1940 (2002).
- [Che14] F. Chen, J. R. Vázquez de Aldana, *Optical waveguides in crystalline dielectric materials produced by femtosecond-laser micromachining*, Laser & Photonics Reviews **8**(2), 251–275 (2014).
- [Cho14] D. Choudhury, J. R. Macdonald, A. K. Kar, *Ultrafast laser inscription: perspectives on future integrated applications*, Laser & Photonics Reviews 1–20 (2014).
- [Cor14] G. Corrielli, A. Crespi, R. Geremia, R. Ramponi, L. Sansoni, A. Santinelli, P. Mataloni, F. Sciarrino, R. Osellame, *Rotated waveplates in integrated waveguide optics*, Nature Communications **5** (2014).



- [Cru09] A. Ruiz de la Cruz, A. Ferrer, W. Gawelda, D. Puerto, M. Galván Sosa, J. Siegel, J. Solis, *Independent control of beam astigmatism and ellipticity using a SLM for fs-laser waveguide writing*, *Optics Express* **17**(23), 20853–20859 (2009).
- [D’A14] C. D’Amico, G. Cheng, C. Mauclair, J. Troles, L. Calvez, V. Nazabal, C. Caillaud, G. Martin, B. Arezki, E. LeCoarer, P. Kern, R. Stoian, *Large-mode-area infrared guiding in ultrafast laser written waveguides in Sulfur-based chalcogenide glasses*, *Optics Express* **22**(11), 13091–13101 (2014).
- [Dan15] R. Dangel, J. Hofrichter, F. Horst, D. Jubin, A. La Porta, N. Meier, I. M. Soganci, J. Weiss, B. J. Offrein, *Polymer waveguides for electro-optical integration in data centers and high-performance computers*, *Optics Express* **23**(4), 4736–4750 (2015).
- [Dav96] K. M. Davis, K. Miura, N. Sugimoto, K. Hirao, *Writing waveguides in glass with a femtosecond laser*, *Optics Letters* **21**(21), 1729–1731 (1996).
- [DB07] V. Diez-Blanco, J. Siegel, A. Ferrer, A. Ruiz de la Cruz, J. Solis, *Deep sub-surface waveguides with circular cross section produced by femtosecond laser writing*, *Applied Physics Letters* **91**(5), 051104 (2007).
- [DM11] C. De Marco, R. Suriano, M. Levi, S. Turri, S. M. Eaton, G. Cerullo, R. Osellame, *Femtosecond laser fabrication and characterization of microchannels and waveguides in methacrylate-based polymers*, *Microsystem Technologies* **18**(2), 183–190 (2011).
- [Dou15] G. Douglass, F. Dreisow, S. Gross, S. Nolte, M. J. Withford, *Towards femtosecond laser written arrayed waveguide gratings*, *Optics Express* **23**(16), 21392–21402 (2015).
- [Dre08] F. Dreisow, A. Szameit, M. Heinrich, T. Pertsch, S. Nolte, A. Tünnermann, *Second-order coupling in femtosecond-laser-written waveguide arrays*, *Optics Letters* **33**(22), 2689–2691 (2008).
- [Dub14] M. Dubov, V. Mezentsev, A. A. Manshina, I. A. Sokolov, A. V. Povolotskiy, Y. V. Petrov, *Waveguide fabrication in lithium-niobophosphate glasses by high repetition rate femtosecond laser: route to non-equilibrium material’s states*, *Optical Materials Express* **4**(6), 1197–1206 (2014).

- [DV05] G. Della Valle, R. Osellame, N. Chiodo, S. Taccheo, G. Cerullo, P. Laporta, A. Killi, U. Morgner, M. Lederer, D. Kopf, *C-band waveguide amplifier produced by femtosecond laser writing*, Optics Express **13**(16), 5976–5982 (2005).
- [DV09] G. Della Valle, R. Osellame, P. Laporta, *Micromachining of photonic devices by femtosecond laser pulses*, Journal of Optics A: Pure and Applied Optics **11**(1), 013001 (2009).
- [Eat05] S. M. Eaton, H. Zhang, P. R. Herman, F. Yoshino, L. Shah, J. Bovatsek, A. Y. Arai, *Heat accumulation effects in femtosecond laser-written waveguides with variable repetition rate*, Optics Express **13**(12), 4708–4716 (2005).
- [Eat06] S. Eaton, W. Chen, L. Zhang, H. Zhang, R. Iyer, J. Aitchison, P. Herman, *Telecom-band directional coupler written with femtosecond fiber laser*, IEEE Photonics Technology Letters **18**(20), 2174–2176 (2006).
- [Eat12] S. M. Eaton, C. De Marco, R. Martínez Vázquez, R. Ramponi, S. Turri, G. Cerullo, R. Osellame, *Femtosecond laser microstructuring for polymeric lab-on-chips*, Journal of Biophotonics **5**(8-9), 687–702 (2012).
- [Emo12] M. Emons, K. Obata, T. Binhammer, A. Ovsianikov, B. N. Chichkov, U. Morgner, *Two-photon polymerization technique with sub-50 nm resolution by sub-10 fs laser pulses*, Optical Materials Express **2**(7), 942–947 (2012).
- [Far91] M. W. Farn, *New iterative algorithm for the design of phase-only gratings*, in *Proceedings SPIE*, Band 1555, 34–42 (1991).
- [Fer03] M. Ferriol, A. Gentilhomme, M. Cochez, N. Oget, J. L. Mieloszynski, *Thermal degradation of poly (methyl methacrylate)(PMMA): modelling of DTG and TG curves*, Polymer Degradation and Stability **79**(2), 271–281 (2003).
- [Fer14] P. H. D. Ferreira, R. Stefanutti, F. J. Pavinatto, C. R. Mendonça, *Femtosecond laser fabrication of waveguides in DR13-doped PMMA*, Optics Communications **318**, 53–56 (2014).
- [Fib00] G. Fibich, A. L. Gaeta, *Critical power for self-focusing in bulk media and in hollow waveguides*, Optics Letters **25**(5), 335–337 (2000).

- [Gam78a] W. A. Gambling, H. Matsumura, C. M. Ragdale, *Field Deformation in a curved single-mode fibre*, Electronics Letters **14**(5), 130–132 (1978).
- [Gam78b] W. A. Gambling, H. Matsumura, C. M. Ragdale, R. A. Sammut, *Measurement of radiation loss in curved single-mode fibres*, IEE Journal on Microwaves, Optics and Acoustics **2**(4), 134–140 (1978).
- [Gat06] R. R. Gattass, L. R. Cerami, E. Mazur, *Micromachining of bulk glass with bursts of femtosecond laser pulses at variable repetition rates*, Optics Express **14**(12), 5279–5284 (2006).
- [Gat08] R. R. Gattass, E. Mazur, *Femtosecond laser micromachining in transparent materials*, Nature Photonics **2**(4), 219–225 (2008).
- [Gle97] E. N. Glezer, E. Mazur, *Ultrafast-laser driven micro-explosions in transparent materials*, Applied Physics Letters **71**(7), 882–884 (1997).
- [Goo47] F. Goos, H. Hänchen, *Ein neuer und fundamentaler Versuch zur Totalreflexion*, Annalen der Physik **436**(7-8), 333–346 (1947).
- [Gra07] R. Graf, A. Fernandez, M. Dubov, H. J. Brueckner, B. N. Chichkov, A. Apolonski, *Pearl-chain waveguides written at megahertz repetition rate*, Applied Physics B **87**(1), 21–27 (2007).
- [Gro13] S. Gross, M. Alberich, A. Arriola, M. J. Withford, A. Fuerbach, *Fabrication of fully integrated antiresonant reflecting optical waveguides using the femtosecond laser direct-write technique*, Optics Letters **38**(11), 1872–1874 (2013).
- [Gro15] S. Gross, M. Dubov, M. J. Withford, *On the use of the Type I and II scheme for classifying ultrafast laser direct-write photonics*, Optics Express **23**(6), 7767–7770 (2015).
- [Han15] T. Hanemann, K. Honnef, *Viscosity and refractive index adjustment of poly(methyl methacrylate-co-ethyleneglycol dimethacrylate) for application in microoptics*, Polymers for Advanced Technologies **26**(4), 294–299 (2015).
- [He10] F. He, H. Xu, Y. Cheng, J. Ni, H. Xiong, Z. Xu, K. Sugioka, K. Midorikawa, *Fabrication of microfluidic channels with a circular cross section using spatiotemporally focused femtosecond laser pulses*, Optics Letters **35**(7), 1106–1108 (2010).

- [Hir98] K. Hirao, K. Miura, *Writing waveguides and gratings in silica and related materials by a femtosecond laser*, Journal of Non-Crystalline Solids **239**(1–3), 91–95 (1998).
- [Hom99] D. Homoelle, S. Wielandy, A. L. Gaeta, N. F. Borrelli, C. Smith, *Infrared photosensitivity in silica glasses exposed to femtosecond laser pulses*, Optics Letters **24**(18), 1311–1313 (1999).
- [Hor12] W. Horn, S. Kroesen, J. Herrmann, J. Imbrock, C. Denz, *Electro-optical tunable waveguide Bragg gratings in lithium niobate induced by femtosecond laser writing*, Optics Express **20**(24), 26922–26928 (2012).
- [Hun09] R. G. Hunsperger, *Integrated Optics, Sixth Edition* (Springer Science+Business Media, 2009).
- [Juo06] S. Juodkazis, H. Misawa, T. Hashimoto, E. G. Gamaly, B. Luther-Davies, *Laser-induced microexplosion confined in a bulk of silica: Formation of nanovoids*, Applied Physics Letters **88**(20), 201909 (2006).
- [Kai00] A. Kaiser, B. Rethfeld, M. Vicanek, G. Simon, *Microscopic processes in dielectrics under irradiation by subpicosecond laser pulses*, Physical Review B **61**(17), 11437–11450 (2000).
- [Kai16] W. Kaiser, *Kunststoffchemie für Ingenieure: Von der Synthese bis zur Anwendung, 4. Auflage* (Hanser, 2016).
- [Kaz07] P. G. Kazansky, W. Yang, E. Bricchi, J. Bovatsek, A. Arai, Y. Shimotsuma, K. Miura, K. Hirao, *“Quill” writing with ultrashort light pulses in transparent materials*, Applied Physics Letters **90**(15), 151120 (2007).
- [Kei11] R. Keil, M. Heinrich, F. Dreisow, T. Pertsch, A. Tünnermann, S. Nolte, D. N. Christodoulides, A. Szameit, *All-optical routing and switching for three-dimensional photonic circuitry*, Scientific Reports **1** (2011).
- [Kel16] C. Kelb, W. M. Pätzold, U. Morgner, M. Rahlves, E. Reithmeier, B. Roth, *Characterization of femtosecond laser written gratings in PMMA using a phase-retrieval approach*, Optical Materials Express **6**(10), 3202–3209 (2016).
- [Kil04] A. Killi, U. Morgner, M. J. Lederer, D. Kopf, *Diode-pumped femtosecond laser oscillator with cavity dumping*, Optics Letters **29**(11), 1288–1290 (2004).

- [Len98] M. Lenzner, J. Krüger, S. Sartania, Z. Cheng, C. Spielmann, G. Mourou, W. Kautek, F. Krausz, *Femtosecond optical breakdown in dielectrics*, Physical Review Letters **80**(18), 4076–4079 (1998).
- [Lev15] S. Levy, M. Klebanov, A. Zadok, *High-Q ring resonators directly written in As<sub>2</sub>S<sub>3</sub> chalcogenide glass films*, Photonics Research **3**(3), 63–67 (2015).
- [Liu10] D. Liu, Z. Kuang, W. Perrie, P. J. Scully, A. Baum, S. P. Edwardson, E. Fearon, G. Dearden, K. G. Watkins, *High-speed uniform parallel 3D refractive index micro-structuring of poly(methyl methacrylate) for volume phase gratings*, Applied Physics B **101**(4), 817–823 (2010).
- [Mü12] S. Müller, T. Calmano, P. Metz, N.-O. Hansen, C. Kränkel, G. Huber, *Femtosecond-laser-written diode-pumped Pr:LiYF<sub>4</sub> waveguide laser*, Optics Letters **37**(24), 5223–5225 (2012).
- [Mas16] P. Masselin, E. Bychkov, D. Le Coq, *Direct laser writing of a low-loss waveguide with independent control over the transverse dimension and the refractive index contrast between the core and the cladding*, Optics Letters **41**(15), 3507–3510 (2016).
- [Mau08] C. Mauclair, A. Mermillod-Blondin, N. Huot, E. Audouard, R. Stoian, *Ultrafast laser writing of homogeneous longitudinal waveguides in glasses using dynamic wavefront correction*, Optics Express **16**(8), 5481–5492 (2008).
- [Men08] C. R. Mendonça, L. R. Cerami, T. Shih, R. W. Tilghman, T. Baldacchini, E. Mazur, *Femtosecond laser waveguide micromachining of PMMA films with azoaromatic chromophores*, Optics Express **16**(1), 200–206 (2008).
- [Miw01] M. Miwa, S. Juodkazis, T. Kawakami, S. Matsuo, H. Misawa, *Femtosecond two-photon stereo-lithography*, Applied Physics A **73**(5), 561–566 (2001).
- [Miy14] I. Miyamoto, K. Cvecek, Y. Okamoto, M. Schmidt, *Internal modification of glass by ultrashort laser pulse and its application to microwelding*, Applied Physics A **114**(1), 187–208 (2014).
- [Mor99] U. Morgner, F. X. Kärtner, S. H. Cho, Y. Chen, H. A. Haus, J. G. Fujimoto, E. P. Ippen, V. Scheuer, G. Angelow, T. Tschudi, *Sub-two-cycle pulses from a Kerr-lens mode-locked Ti:sapphire laser*, Optics Letters **24**(6), 411–413 (1999).

- [Mus11] J. D. Musgraves, K. Richardson, H. Jain, *Laser-induced structural modification, its mechanisms, and applications in glassy optical materials*, *Optical Materials Express* **1**(5), 921–935 (2011).
- [MV09] R. Martínez Vázquez, R. Osellame, D. Nolli, C. Dongre, H. van den Vlekkert, R. Ramponi, M. Pollnau, G. Cerullo, *Integration of femtosecond laser written optical waveguides in a lab-on-chip*, *Lab on a Chip* **9**(1), 91–96 (2009).
- [Nol03] S. Nolte, M. Will, J. Burghoff, A. Tünnermann, *Femtosecond waveguide writing: a new avenue to three-dimensional integrated optics*, *Applied Physics A* **77**(1), 109–111 (2003).
- [Okh05] A. G. Okhrimchuk, A. V. Shestakov, I. Khrushchev, J. Mitchell, *Depressed cladding, buried waveguide laser formed in a YAG:Nd<sup>3+</sup> crystal by femtosecond laser writing*, *Optics Letters* **30**(17), 2248–2250 (2005).
- [Ose03] R. Osellame, S. Taccheo, M. Marangoni, R. Ramponi, P. Laporta, D. Polli, S. De Silvestri, G. Cerullo, *Femtosecond writing of active optical waveguides with astigmatically shaped beams*, *Journal of the Optical Society of America B* **20**(7), 1559–1567 (2003).
- [Ose04] R. Osellame, N. Chiodo, G. Della Valle, S. Taccheo, R. Ramponi, G. Cerullo, A. Killi, U. Morgner, M. Lederer, D. Kopf, *Optical waveguide writing with a diode-pumped femtosecond oscillator*, *Optics Letters* **29**(16), 1900–1902 (2004).
- [Ose12] R. Osellame, G. Cerullo, R. Ramponi (Hg.), *Femtosecond Laser Micromachining*, Band 123 von *Topics in Applied Physics* (Springer Berlin Heidelberg, 2012).
- [Pä16] W. M. Pätzold, C. Reinhardt, A. Demircan, U. Morgner, *Cascaded-focus laser writing of low-loss waveguides in polymers*, *Optics Letters* **41**(6), 1269–1272 (2016).
- [Pä17] W. M. Pätzold, A. Demircan, U. Morgner, *Low-loss curved waveguides in polymers written with a femtosecond laser*, *Optics Express* **25**(1), 263–270 (2017).
- [Pal10] G. Palmer, M. Schultze, M. Emons, A. L. Lindemann, M. Pospiech, D. Steingrube, M. Lederer, U. Morgner, *12 MW peak power from a two-*

- crystal Yb:KYW chirped-pulse oscillator with cavity-dumping*, *Optics Express* **18**(18), 19095–19100 (2010).
- [Pap11] D. G. Papazoglou, S. Tzortzakis, *Physical mechanisms of fused silica restructuring and densification after femtosecond laser excitation*, *Optical Materials Express* **1**(4), 625–632 (2011).
- [Ple12] R. H. Pletcher, J. C. Tannehill, D. Anderson, *Computational Fluid Mechanics and Heat Transfer, Third Edition* (CRC Press, 2012).
- [Pon08] C. W. Ponader, J. F. Schroeder, A. M. Streltsov, *Origin of the refractive-index increase in laser-written waveguides in glasses*, *Journal of Applied Physics* **103**(6), 063516 (2008).
- [Pos09] M. Pospiech, M. Emons, A. Steinmann, G. Palmer, R. Osellame, N. Bellini, G. Cerullo, U. Morgner, *Double waveguide couplers produced by simultaneous femtosecond writing*, *Optics Express* **17**(5), 3555–3563 (2009).
- [Pos10] M. Pospiech, M. Emons, B. Väckenstedt, G. Palmer, U. Morgner, *Single-sweep laser writing of 3D-waveguide devices*, *Optics Express* **18**(7), 6994–7001 (2010).
- [Ró09] A. Ródenas, G. A. Torchia, G. Lifante, E. Cantelar, J. Lamela, F. Jaque, L. Roso, D. Jaque, *Refractive index change mechanisms in femtosecond laser written ceramic Nd:YAG waveguides: micro-spectroscopy experiments and beam propagation calculations*, *Applied Physics B* **95**(1), 85–96 (2009).
- [Ric13] S. Richter, S. Döring, F. Burmeister, F. Zimmermann, A. Tünnermann, S. Nolte, *Formation of periodic disruptions induced by heat accumulation of femtosecond laser pulses*, *Optics Express* **21**(13), 15452–15463 (2013).
- [Sak07] M. Sakakura, M. Terazima, Y. Shimotsuma, K. Miura, K. Hirao, *Observation of pressure wave generated by focusing a femtosecond laser pulse inside a glass*, *Optics Express* **15**(9), 5674–5686 (2007).
- [Sal07] B. E. A. Saleh, M. C. Teich, *Fundamentals of Photonics, Second Edition*, *Pure and Applied Optics* (Wiley, 2007).

- [Sal12] P. S. Salter, A. Jesacher, J. B. Spring, B. J. Metcalf, N. Thomas-Peter, R. D. Simmonds, N. K. Langford, I. A. Walmsley, M. J. Booth, *Adaptive slit beam shaping for direct laser written waveguides*, *Optics Letters* **37**(4), 470–472 (2012).
- [Sal14] G. Salamu, F. Jipa, M. Zamfirescu, N. Pavel, *Cladding waveguides realized in Nd:YAG ceramic by direct femtosecond-laser writing with a helical movement technique*, *Optical Materials Express* **4**(4), 790–797 (2014).
- [Sch01] C. B. Schaffer, A. Brodeur, E. Mazur, *Laser-induced breakdown and damage in bulk transparent materials induced by tightly focused femtosecond laser pulses*, *Measurement Science and Technology* **12**(11), 1784–1794 (2001).
- [Sch04] H. Schenk, R. Peschar, *Understanding the structure of chocolate*, *Radiation Physics and Chemistry* **71**(3–4), 829–835 (2004).
- [Scu03] P. J. Scully, D. Jones, D. A. Jaroszynski, *Femtosecond laser irradiation of polymethylmethacrylate for refractive index gratings*, *Journal of Optics A: Pure and Applied Optics* **5**(4), S92–S96 (2003).
- [Sha05] L. Shah, A. Y. Arai, S. Eaton, P. R. Herman, *Waveguide writing in fused silica with a femtosecond fiber laser at 522 nm and 1 MHz repetition rate*, *Optics Express* **13**(6), 1999–2006 (2005).
- [Sie10] J. Siebenmorgen, T. Calmano, K. Petermann, G. Huber, *Highly efficient Yb:YAG channel waveguide laser written with a femtosecond-laser*, *Optics Express* **18**(15), 16035–16041 (2010).
- [Sow06] S. Sowa, W. Watanabe, T. Tamaki, J. Nishii, K. Itoh, *Symmetric waveguides in poly(methyl methacrylate) fabricated by femtosecond laser pulses*, *Optics Express* **14**(1), 291–297 (2006).
- [Str02] A. M. Streltsov, N. F. Borrelli, *Study of femtosecond-laser-written waveguides in glasses*, *Journal of the Optical Society of America B* **19**(10), 2496–2504 (2002).
- [Suz06] K. Suzuki, V. Sharma, J. G. Fujimoto, E. P. Ippen, Y. Nasu, *Characterization of symmetric  $[3 \times 3]$  directional couplers fabricated by direct writing with a femtosecond laser oscillator*, *Optics express* **14**(6), 2335–2343 (2006).



- [Tho08] R. R. Thomson, A. S. Bockelt, E. Ramsay, S. Beecher, A. H. Greenaway, A. K. Kar, D. T. Reid, *Shaping ultrafast laser inscribed optical waveguides using a deformable mirror*, *Optics Express* **16**(17), 12786–12793 (2008).
- [Tho13a] J. Thomas, R. Bernard, K. Alti, A. K. Dharmadhikari, J. A. Dharmadhikari, A. Bhatnagar, C. Santhosh, D. Mathur, *Pattern formation in transparent media using ultrashort laser pulses*, *Optics Communications* **304**, 29–38 (2013).
- [Tho13b] R. Thomson, C. Leburn, D. Reid (Hg.), *Ultrafast Nonlinear Optics* (Springer International Publishing, Heidelberg, 2013).
- [Thy14] L. Thylén, L. Wosinski, *Integrated photonics in the 21st century*, *Photonics Research* **2**(2), 75–81 (2014).
- [Upp08] N. Uppal, P. S. Shiakolas, M. Rizwan, *Three dimensional waveguide fabrication in PMMA using femtosecond laser micromachining system*, in *Proceedings of SPIE*, Band 6882, 68820I (2008).
- [Was10] A. L. Washburn, R. C. Bailey, *Photonics-on-a-chip: recent advances in integrated waveguides as enabling detection elements for real-world, lab-on-a-chip biosensing applications*, *Analyst* **136**(2), 227–236 (2010).
- [Wat06] W. Watanabe, S. Sowa, T. Tamaki, K. Itoh, J. Nishii, *Three-dimensional waveguides fabricated in poly(methyl methacrylate) by a femtosecond laser*, *Japanese Journal of Applied Physics* **45**(29), L765–L767 (2006).
- [Wat09] W. Watanabe, *Femtosecond filamentary modifications in bulk polymer materials*, *Laser Physics* **19**(2), 342–345 (2009).
- [Wil02] M. Will, S. Nolte, B. N. Chichkov, A. Tünnermann, *Optical properties of waveguides fabricated in fused silica by femtosecond laser pulses*, *Applied Optics* **41**(21), 4360–4364 (2002).
- [Yan08a] W. Yang, P. G. Kazansky, Y. Shimotsuma, M. Sakakura, K. Miura, K. Hiro, *Ultrashort-pulse laser calligraphy*, *Applied Physics Letters* **93**(17), 171109 (2008).
- [Yan08b] W. Yang, P. G. Kazansky, Y. P. Svirko, *Non-reciprocal ultrafast laser writing*, *Nature Photonics* **2**(2), 99–104 (2008).

- [Zha11] C. Zhang, N. Dong, J. Yang, F. Chen, J. R. Vázquez de Aldana, Q. Lu, *Channel waveguide lasers in Nd:GGG crystals fabricated by femtosecond laser inscription*, *Optics Letters* **19**(13), 12503–12508 (2011).
- [Zhe15a] C. Zheng, A. Hu, K. D. Kihm, Q. Ma, R. Li, T. Chen, W. W. Duley, *Femtosecond laser fabrication of cavity microball lens (CMBL) inside a PMMA substrate for super-wide angle imaging*, *Small* **11**(25), 3007–3016 (2015).
- [Zhe15b] C. Zheng, A. Hu, R. Li, D. Bridges, T. Chen, *Fabrication of embedded microball lens in PMMA with high repetition rate femtosecond fiber laser*, *Optics Express* **23**(13), 17584–17598 (2015).
- [Zou04] A. Zoubir, C. Lopez, M. Richardson, K. Richardson, *Femtosecond laser fabrication of tubular waveguides in poly(methyl methacrylate)*, *Optics Letters* **29**(16), 1840–1842 (2004).
- [Zou05] A. Zoubir, M. Richardson, L. Canioni, A. Brocas, L. Sarger, *Optical properties of infrared femtosecond laser-modified fused silica and application to waveguide fabrication*, *Journal of the Optical Society of America B* **22**(10), 2138–2143 (2005).

# List of Figures

1.1	Cross-sectional schematics of: (a) step-index waveguide, (b) graded-index waveguide, (c) photonic-crystal waveguide with solid core surrounded by air-filled holes, and (d) photonic band gap waveguide with a hollow core. . . . .	6
1.2	Optical waveguide with core index $n_1$ exceeding the cladding index $n_2$ . The maximum acceptance angle $\theta_{\max}$ is determined by the critical angle $\theta_c$ and the refractive index $n_0$ of the external medium. The acceptance cone is given by $2\theta_{\max}$ . . . . .	7
1.3	(a) Bessel functions of first kind $J_l(x)$ for $l = 0, 1, 2$ . (b) Radial distribution $\Psi_0(r)$ of the LP <sub>01</sub> mode in a waveguide with core radius $a$ , calculated according to Equation (1.11). . . . .	9
1.4	Linearly polarized modes for $l = 0, 1, 2, 3$ and $m = 1, 2, 3$ . . . . .	10
1.5	Origin of energy loss in a bent waveguide. (a) Ray optics: The condition for total internal reflection is not satisfied anymore when a beam hits a concave surface. (b) Wave optics: The phase-front is trailing behind in the cladding due to an increased path length and a finite speed of light. Dissipation of energy is caused by an emerging radial component of the Poynting vector $\vec{S}$ . . . . .	11
1.6	Bend losses at 638 nm for a waveguide with a core radius of $3\ \mu\text{m}$ and index contrasts of $\Delta n = 0.0015, 0.003$ , and $0.005$ compared to a cladding with $n = 1.5$ . The curves were calculated based on Equation (1.15). . . . .	12
1.7	Schematic of evanescent coupling between waveguides. The power $P_0$ is coupled from waveguide 1 into waveguide 2 due to overlapping waveguide modes. The output powers $P_1$ and $P_2$ depend on the distance $d$ and the coupling length $L$ . . . . .	13
1.8	(a) Output powers $P_1(z)$ and $P_2(z)$ of coupled identical waveguides according to Equation (1.19). (b) A directional x-coupler, with 50:50 split ratio. . . . .	14

1.9	(a) Tunnel ionization: A strong electric field distorts the band structure and an electron can tunnel through the reduced band gap. (b) Multiphoton ionization: A number of photons is simultaneously absorbed to overcome the band gap. The green dashed lines indicate a broadened conduction band due to the uncertainty principle. . . . .	15
1.10	Schematics of avalanche ionization: A promoted electron continues to absorb photons linearly and can impact ionize a bound electron from the valence band when it has sufficient kinetic energy. . . . .	16
1.11	Typical time scales of relevant physical phenomena occurring during and after the interaction of a femtosecond laser pulse with a transparent material. Schematic based on [Gat08]. . . . .	17
1.12	SEM image of a microball cavity in PMMA created by high power femtosecond laser pulses. Visible is also a zone affected by melting and resolidification around the cavity with an increased refractive index. Figure taken from [Zhe15a]. . . . .	20
1.13	(a) Athermal regime: A low repetition rate results in single pulse modification. (b) Thermal regime: A high repetition rate enables heat accumulation. . . . .	22
1.14	Schematic depiction of focusing from air into a medium with higher refractive index. Results are a higher effective focusing depth and additional spherical aberration. (b) Simulated intensity distribution of 800 nm light focused 1 mm below the surface of glass for NA = 0.1, 0.2 and 0.6, taken from [DB07]. . . . .	24
1.15	Microscope image of the cross section of modification tracks written in Nd:YAG. At larger peak powers the vertical dimension of the structures increases due to self-focusing and filamentation. Figure taken from [Che14]. . . . .	25
1.16	(a) Longitudinal writing: The sample gets scanned parallel to laser incidence. (b) Transverse writing: The sample is scanned perpendicularly to the laser incidence. . . . .	26
1.17	(a) Beam evolution of a focused symmetric Gaussian beam and energy distribution in the y-z-plane and (b) corresponding material modification. (c) Beam evolution of a focused elliptical beam and (d) resulting symmetric waveguide. Figures taken from [Ams05]. . . . .	28
1.18	Pattern formation and writing anisotropy in PMMA. The arrows in (a) and (b) indicated the writing direction respectively, taken from [Tho13a]. . . . .	29

- 1.19 Schematic depiction of various waveguide geometries. The dashed lines indicate the waveguide core. (a) Single-track waveguide: A positive refractive index modification emerges directly in the focal volume and the track itself forms the waveguide core. (b) Dual-track waveguide: Zones of increased refractive index in the vicinity of two damage tracks are overlapped. The waveguide core is located between the tracks. (c) Depressed cladding waveguide: A number of modification tracks which exhibit a decrease in refractive index are symmetrically aligned around the waveguide core. . . . . 30
- 1.20 Some exemplary waveguide geometry variations. All scale bars correspond to 10  $\mu\text{m}$ . (a) Rhombic depressed cladding structure in Pr:LiYF<sub>4</sub> [Mü12], (b) Depressed cladding waveguide in glass built up from concentric rings [Gro15], (c) hexagonal lattice multi-core waveguide in chalcogenide glass [Mas16], (d) cladding waveguide written with a helical sample movement in Nd:YAG [Sal14], (e) White light guiding in a microstructured waveguide in ZBLAN glass using negative index contrast modifications [Gro15], (f) Antiresonant reflecting optical waveguide in boro-aluminosilicate glass based on positive index modifications [Gro13]. . . . . 32
- 1.21 (a) Difference interference contrast microscope image of a tubular waveguide cross section and corresponding intensity distribution of guided light at 632.8 nm [Zou04]. (b) Microscope image of a waveguide in PMMA written in longitudinal configuration and the corresponding refractive index profile [Bau07]. (c) Microscope images of waveguides fabricated at 100 kHz (top) and 500 kHz (bottom) and the corresponding guided modes at 633 nm [Eat12]. . . . . 33
- 2.1 Schematic diagram of the writing setup. An electro-optic modulator (EOM) picks pulses from the femtosecond laser source to tune the repetition rate. A half-wave plate and polarization beam splitter (PBS) are utilized to control the pulse energy. A mechanical beam shutter clears or blocks the beam path. It gets triggered by the 3D translation stages. The beam diameter is adjusted by a telescope and then focused into the substrate by an aspheric lens or microscope objective. 37
- 2.2 (a) Exemplary intra-cavity pulse evolution with cavity dumping. (b) Measured spectrum and (c) autocorrelation function of the corresponding pulse. . . . . 38

- 2.3 Structural formulas: (a) Methyl methacrylate monomer, (b) Poly(methyl methacrylate) chain. . . . . 41
- 2.4 An alignment laser is coupled into the writing setup via a dichroite and superimposed with the writing beam. A 50:50 beam splitter (BS) sends part of the back reflection from the surface of the substrate onto a CCD camera. Using a mirror mount the sample is aligned perpendicular to the beam via triangulation. . . . . 42
- 2.5 Schematic diagram of the waveguide characterization setup. Light is coupled from a fiber into a waveguide. At the exiting facet, the transmitted light gets collected by an objective and imaged onto a CCD camera. An iris diaphragm shields from scattered light. . . . . 44
- 2.6 (a) Photograph of the analysis setup. Visible are the translation stages which hold all components and a part of the stereo microscope which is used for observation. (b) Exemplary microscope image showing a fiber coupling light into a waveguide. Visible scattering losses highlight the coupled waveguide. . . . . 44
- 2.7 Left: False color representation of an intensity distribution of a Thorlabs SM600 fiber at 638 nm. Right: Horizontal and vertical cut of the same profile. Red line shows the fit of a Gaussian distribution. The mode field radius is calculated to be  $1.85\ \mu\text{m}$  on both axis. . . . . 45
- 2.8 (a) Schematic of the NA measurement method. Interference between guided and unguided light allows for the calculation of the acceptance angle of a waveguide. (b) Typical CCD image of the interference fringes. 46
- 3.1 (a) Top view of single-pulse modifications, separated by a distance of  $20\ \mu\text{m}$ , for pulse energies of 300, 500 and 700 nJ. The laser incidence was into the plane. The white dotted circles mark the outside margins of the visible structural changes. (b) Corresponding cross-sectional morphology of a single-pulse modification. Laser incidence was from the top. The white dashed line marks the waist evolution of the focused Gaussian beam. The scaling is identical for all images. . . . . 52
- 3.2 Light microscopy image of zones exposed to stationary irradiation of laser pulses with an energy of 200 nJ. The number of pulses per spot was  $2 \cdot 10^3$ ,  $2 \cdot 10^4$  and  $2 \cdot 10^5$  at repetition rates of 1, 10, 50 and 100 kHz. The laser incidence was into the plane. . . . . 55

- 3.3 Evolution of the material temperature 3  $\mu\text{m}$  from the center of the focus over the course of 12 consecutive pulses. (a) 200 nJ pulse energy at 1 kHz, 10 kHz, 50 kHz and 100 kHz. (b) 500 nJ pulse energy at 1 kHz and 10 kHz. The dashed red line marks the glass transition temperature of PMMA at  $T_g = 372$  K whereas the black dashed line marks the temperature for random chain scission at  $T_{cs} = 623$  K. The data for 1 kHz set has a small offset on the horizontal axis to increase its visibility. . . . . 57
- 3.4 Top row: Top view of modification tracks with spacings from 10  $\mu\text{m}$  to 0.5  $\mu\text{m}$  between consecutive pulses, written at 200 nJ. Laser incidence was into the plane. Bottom row: corresponding cross-sectional morphology of the material modification. . . . . 59
- 3.5 SEM images of embedded femtosecond laser written structures. (a) Surface bulge due to pressure from the core of the modification track, emphasized by a 2  $\mu\text{m}$  thick Platinum bar. (b) Cross-sectional cut through the structure, exposing a cavity at the core. . . . . 60
- 3.6 Left: Microscope image of a waveguide written at the low-energy thermal regime. Right: False color representation of a annular intensity distribution of the corresponding guided mode. . . . . 62
- 3.7 Schematic representation of the refractive index change mechanism during waveguide writing. (a) An expanding plasma core at the center of the focus spot applies radial pressure on the surrounding material. (b) After processing, three zones can be distinguished on the final structure: (I) A cavity at the center which matches in dimension the spot size of the focused laser beam. (II) An inner ring of material modification affected by melting and resolidifying. (III) An outer ring of increased refractive index due to material densification. . . . . 63
- 3.8 Microscope images of the cross-sectional evolution of the modification track at 500 nJ. Focusing was done with different aspheric lenses with a numerical aperture of 0.40, 0.55 and 0.65. Laser irradiation was from top. . . . . 64

- 3.9 Intensity distributions of waveguides written with an aspheric lens with an NA of 0.65. (a) 300 nJ and 40 mm/s. Guiding takes place above the primary modification. (b) 300 nJ and 50 mm/s. Guiding takes place between the primary and the secondary modification. (c) 400 nJ and 50 mm/s. Guiding takes place below the secondary modification. The white dotted circles mark the outside margins of the visible primary and secondary modifications. . . . . 66
- 3.10 (a) Bright-field microscope image of a polished end facet of a cascaded-focus material modification fabricated at 100 kHz repetition rate. Pulse energy was 550 nJ and the writing speed 35 mm/s. (b) Intensity distribution of the corresponding guided mode at a 660 nm test-wavelength. The white dotted line marks the outside margins of the primary and secondary modification. . . . . 67
- 3.11 Success probability of the fabrication process as a function of the writing speed and the pulse energy. (a) A success probability of almost 100 % is achieved in the dark red area. (b) Too slow writing speeds has the success probability quickly drop below 50%. . . . . 68
- 3.12 Microscope images of modification tracks fabricated with different writing parameters. Writing direction was from left to right in every image. (a) Homogeneous material modification optimal for waveguiding. (b) Frayed edges caused by too slow writing speeds. (c) Non-periodic disruptions caused by too large pulse energies. (d) Periodic disruptions triggered by disturbances on the laser beam. . . . . 68
- 3.13 Refractive index contrast  $\Delta n$  as a function of the energy dosage  $D$ . The red line marks the average  $\Delta n$ , with the highlighted background being the standard deviation. . . . . 69
- 3.14 Insertion losses as function of the waveguide length for guided light at 600 nm and 850 nm. The propagation losses (PL) are determined from a linear fit. The errorbars are the standard error of the sampling distribution. . . . . 71
- 3.15 Setup to measure diffraction efficiencies of femtosecond laser written gratings. . . . . 72



- 3.16 (a) Microscope image of the cross section of a single-pulse modification. The track was written with a 0.55-NA aspheric lens 150  $\mu\text{m}$  below the surface at a repetition rate of 10 kHz, 250 nJ pulse energy and a writing speed of 40  $\text{mm/s}$ . (b) False color representation of the intensity distribution of the corresponding guided modes at 638 nm. The plot is composed of two images since only one waveguide can be coupled at a time. (c) Schematic depiction of the material modification and stress distributions surrounding it. . . . . 74
- 3.17 Schematic of a dual track waveguide. It is built up by overlapping two adjacent refractive index modification zones by placing two single-pulse tracks close to each another at a distance  $s$ . . . . . 75
- 3.18 Dual-track waveguides with spacings of 10  $\mu\text{m}$ , 12  $\mu\text{m}$ , 14  $\mu\text{m}$ , 16  $\mu\text{m}$  and 20  $\mu\text{m}$ . Top row: bright field microscopy images of the waveguide cross section. Bottom row: Intensity distribution of the guided mode at 638 nm. . . . . 75
- 3.19 (a) Dark-field microscopy image of an ensemble of cascaded-focus modification tracks at a constant spacing of  $\Delta y = 16 \mu\text{m}$ . (b) Exemplary intensity distribution of a mode that can be guided between every two neighboring tracks. The white dotted circles mark the outside margins of the primary and secondary modification. . . . . 77
- 3.20 Cascaded-focus multi-track waveguide scheme. (a) Two blocks of four modifications with a spacing  $\Delta y$  in between are written into the material. In between the blocks, a lateral spacing  $s$  forms the core of the waveguide. (b) Cross-sectional dark field microscopy image of the end-facet of a multi-track waveguide. . . . . 77
- 3.21 Intensity distributions of guided modes in false color representation for varying core sizes  $s$ . The white dots represent three additional modifications on each side with a respective distance of 10  $\mu\text{m}$ . . . . . 79
- 3.22 Insertion losses as a function of waveguide length for test-wavelengths (a)  $\lambda = 638 \text{ nm}$  and (b)  $\lambda = 850 \text{ nm}$ . Spacing for the waveguide core was  $s = 16, 18, 20$  and  $22 \mu\text{m}$ . Propagation losses are determined from a linear fit. . . . . 80
- 3.23 Schematic of a multi-track waveguide with an s-curve segment. Each track has to follow an individual path with varying radii of curvature. The reference radius  $R$  refers to the center of the waveguide. . . . . 81

3.24	Bend losses per unit length of s-curved waveguides with $s = 18 \mu\text{m}$ in dependency of the bend radius $R$ measured at $\lambda = 638 \text{ nm}$ . The theoretical curve was calculated with $a = 3 \mu\text{m}$ , $\Delta n = 1.5 \cdot 10^{-3}$ and $n_{\text{eff}} = 1.49062$ . . . . .	82
3.25	(a) Microscope image of the cross-section of a periodic cladding structure surrounding a waveguide core. (b) Intensity distribution of the corresponding mode guided at the core of the structure. . . . .	83
3.26	Left: Photograph of a thin-film filter sitting in a groove cut through a set of multi-track waveguides. Right: The black curve shows an excerpt of the intensity distribution of a measured spectrum of white light propagating through the filter via a waveguide. The red curve shows the design transmission of the filter at a tilt of $17^\circ$ . . . . .	85
3.27	(a) Spectrum of a frequency doubled pulse at $525 \text{ nm}$ central wavelength, recorded at the waveguide output for small pulse energies. (b) Spectral broadening due to self-phase modulation at increased pulse energies. . . . .	87

# Appendix A

## Heat Accumulation Simulation

The one dimensional heat-diffusion equation is given by

$$\frac{\partial}{\partial r} \left( r^2 \frac{\partial T}{\partial r} \right) = \frac{r^2}{\alpha} \frac{\partial T}{\partial t}, \quad (\text{A.1})$$

with  $T(r, t)$ , the temperature of the material as a function of space  $r$  and time  $t$ , and  $\alpha$  the thermal diffusivity of a given material.

The temperature is discretized in the form of  $T_j^n$ , with  $n$  and  $j$  being the linear coordinates in time and space, respectively. The discretized form of the differential equation in the ‘‘Foward in time centered in space’’ (FTCS) scheme becomes

$$T_j^{n+1} = T_j^n + \alpha \Delta t \left( \frac{T_{j+1}^n - T_{j-1}^n}{r_j \Delta r} + \frac{T_{j+1}^n - 2T_j^n + T_{j-1}^n}{\Delta r^2} \right). \quad (\text{A.2})$$

The size of a time step is  $\Delta t$  and the size of a step in space is  $\Delta r$ . The position in space in SI units is  $r_j$ . The stability criteria for the FTCS scheme is

$$\alpha \frac{\Delta t}{\Delta r^2} < \frac{1}{2}. \quad (\text{A.3})$$

For symmetry reasons only one branch of the heat distribution is simulated. The peak is located at  $j_0$  and the array is defined large enough, so that at  $j_{\max}$  always remains at ambient temperature  $T_0$ . These assumptions result in the following side conditions:

$$T_{j_0}^{n+1} = T_{j_0}^n + 2\alpha \Delta t \left( \frac{T_{j_0+1}^n - T_{j_0}^n}{\Delta r^2} \right), \quad (\text{A.4})$$

$$T_{j_{\max}}^{n+1} = T_0. \quad (\text{A.5})$$



# Publications

## Journal Publications

1. Welm M. Pätzold, Carsten Reinhardt, Ayhan Demircan, and Uwe Morgner  
*Cascaded-focus laser writing of low-loss waveguides in polymers*,  
Optics Letters **41**(6), 1269–1272 (2016).
2. Welm M. Pätzold, Ayhan Demircan, and Uwe Morgner  
*Low-loss curved waveguides in polymers written with a femtosecond laser*,  
Optics Express **25**(1), 263–270 (2017).
3. Christian Kelb, Welm M. Pätzold, Uwe Morgner, Maik Rahlves, Eduard Reithmeier, and Bernhard Roth  
*Characterization of femtosecond laser written gratings in PMMA using a phase-retrieval approach*,  
Optical Materials Express **6**(10), 3202–3209 (2016).

## Contributions to International Conferences

1. Welm M. Pätzold, Carsten Reinhardt, Boris Chichkov, and Uwe Morgner  
Poster Presentation: *On the stability of direct femtosecond laser written waveguides in poly(methyl methacrylate)*,  
CLEO Europe, June 2015, Munich, Germany
2. Welm M. Pätzold, Carsten Reinhardt, Ayhan Demircan, and Uwe Morgner  
Poster Presentation: *Low-loss embedded waveguides in PMMA written by a femtosecond laser*,  
CLEO: Science and Innovations 2016, June 2016, San José, USA  
DOI: 10.1364/CLEO\_AT.2016.JTh2A.33

## Contributions to National Conferences

1. Welm M. Pätzold, Bernhard Kreipe, Moritz Emons, Carsten Reinhardt, Boris Chichkov, and Uwe Morgner  
Poster Presentation: *Direct writing of waveguides in polymers with a fs laser*,  
DPG Spring Meeting, March 2014, Berlin, Germany
2. Welm M. Pätzold, Carsten Reinhardt, Bernhard Kreipe, Boris Chichkov, and Uwe Morgner  
Oral Presentation: *Femtosecond laser writing of Type I and Type II waveguides in polymers*,  
DPG Spring Meeting, March 2015, Heidelberg, Germany
3. Welm M. Pätzold, Carsten Reinhardt, Ayhan Demircan, and Uwe Morgner  
Oral Presentation: *Low-loss femtosecond laser written waveguides in PMMA*,  
DPG Spring Meeting, March 2016, Hannover, Germany
4. Welm M. Pätzold, Carsten Reinhardt, Ayhan Demircan, and Uwe Morgner  
Oral Presentation: *Femtosecond laser written low-loss single-mode waveguides in PMMA*,  
Annual Meeting of DGaO, May 2016, Hannover, Germany

# Curriculum Vitae

## Personal Details

Welm Maximilian Pätzold

born 29<sup>th</sup> of November 1985 in Braunschweig, Germany

unmarried, German

## Ph.D. Studies

since 11/2012      Ph.D. student at the Institute of Quantum Optics at the  
Leibniz Universität Hannover, research group of Prof. Dr.  
Uwe Morgner

## University Education

04/2010 – 07/2012      Master of Science in Physics, Georg-August-Universität  
Göttingen  
08/2009 – 03/2010      Research assistant at Montana State University, Bozeman,  
USA  
10/2006 – 07/2009      Bachelor of Science in Physics, Georg-August-Universität  
Göttingen

## Alternative Civilian Service

07/2005 – 03/2006      Caritas Home for mentally handicapped adults,  
Hann. Münden

## School Education

1992 – 2005      Abitur, Grotefeld-Gymnasium Münden, Hann. Münden





# Danksagung

An dieser Stelle möchte ich von Herzen all jenen danken, die mich in den letzten viereinhalb Jahren begleitet und somit direkt oder indirekt zum Gelingen dieser Arbeit beigetragen haben.

An erster Stelle möchte ich meinem Doktorvater Uwe Morgner danken für die Möglichkeit, auf so einem spannenden und vielfältigen Themengebiet zu forschen.

Bei Carsten Reinhardt und Ulrike Willer bedanke ich mich für die Übernahme des Korreferats. Clemens Walther danke ich für den Vorsitz bei der Disputation.

Vielen Dank auch dem gesamten Team des Sonderforschungsbereichs PlanOS. In so einem interdisziplinären Umfeld zu arbeiten und zu forschen, war eine ganz besondere Erfahrung und weit mehr als nur ein Blick über den Tellerrand. Besonders erwähnt seien die Kollegen Carsten, Tobias und Urs, die mit mir zusammen auf vielen Veranstaltungen das Teilprojekt B03 vertreten haben.

Ich hatte das große Glück noch Gründungsmitglieder, „die mit Uwe das Labor aus dem Nichts erschaffen haben“, kennenlernen zu dürfen, die mich sofort herzlich in die Arbeitsgruppe aufgenommen haben. Mein Dank gilt somit allen ehemaligen und aktuellen Mitgliedern der AG Morgner für das angenehme Arbeitsumfeld. In diesem Zusammenhang auch noch mal ein besonderer Dank an alle Korrekturleser. Ebenfalls möchte ich mich auch ganz herzlich bei der gesamten Werkstatt und dem gesamten Sekretariat bedanken für den unkomplizierten und reibungslosen Ablauf des Institutsalltags. Besondere Erwähnung soll Frau Hünitzsch finden, die auch in kniffligen Situationen immer weiß, was zu tun ist.

Zum Schluss noch ein herzliches Dankeschön an meine Familie und enge Freunde aus nah und fern.

**Vielen Dank euch allen!**

